Space Legos: A Concept for In-Space Assembly of Large Structures with a Stationary Robot

Thesis by
Sahangi Dassanayake

In Partial Fulfillment of the Requirements for the
Degree of
Doctor of Philosophy in Space Engineering

CALIFORNIA INSTITUTE OF TECHNOLOGY
Pasadena, California

2025
Defended September 30, 2024

Sahangi Dassanayake
ORCID: 0000-0002-1363-5764

ACKNOWLEDGEMENTS

This thesis would not have been possible without the support, encouragement, and guidance of many individuals who have shaped my journey, both academically and personally.

First and foremost, I would like to express my deepest gratitude to my advisor, Professor Sergio Pellegrino. Your insightful guidance, passion for the field, and unwavering support have been pivotal throughout my Ph.D. journey. Thank you for encouraging me to explore my ideas independently, for keeping me focused when it was most needed, and for the many exciting discussions and opportunities you have generously provided.

I would like to express my heartfelt thanks to my collaborators in the DARPA NOM4D project at the Space Structures Lab. Jaden, Alan, and Charles—your mentorship, wisdom, and shared enthusiasm for innovation have enriched my research experience. You encouraged my ideas, fostered collaboration, and without your dedication, this thesis would not have taken the same form. I also wish to extend my sincere thanks to Mark Thomson, as well as Professor Igor Bargatin and his team at the University of Pennsylvania, for their invaluable guidance and contributions throughout this work. A special thank you to Dr. Andrew Detor for his leadership of the DARPA NOM4D program and for supporting this research through grant HR001122C0054.

I am sincerely thankful to my candidacy and thesis committee members, Professors Domniki Asimaki, Guruswami Ravichandran, Ares Rosakis, and especially, Daniel Meiron. Your feedback, encouragement, and support have been vital in helping me navigate this academic journey.

To my dear labmates, thank you for being there to exchange ideas and share the highs and lows of graduate school (and endure the many practice talks!). I'm incredibly fortunate to have had such a supportive and fun group by my side. Every conference, lab party, and group meeting was brighter and filled with unforgettable memories, thanks to you.

To my GALCIT/MCE G1 cohort—Sorina, Niyati, Tracy, Stephanie, John, Brayden, Paul, Tanner, Miles, Peter, Ying, Nikhil—our shared experiences have been a cornerstone of my time here. You made the tough times (G1 and Quals during

COVID!!) easier and the good times even better, and I'm grateful for every moment of fun, laughter, and friendship we have had along the way.

A special thanks to the entire GALCIT community and the dedicated administrative staff for your tireless efforts in keeping everything running so smoothly behind the scenes. I deeply appreciate all that you do.

To my wonderful friends in the performing arts—especially Nancy, your creativity and passion for your craft have always been a source of inspiration. You welcomed me with open arms and reminded me that art and science are intertwined in their pursuit of truth and beauty, and I am lucky to have shared this journey, and the stage, with you.

To my Caltech friends—Shruti, André, Scott, Yanky, Hirsh, Taylan, Utku, and Mert, since the very beginning of grad school, you have been there for me, celebrating my successes and offering encouragement through the setbacks. Your warmth, kindness, and unfaltering support have brought me so much comfort and joy. I moved to LA knowing no one, and I am incredibly grateful to you for making this city feel like home. I'm so fortunate to have found such an incredible community here.

To my friends who have supported me from across continents—Roanga and Nipun, your constant presence, despite the distance and time zone differences, has meant more to me than I can express. You listened to my endless rants, offered thoughtful advice, and shared in both my frustrations and triumphs. Your unwavering encouragement and friendship have been a grounding force throughout this journey, and I'm incredibly grateful to have had you by my side, even from afar.

Finally, to my family—Amma, Appachchi, Nangi—I don't have enough words to express my gratitude. Amma and Appachchi, you instilled in me curiosity, confidence, and an eagerness to learn that has guided me throughout my life. You gave me the freedom to make mistakes, while always assuring me of your pride in my aspirations and your unconditional love and support—even going so far as to arrange for home-cooked meals to be sent when I was too busy to eat. Nangi, thank you for being there to listen when I needed someone to talk to during my moments of anxiety. And to Bubbles, my dog, thank you for being a sweet and constant source of comfort. I love you all, and this thesis is as much yours as it is mine.

To everyone who has been a part of this journey, whether mentioned here or not, thank you from the bottom of my heart. Your presence in my life has made all the difference.

ABSTRACT

Human nature is inherently driven by the desire to build; advancing from primitive shelters to skyscrapers, and extending this relentless pursuit of progress to space through technological innovations. As space missions require larger and more complex structures, traditional deployable systems face challenges due to constraints on launch mass, volume, and complex deployment mechanisms. In-space assembly (ISA) offers a promising solution for constructing large structures, such as telescopes and satellites, directly in space.

This thesis introduces a novel ISA concept with a centralized 'truss builder' for autonomous assembly of polygonal-ring structures, using simple, repetitive operations and focusing on scalable mesh reflectors for communication and imaging. Utilizing the standard AstroMesh architecture, a rapid generalized design method is developed. Through the analysis of reflector geometry, optimized cable prestress, structural design, and a high-fidelity finite element model, analytical scaling laws are derived for mass, stowed envelope, and natural frequency based on aperture diameter. A semi-analytical homogenization model is introduced to efficiently predict fundamental natural frequencies. Stowed volume is a key limitation for large deployable reflectors, approaching current and future launch capacity limits, while the proposed ISA reflectors face no such constraints for apertures up to 200 meters.

A two-dimensional finite element model simulates the assembly kinematics of large ring-like structures with the proposed ISA concept, enhancing understanding of the process and evaluating key design aspects of a stationary robot assembling scalable ring-like trusses. The model provides insights for optimizing autonomous assembly systems and underscores the need for advanced numerical simulations to ensure smooth assembly and stability during ISA, especially as structures scale.

Lab-scale prototype testing validates the ISA concept, with results aligning qualitatively with simulations. Both experiments and simulations reveal a range of viable solutions, demonstrating flexibility for future mission designs. This research offers crucial insights into the design and scaling of mesh reflectors, setting the stage for comparing ISA with traditional deployable systems. The proposed ISA concept presents a practical solution for building high-precision, large-scale structures in space, advancing the field of space construction and supporting future extended space missions.

PUBLISHED CONTENT AND CONTRIBUTIONS

[1] J. Suh, S. P. Dassanayake, M. Thomson, and S. Pellegrino, "Scaling Laws for Deployable Mesh Reflector Antennas," *AIAA Journal*, pp. 1–12, 2024. DOI: 10.2514/1.J063940.
S.D. participated in conceptualizing the project, developed the generalized design method, performed the scaling analysis for mass and stowed volume and contributed to the preparation of the manuscript.

[2] J. Suh, S. P. Dassanayake, M. Thomson, and S. Pellegrino, "In-Space Assembly of Large Mesh Reflector Antennas," in *Aerospace Structures, Structural Dynamics, and Materials Conference, SSDM 2024 [Technical Presentation]*, 2024, p. 137 740.
S.D. participated in conceptualizing the project, developed the generalized design method and simulation techniques, and performed the scaling analysis for mass and stowed volume and the numerical analyses on assembly.

[3] S. P. Dassanayake, J. Suh, M. Thomson, and S. Pellegrino, "Mass, Volume and Natural Frequency Scaling of Deployable Mesh Reflectors," in *AIAA SCITECH 2024 Forum*, 2024, p. 2041. DOI: 10.2514/6.2024-2041.
S.D. participated in conceptualizing the project, developed the generalized design method, performed the scaling analysis for mass and stowed volume and prepared the manuscript.

[4] J. Suh, S. P. Dassanayake, M. Thomson, and S. Pellegrino, "Scalable Concept for Reflector Antenna Assembled in Space," in *AIAA SCITECH 2024 Forum*, 2024, p. 0823. DOI: 10.2514/6.2024-0823.
S.D. participated in conceptualizing the project and developed the generalized design method.

[5] J. Suh, S. Dassanayake, M. Thomson, and S. Pellegrino, "Concept for In-Space Assembly of Large Reflector Antennas," in *41st ESA Antenna Workshop ESTEC*, 2023.
S.D. participated in conceptualizing the project, developed the generalized design method, performed the scaling analysis and contributed to the preparation of the manuscript.

[6] J. Suh, S. P. Dassanayake, and S. Pellegrino, "In-Space Assembly of Large Mesh Reflectors," in *AIAA SCITECH 2025 Forum [Accepted]*, 2025.
S.D. developed the simulation techniques, performed the numerical analyses, and contributed to the preparation of the manuscript.

[7] S. P. Dassanayake and S. Pellegrino, "In-Space Assembly of Large Structures with a Stationary Robot," *[In Preparation]*, 2025.

S.D. developed the simulation techniques, performed the detailed numerical analyses and prepared the manuscript.

TABLE OF CONTENTS

LIST OF ILLUSTRATIONS

LIST OF TABLES

NOMENCLATURE

Space Legos. Modular components engineered for assembling structures in space.

Stationary Robot. A robot that remains fixed in position relative to the spacecraft and does not traverse across or along the structure being assembled.

Chapter 1

LARGE STRUCTURES IN SPACE

1.1 In-Space Assembly: A Strategy for Launching Large Space Structures?

The growing demand for advanced space missions is driving the need for larger and more complex space structures. Historically, construction of large space structures has relied on deployable systems housed within a single launch vehicle. This method has been successfully employed in missions involving structures typically ranging from 10 to 20 meters in size [1]–[4], as shown in Fig. 1.1. However, on-orbit deployment poses significant challenges, primarily due to intricate mechanisms required, increasing the risk of failure and impacting mission reliability [5], [6]. Substantial portions of engineering costs and launch mass are allocated to ensuring the structure's survival during launch. As component sizes increase, these costs escalate further, driven by the complex folding mechanisms and the extensive testing needed to guarantee successful deployment. Additionally, the size of these structures is limited by the mass, volume, and stress constraints imposed by launch vehicles, as exemplified by the James Webb Space Telescope (JWST) and its 6.5-meter primary mirror, which likely represents the largest aperture achievable for single-launch telescopes [7], [8].

On-orbit assembly, as demonstrated by the construction of the International Space Station (ISS) using separately launched large modules, offers a promising approach to overcoming payload constraints in space missions [9], [10]. In-space assembly

(ISA) maximizes the use of a launcher's fairing capacity, enabling the construction of very large structures. This capability is especially vital for the development of large space telescopes, a key objective in space exploration, as scientists have long sought to deploy large optical systems in space with primary mirrors exceeding 10 meters in diameter. Several concepts for such telescopes have been proposed, including a scalable 30-meter space observatory operating across ultraviolet, optical, and near-infrared wavelengths [11], and a 10-meter ultraviolet-optical telescope [12], both intended to be assembled robotically in space. In the 1990s, NASA determined that deploying a 25-meter telescope mirror through mechanical means was impractical due to inefficient packaging, concluding that an erectable mirror assembled in orbit by astronauts or robotic systems would be more feasible [13].

Stowed configuration Deployed configuration (primary mirror)

(a)

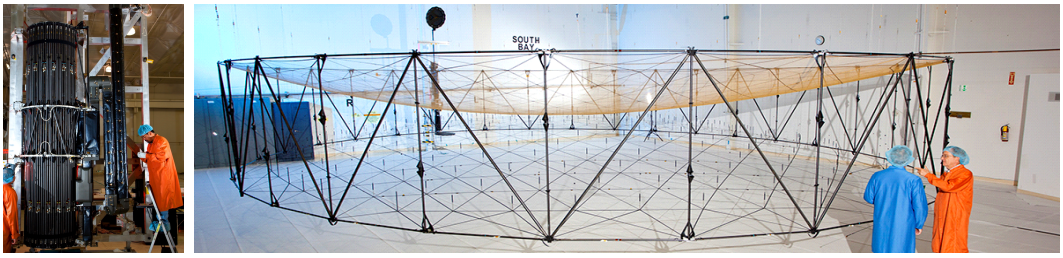

Stowed configuration Deployed configuration

(b)

Figure 1.1: State-of-the-art deployable structures: (a) JWST (NASA, 2016) and (b) AstroMesh deployable mesh reflector (Northrop Grumman, 1999)

Extensive research into support structures for space telescopes and reflectors has highlighted the benefits of using trusses, leading to significant progress in lightweight space truss design [14], [15] (see Fig. 1.2). This research includes early designs for large, high-precision segmented reflectors [16] and a doubly-curved truss structure that was designed, fabricated, and validated for its exceptional surface precision, stiffness, and strength [17]. However, assembling trusses with large areas or spans requires a substantially greater number of lightweight truss elements, necessitating careful consideration of several key design factors [18]–[20]. These factors include the modular design of structural components to enable easy integration while maintaining sufficient stiffness when assembled, the efficient packaging and delivery of components to the target orbit, and efficient ISA concepts to achieve the desired functional configuration of the structure.

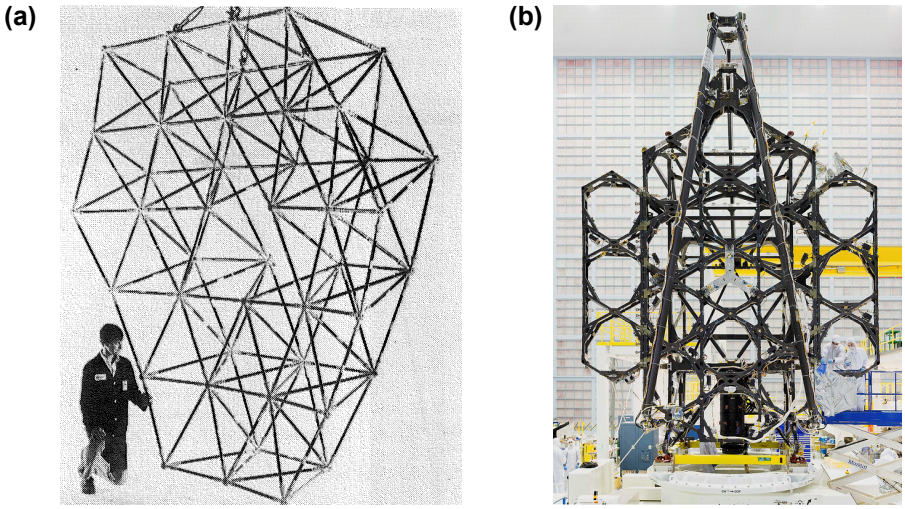

Figure 1.2: Lightweight trusses as support structures: (a) erectable 4-meter tetrahedral truss [17] and (b) JWST support structure (NASA, 2015)

1.2 Robotic Autonomous Assembly

There is a growing shift towards autonomous robotic systems in assembly, replacing traditional methods. Extra-Vehicular Activity (EVA)-based structural assembly culminated in a 14-meter diameter doubly-curved telescope truss experiment [21]–[23]. This study underscored several crucial lessons, such as the need for simple, repetitive construction tasks, the benefit of using movable work platforms, and the distribution of tasks to minimize worker fatigue. It also highlighted the importance of storing components near the crew for quick access and efficient assembly, while recognizing the limitations of manual assembly as the size of the structure

increases. Manual assembly becomes impractical for large structures, necessitating the shift to centralized, autonomous assembly methods utilizing robotic systems.

In the manufacturing industry, the use of assembly robots is a well-established practice, where robots have become integral, excelling in precise, repetitive tasks that ensure efficient, high-quality product assembly and enable rapid production. However, applying robotics to construction, particularly in difficult environments such as hazardous or remote locations, has not progressed as rapidly, with only a few feasible short-term solutions available [24]–[27].

Numerous innovative structural concepts and system architectures have been developed to facilitate the autonomous ISA of large, functional structures [28]–[30]. These advancements are paralleled by the growing adoption of collective and traversing robotic assembly methods, as shown in Fig. 1.3. Noteworthy examples include the assembly of cubic truss structures by multiple aerial robots [31], a coordinated multi-robot system for assembling furniture [32] and termite-inspired climbing robots [33]. However, the use of multiple robots for assembly of structures introduces several intricate challenges, akin to those faced in EVA experiments. These challenges include ensuring seamless coordination and communication among robots to prevent interference, optimizing task distribution to enhance productivity, and managing workspace constraints to avoid collisions and provide adequate operational space (see Fig. 1.3(a-c)). Additionally, the setup and maintenance of multi-robot systems are inherently complex, often resulting in heavier robots that must be supported by the stiffness of the structure. As the structure grows larger, scalable communication and coordination become increasingly critical, and traversals become significantly longer and more time-consuming. As the complexity of autonomously assembling large trusses grows, so does the risk of encountering single points of failure that could disrupt or halt the entire process. Therefore, simplifying system architecture and operations in the autonomous assembly of large trusses is essential.

Streamlining processes and reducing reliance on complex subsystems improve reliability and operational robustness while preserving the advantages of autonomous assembly. Jenett and Cheung [34] aimed to simplify truss assembly by developing inchworm-inspired bipedal “Relative Robots” (see Fig. 1.3(d-f)). These robots are designed to interact with their structured environment, using the modular three-dimensional lattice they are constructing as support. As they traverse the lattice, they manipulate and transport the building blocks needed for assembly. While this concept comes closest to the idea of ‘Space Legos’ by using identical robots and modular

building blocks, simplifying control mechanisms and enhancing reliability through fault-tolerant connections, it still relies on coordinating multiple robots. Strengthening the reliability of large truss assembly and advancing autonomous construction capabilities in space and other challenging environments remain key goals.

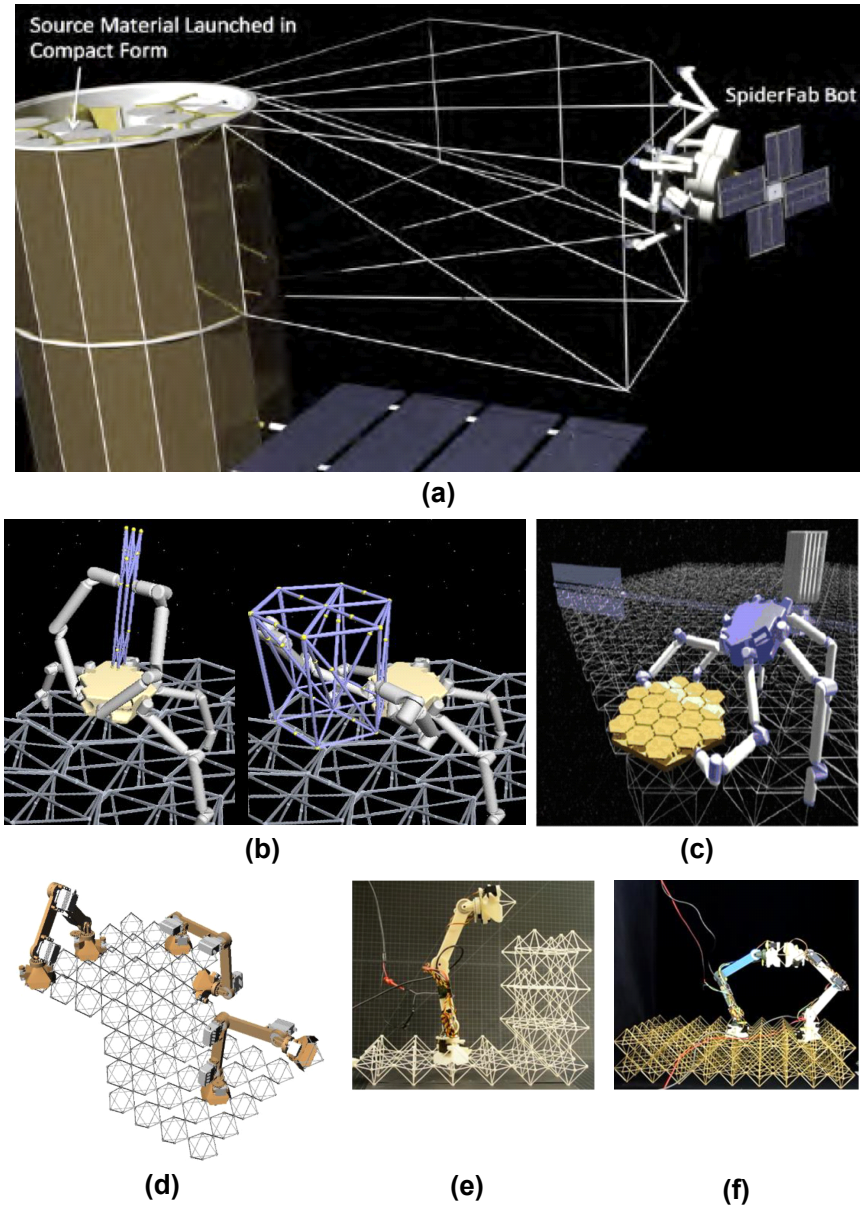

Figure 1.3: Advancements in robotic assembly: (a) SpiderFab robot constructing a support structure for functional elements [9], Robot-Assembled Modular Space Telescope (RAMST) architecture [29]: dexterous hexbot (b) deploying and assembling truss and (c) traversing and assembling mirror module and BILL-E: robotic platform [34]: identical bipedal robots (d) using the truss as support for traversing, (e) placing and (f) moving identical truss modules.

1.3 Reflector Antennas

Large reflector antennas have garnered significant interest for space missions due to their requirement for high resolution and bandwidth in communication and imaging, with commercial systems available from companies such as Astro Aerospace Northrop Grumman, L3 Harris, and Tendeg. Mesh reflectors were selected as the primary structure of interest for the research described in this thesis, guided and supported by funding from the DARPA NOM4D (pronounced "NOMAD") program [10].

Early designs for deployable reflectors, such as the umbrella-type with metallic wire mesh stretched over parabolic ribs [35], and the wrap-rib type where thin shell elastic ribs with a parabolic edge profile were wound around a central hub mechanism [36], achieved compact stowage but struggled to deliver high surface accuracy for larger apertures. To address these challenges, a concept with a faceted reflective surface [37], [38] emerged, utilizing triangular mesh facets on a prestressed cable net to form a tension truss (see Fig. 1.4(a)). This innovation led to the development of the *AstroMesh* reflector by Hedgepeth and Thomson [39], [40], which features two doubly curved cable nets tensioned across a deployable perimeter truss (see Fig. 1.4(b)). This design has proven effective in achieving superior surface accuracy, mass efficiency, and packaged volume, leading to its adoption for a variety of space missions with diameters ranging from 3 to 25 meters [41]–[43]. It has become a widely accepted standard for deployable mesh reflectors, inspiring numerous adaptations of the original design by Hedgepeth and Thomson [44], [45].

Most of the existing research on deployable mesh reflectors has primarily targeted radio frequency (RF) efficiency improvements, leaving the relationship between aperture size, focal length, and the practical aspects of mass and stowed volume underexplored. This gap is particularly evident in system-level studies, where understanding these dependencies is crucial for the design and optimization of large-scale deployable mesh reflectors. Although some studies, such as Thomson's work [41] on reflectors up to 25 meters in diameter, have addressed mass scaling, the broader implications for very large reflectors and across different scales remain insufficiently investigated. There has been a significant focus on form-finding techniques to improve the surface accuracy and stability of cable nets [46]–[49], and on the dynamic behavior of reflectors to prevent coupling with spacecraft attitude control systems [50]–[53]. While several numerical and experimental studies on the dynamic behavior of mesh reflectors have been conducted [52], [53], high-fidelity

models and experimental approaches fall short when it comes to analyzing extremely large reflectors or studying them across a broad range of scales due to the rapidly increasing number of structural elements involved. The lack of comprehensive data underscores the need for further research to accurately predict and optimize key metrics such as mass, stowed volume, and fundamental natural frequency of vibration, particularly in the design of very large reflectors and in determining the limits of current technology.

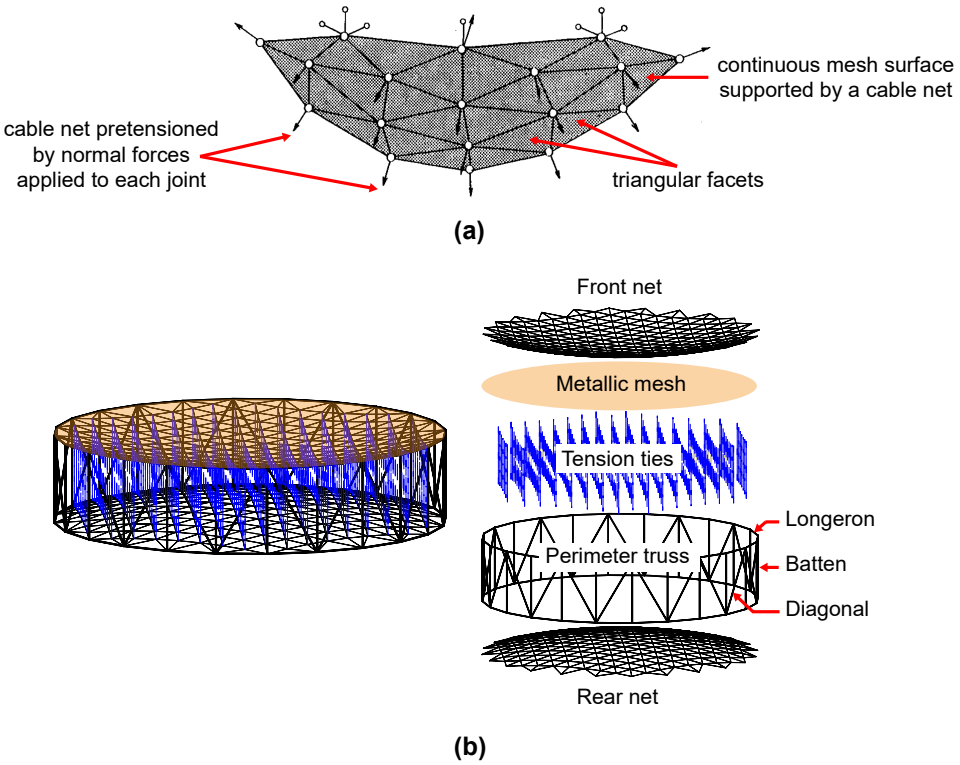

Figure 1.4: Faceted reflective surface: (a) tension truss concept and (b) structural architecture of faceted deployable mesh reflector, based on [40].

A critical aspect in designing mesh reflectors for ISA is the assembly of the reflective surface itself. However, existing robotic systems have yet to explore this challenge. Using traversing robots complicates the assembly process, as it requires managing both the construction of the truss structure and the assembly of the reflective surface simultaneously. Hence, this thesis considers a simpler, fixed robotic system specifically tailored for the assembly of reflectors and similar ring-like structures with a cable interior.

1.4 Feasibility of In-Space Assembly Concepts

As noted in [18], [54], ISA presents a series of challenges that escalate with the increase in the number of structural units and the complexity of installation sequences. Key issues during assembly include ensuring smooth integration of components without snagging or jamming and maintaining structural stability throughout the process. As the size of the structure grows, these challenges become more pronounced, complicating the prediction of component interactions and increasing the risk of interference and misalignment. The greater the number of components, the higher the likelihood of obstructions and delays caused by interference. The sequence of assembly plays a crucial role in facilitating smooth integration and preserving structural integrity, necessitating meticulous planning to avoid misalignments and excessive stresses. Addressing these challenges effectively demands advanced numerical simulations that can accurately model the entire assembly process, track kinematic evolution, and identify potential issues. Such simulations are essential for optimizing the assembly sequence, ensuring the stability and functionality of the structure as it scales and new components are integrated.

Even with reliable simulations, experimental validation of numerical simulation results is still critical to accurately evaluate the feasibility of ISA. However, as systems are scaled to larger size, relying on simulated outcomes becomes essential for assessing the effectiveness of the proposed ISA concept. To build confidence in these simulations, it is vital to ensure that the results align with experimental observations, particularly in smaller-scale cases where experiments are still feasible. This alignment between simulation and experiment serves as a foundational step in confirming the reliability of the models before applying them to larger and more complex systems.

1.5 Thesis Outline

Chapter 2 of this thesis presents a comprehensive and rapid design approach for deployable mesh reflector antennas, based on the state-of-the-art AstroMesh architecture. This design method is then employed to estimate key metrics such as the total mass, stowed volume, and fundamental natural frequency of vibration for antennas with varying aperture diameters and focal lengths, assuming an operational RF of 10 GHz. A detailed analysis is carried out on the distribution of prestress within the inner tension structure by formulating a prestress optimization problem. Analytical scaling laws are then derived for the mass, stowed volume, and natural frequency of optimally prestressed reflectors with aperture diameters up to

200 meters. The study then identifies the maximum achievable aperture diameters for deployable reflector designs based on the constraints of current and near-future launch vehicle capabilities. Additionally, a semi-analytical homogenization model is introduced to estimate the fundamental natural frequencies for various boundary conditions. This model offers accurate and rapid dynamic performance predictions, serving as a more efficient alternative to the use of a high-fidelity model.

Chapter 3 examines the design of mesh reflectors for ISA and assesses their feasibility for stowage within current commercial launch vehicles. This is demonstrated through a detailed scaling study of mass and stowed volume, leveraging the generalized design method introduced in Chapter 2. These ISA mesh reflectors are based on the same structural architecture as deployable reflectors. Building on this analysis, a novel ISA concept for large mesh reflectors is introduced, broadly applicable to ring-like structures with cable interior. A stationary robotic assembly facility is key to this concept, which is folded and stowed in the launch vehicle. Once deployed in space, the facility simultaneously assembles a perimeter truss that expands in diameter with each added unit cell. Boundary nodes of the cable interior are attached to the perimeter truss before each unit cell is released, and the assembly is completed when the facility releases the last unit cell and secures the final node of the cable interior.

Chapter 4 introduces a two-dimensional finite element model to predict the kinematics of large ring-like structures with a prestressed cable interior assembly. This model is utilized to enhance understanding of the proposed ISA concept in Chapter 3 and evaluate design considerations for the stationary robot assembling a ring-like truss. The numerical simulation setup, established using the commercial finite element software ABAQUS/CAE [55], is described along with the modifications and simplifications made to the original designs developed in Chapter 2 to improve computational efficiency. A structure featuring a six-sided perimeter truss and a simple cable interior is used to identify key parameters and techniques for accurate simulation, allowing for the refinement of the developed simulation methods.

Chapter 5 delves into the application of the developed simulation techniques to model the assembly process of a twelve-sided perimeter truss and a network of internal cables that is representative of a reflector antenna. By exploring various assembly sequences and configurations, this chapter aims to gain a comprehensive understanding of the nonsymmetric deployment of the structure, assessing how different approaches influence the overall stability and integrity of the assembly

process, and obtaining the desired final configuration. Key design considerations are examined to improve assembly efficiency and robustness, with particular attention to the strategic positioning of the stationary robot, the management of prestressed cables, and the sequence in which truss components are integrated. These factors are crucial for achieving precise autonomous construction of the target ring-like structure with a cable interior in the challenging environment of space, without human intervention. The simulation results, while showcasing the scalability of the developed techniques, offer valuable insights for optimizing the design and operation of autonomous assembly systems for large-scale space structures.

Chapter 6 provides an overview of a lab-scale prototype developed and tested to validate the proposed ISA concept. The prototype, with its twelve-sided perimeter truss and 1.4 meter-diameter is a continuing endeavor by fellow team members of the DARPA NOM4D project at the Space Structures Laboratory at Caltech. Utilized to experimentally model critical elements of the ISA process, this effort not only serves to confirm the viability of the ISA concept but also acts as a tool for validating the qualitative conclusions drawn from simulations. Successful demonstration of the concept indicates that constructing large, high-precision ring-like structures in space using robotic systems is feasible. Experimental observations are compared with simulation results, and these comparisons reveal that, despite using a two-dimensional model, the simulations effectively capture key effects observed in the experiments, providing valuable insights that inform the prototyping process. This qualitative analysis demonstrates the virtual model's ability to offer crucial guidance and enhance understanding during the development of ISA prototypes, especially as structures increase in size.

Chapter 2

ESTABLISHING THE LIMITS OF DEPLOYABLE REFLECTORS

Article: Scaling Laws for Deployable Mesh Reflector Antennas

This chapter also includes both published work from the following proceedings and new, unpublished sections:

S. P. Dassanayake, J. Suh, M. Thomson, and S. Pellegrino, "Mass, Volume and Natural Frequency Scaling of Deployable Mesh Reflectors," in *AIAA SCITECH 2024 Forum*, 2024, p. 2041. DOI: 10.2514/6.2024-2041.

2.1 Motivation

Consider the structural architecture of the state-of-the-art deployable mesh reflector, AstroMesh illustrated in Fig. 2.1. It is composed of three primary components: two cable nets, a metallic wire mesh, and a deployable perimeter truss. The metallic mesh is attached to the back side of the front cable net, providing a radio-frequency reflective surface that approximates a paraboloid. The accuracy of this approximation depends on the size of the triangular facets, which is determined by the length of the cable elements and the density of nodes on the paraboloid. Both the front and rear cable nets are identical, equally prestressed, and attached to the perimeter truss. Tension ties connecting corresponding node pairs between the front and rear nets provide the normal forces required to achieve the desired paraboloid shape.

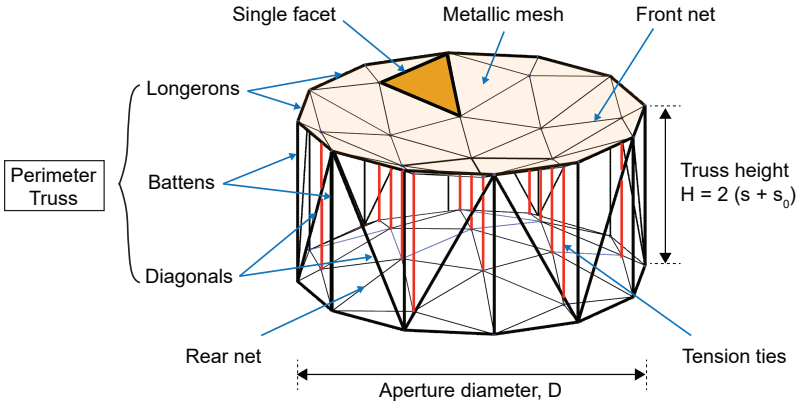

Figure 2.1: Generalized design terminology: structural architecture of faceted deployable mesh reflector.

The deployable perimeter truss consists of identical repeating parallelogram units, each formed by two longerons (i.e., horizontal struts in Fig. 2.1), two battens (i.e., vertical struts in Fig. 2.1), and a diagonal brace that allows for extension when the truss is folded. The truss operates as a cable-actuated, synchronized parallelogram. When stowed, it forms a compact, hollow cylinder, with members secured and preloaded against lightweight hoops that provide stability and debris-protection. This design allows the truss to gently expand upon the release of tie-downs during deployment [40]. The deployed and prestressed structure achieves high stiffness and thermal stability by using high-modulus tubes with a near-zero coefficient of thermal expansion (CTE) for the truss, and thermally stable high-modulus tapes for the cable nets. The reflective surface is made of triangular facets sized according to the operational RF of the reflector. The facet size is chosen

to achieve the required approximation to the paraboloid, quantified by the surface root-mean-square (RMS) error, δ_{RMS}.

As described in Section 1.3, the key metrics for evaluating deployable mesh reflectors include mass and stowed volume (important for launch accommodation), and natural frequency of vibration (related to dynamic performance during operation), which become increasingly significant as the reflector size increases. Despite the importance of mass and stowed volume for large deployable mesh reflectors, systematic studies are lacking, with most research focusing on RF efficiency. Existing studies on dynamics are limited, as high-fidelity models lack computational efficiency.

Given these challenges, this chapter focuses on developing simplified analysis methods that allow for quick estimation of key parameters for deployable reflectors. This approach is not intended to replace more detailed design methods that have been presented elsewhere but serves as a foundation for scaling studies. It extends existing data for deployable mesh reflectors, offering a basis for comparison with reflectors designed for ISA. A general design framework is established for faceted mesh reflector antennas, utilizing a simplified geometric approximation to estimate the maximum facet size and a fundamental approach for designing the facet geometry.

The study then addresses the required connectivity between the edges of the faceted surface and the deployable perimeter truss to ensure that the front cable net can be uniquely prestressed (i.e., to form a statically determinate structure) and maintain a unique (i.e., a kinematically determinate) shape. Once the structure's geometry is determined, the prestress distribution is optimized by adjusting the tension in the ties, and the structural components are sized to provide sufficient safety margins against relevant failure modes.

This design methodology is applied to create deployable center-fed mesh reflectors with an operational frequency of 10 GHz and apertures up to 200 meters in diameter. Scaling laws for mass, stowed volume, and natural vibration frequency are derived, considering various boundary conditions that determine the behavior of reflectors on spacecraft with inertia that is either comparable or much smaller than the reflector. A semi-analytical model is used to significantly reduce computational complexity of numerical analysis compared to fully detailed models.

2.2 Geometry, Connectivity, and Prestress

2.2.1 Geometry and Design for Kinematic and Static Determinacy

A paraboloidal reflective surface is used for maximizing antenna directivity [56]. Figure 2.2 illustrates a circular paraboloid defined by its axis z, aperture diameter D, focal length F, and z-offset s_0. The equation for the surface is:

$$s_0 + \frac{(x^2 + y^2)}{4F^2} = z \tag{2.1}$$

which depends on the key geometric parameter, the F/D ratio, with higher values corresponding to shallower reflectors. This study considers reflector designs with three different values, $F/D = 0.5, 0.7$, and 1.0.

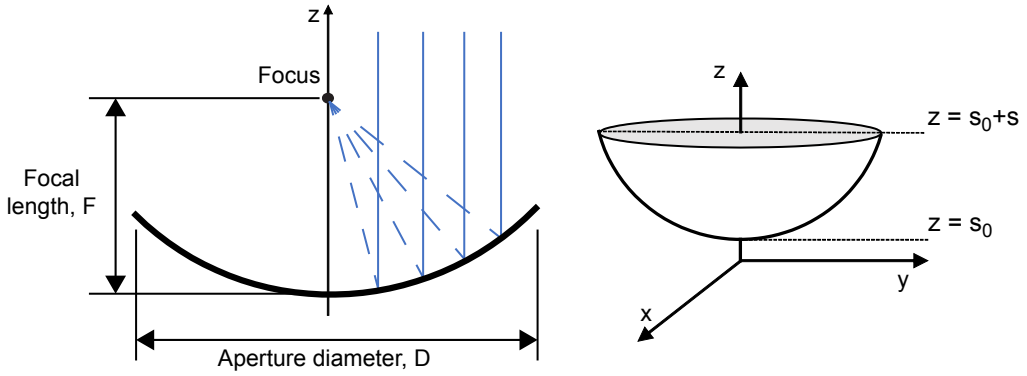

Figure 2.2: Geometry of paraboloidal reflector.

For designing a faceted surface, it is convenient to approximate the paraboloid with a surface of uniform curvature, a sphere. The spherical cap that aligns with the apex and edge of the paraboloid has a radius R as described in [57] and is given by:

$$R = 2F + \frac{D^2}{32F}. \tag{2.2}$$

The required size of the triangles for smooth approximation of the reflector surface is then estimated by analyzing the geometric deviation between a spherical surface of radius R and an equilateral triangle of side length L, whose vertices lie on the curved surface. This RMS error of the facet, described in [58] is given by:

$$\delta_{facet} = \frac{L^2}{8\sqrt{15}R} \tag{2.3}$$

and is used to calculate the appropriate facet size for a given R and F/D.

When a tessellation of equilateral triangles of side length L in the $x-y$ plane is vertically projected onto a paraboloid, the facets increasingly elongate as they move away from the z-axis. However, this elongation is minimal for relatively flat reflectors and small L/D ratios.

In this study, geometric faceting is considered the only source of error, neglecting other potential error sources, such as thermal distortions, spillover, aperture taper, cross polarization, etc. The RMS surface error is therefore set equal to the faceting error in Eq. 2.3, i.e., $\delta_{RMS} = \delta_{facet}$. For a reflector operating at 10 GHz, with an error limit of $\lambda/50 = 0.6$ mm, the maximum allowable facet size is calculated using Eqs. 2.2 and 2.3. It is important to note that the lengths in Eq. 2.3 are not the unstressed lengths of the cable net elements, but account for the elastic stretching caused by prestress.

Figure 2.3(a) shows how the facet size varies with different F/D ratios. Larger facets are feasible for higher F/D values as they correspond to shallower reflectors for the same aperture size. As a general rule, the maximum facet size increases proportionally to $\sqrt{D}$. Figure 2.3(b) shows the net configuration, where, after selecting a facet size for the given aperture and F/D, the number of subdivisions n in the hexagonal tessellation is calculated using the relationship:

$$n = 0.5D/L. \tag{2.4}$$

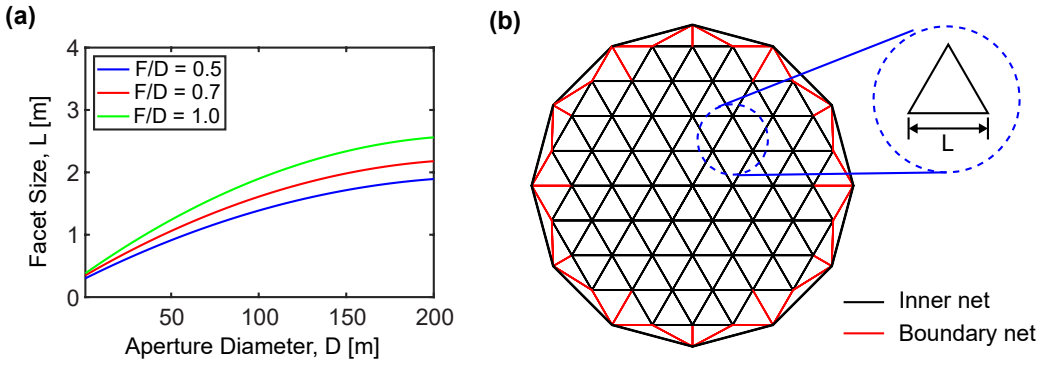

Figure 2.3: Faceting of paraboloidal surface: a) variation of facet size with diameter and b) schematic layout of net.

The front and rear reflector nets consist of *inner net* cables forming the regular hexagonal tessellation, indicated by black solid lines in Fig. 2.3(b) and *boundary net* cables connecting the triangles to the perimeter truss, indicated by red solid lines in Fig. 2.3(b). The inner net consists of *free nodes* connected by tension ties between

the front and rear nets. Although the inner net geometry is unique for a given facet size, the boundary net design can vary based on the number of bays in the perimeter truss and the number of connection points between the perimeter truss and the inner net. Figure 2.4 presents three different boundary net designs with identical number of edge subdivisions ($n = 7$), but varying connections between perimeter truss nodes and free nodes. It is important to note that in the design of the boundary cables, it is assumed that each node of the perimeter truss is connected to an equal number of free nodes, denoted as n_c. The number of subdivisions in one-sixth of the perimeter truss is denoted by n_t. A similar approach was previously adopted in [59].

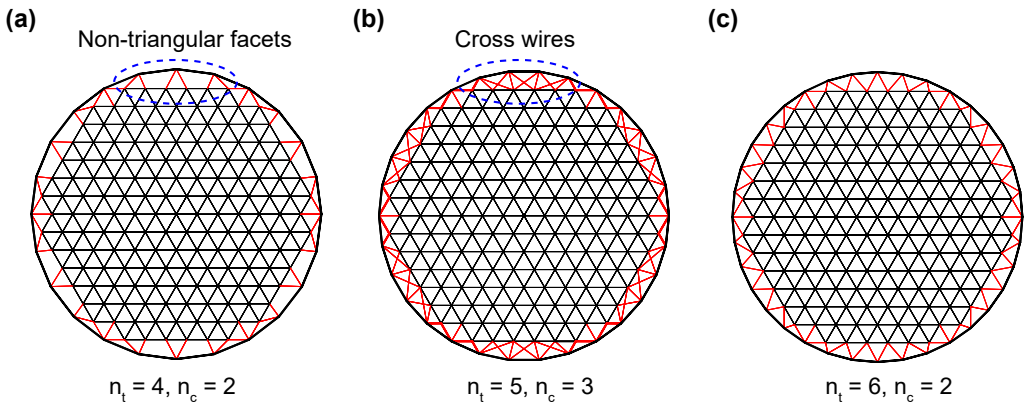

Figure 2.4: Three different net configurations with a) non-triangular facets, b) cross wires, and c) complete triangular tessellation.

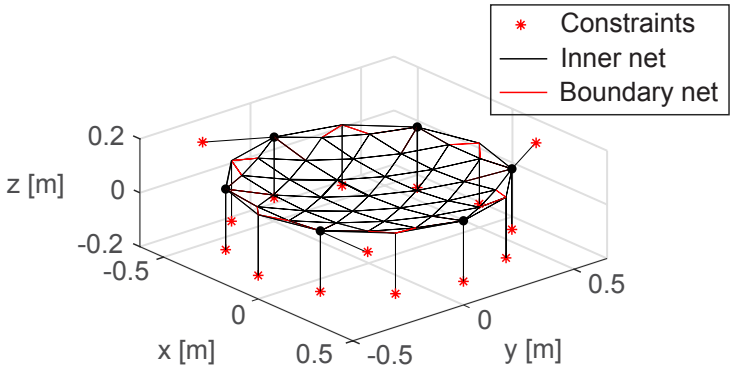

Figure 2.5: Pin-jointed bar model of front net for $n = 3, n_t = 2, n_c = 2$.

To ensure that the reflector has a unique shape and prestress distribution, the degrees of kinematic and static determinacy are analyzed using the pin-jointed bar model of each cable net, as depicted in Fig. 2.5. This analysis, based on Maxwell's

extended equation and equilibrium matrix rank [4], [60], [61], shows that these properties depend on the net geometry. For example, non-triangular facets (Fig. 2.4(a)) result in a kinematically indeterminate structure, while cross-wired boundary nets (Fig. 2.4(b)) lead to static indeterminacy. Only configurations with triangular facets and no cross-wires (Fig. 2.4(c)) are both kinematically and statically determinate, making them the preferred choice for the structural architecture of the reflector.

For reflectors designed in this manner, the number of subdivisions of the hexagonal tessellation is related to the number of free nodes connected to each node of the perimeter truss and the subdivision of the perimeter truss by the relationship:

$$n - 2 = (n_t - 1)\,(n_c - 1)\,. \tag{2.5}$$

In this study, the perimeter truss is designed to have half the density of the net, with each batten supporting three free nodes through boundary cables (i.e., $n_c = 3$ in Eq. (2.5)). The lengths of the truss members; longerons, battens, and diagonals, are determined based on the designed net geometry.

2.2.2 Prestress Optimization of Cable Nets

Optimizing the prestress of the reflector is crucial since the prestress directly impacts the structural mass. A higher prestress leads to increased loading on the structural elements, which in turn requires them to be larger and therefore heavier. This effect is particularly pronounced in the elements of the perimeter truss that experience compression due to prestress. It will be demonstrated that, for large-diameter reflectors, designs utilizing optimal prestress are substantially lighter compared to those with non-optimized prestress.

Given the structure's statically determinate design, the prestress distribution is uniquely defined by the equilibrium equations for the nodes once the tension tie forces are applied. For example, the equilibrium equation in the x-direction for each free node, i, connected to N nodes, j, is (see [4] for more details) given by:

$$\sum_{j}^{N} \frac{x_i - x_j}{L_{ij}} p_{ij} = t_{i,x} \tag{2.6}$$

where,
L_{ij} is the length of cable ij, and hence $L_{ij} = \sqrt{\left(x_i - x_j\right)^2 + \left(y_i - y_j\right)^2 + \left(z_i - z_j\right)^2}$;
p_{ij} is the tension in cable ij;
$t_{i,x}$ is the component of the tension tie force applied to node i, in the x-direction.

The simplest approach involves computing the prestress for a single tension tie force value at all free nodes. However, this method results in several cables near the transition between the inner and boundary nets being under compression (and in practice, slack). To achieve a purely tensile prestress distribution, the tie forces at the free nodes in the transition region must be increased by a suitable factor, $\alpha > 1$, from their nominal value.

Figure 2.6(a) illustrates the prestress distribution in the cable net for $D = 200$ m, $F/D = 1.0$, and $\alpha = 1.7$. This value was determined through trial and error. This approach of applying two distinct tie forces led to a reduction in overall structural mass, suggesting that further mass reduction could be achieved through a more formal optimization of general prestress distributions.

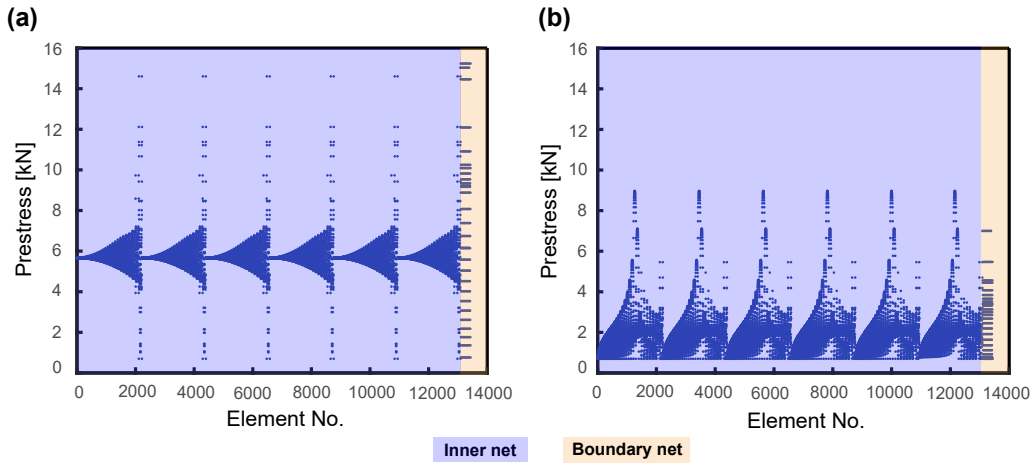

Figure 2.6: Comparison of cable prestress distributions for $D = 200$ m, $F/D = 1.0$ corresponding to (a) 2 distinct tension tie forces, and (b) $(n + 1)$ rings of tension tie forces.

Theoretically, varying the tie forces at each free node could be explored, but this is impractical. To simplify practical implementation, six-fold rotational symmetry of the hexagonal tessellation was assumed. Therefore, the number of distinct tension tie forces was set to the number of *rings* (see Fig. 2.7) in the tessellation, i.e., $n+1$. This approach can be extended to offset reflectors, for which the assumption of six-fold symmetry is not valid, by considering larger sets of cable tensions for each ring of tension tie forces.

A basis for independent tension tie forces, T, was considered by computing the distribution T^k that corresponds to unit tension tie forces at all free nodes on ring k and zero forces at all other free nodes. Denoting the resulting prestress distribution

in equilibrium with T^k as P^k, the following two matrices were defined:

$$T = \left[\underline{T}^1 \ \underline{T}^2 \ \cdots \ \underline{T}^{n+1}\right] \tag{2.7a}$$

$$P = \left[\underline{P}^1 \ \underline{P}^2 \ \cdots \ \underline{P}^{n+1}\right]. \tag{2.7b}$$

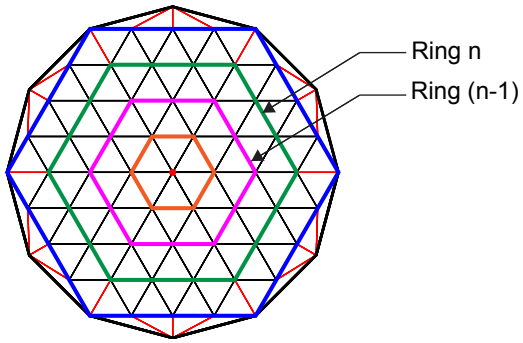

Figure 2.7: Definition of *rings* in inner net.

A general tie force distribution is $T\alpha$, with corresponding cable tensions p_{ij} given by $P\alpha$, where the coefficients $\alpha_k > 0$ to ensure that all tension tie forces are positive.

An additional constraint is that a sufficient level of pretension must be applied to all cables to keep them both under tension and sufficiently straight when loaded by the prestressed metallic mesh. The minimum required tension is [62]:

$$p_{ij} \geq 10\sigma L_{max} \tag{2.8}$$

where,
σ is the biaxial prestress in the metallic mesh;
L_{max} is the maximum cable length in the net.

Different objective functions were evaluated for optimization using MATLAB's *fmincon* function, focusing on two metrics: the maximum compressive forces in the perimeter truss and the range of cable tensions, $\frac{(P)_{max}}{(P)_{min}}$. Both metrics contribute directly to the overall structural mass, as discussed in Sections 2.3 and 2.4. The results, presented in Table 2.1, show that all variants considered improve both metrics. Remarkably, five out of seven different objective functions resulted in a 32% reduction in mass and a 41% reduction in the range of cable tensions. Among these, the average batten force in the perimeter truss was chosen as the objective function for prestress optimization.

Visual comparison of the cable force distribution for the initial two-tension tie force solution, Fig. 2.6(a), with the optimal distribution obtained in this manner, Fig. 2.6(b), for $\sigma = 5$ N/m is interesting. It reveals that the optimal solution results in significantly lower cable tensions.

Table 2.1: Comparison of Objective Functions for $D = 200$ m, $F/D = 1.0$

Objective Function	$\frac{P_{max}}{P_{min}}$	Maximum Compressive Force (kN)	Mass (kg)
RMS Deviation of cable tensions	10.546	145.25	13,259
Range of cable tensions	10.027	138.71	13,039
Maximum longeron force	12.816	138.42	13,030
Average longeron force	12.816	138.42	13,030
Maximum batten force	12.816	138.42	13,030
Average batten force	12.816	138.42	13,030
Sum of tension tie forces	12.816	138.42	13,030
Solution with two distinct tension tie forces	21.775	379.47	19,061

2.2.3 Potential Modifications to the Minimum Tension Requirement

In Eq. 2.8, the minimum tension requirement for the cable elements is governed by the maximum cable length in the net, L_{max}, for a given σ. Examining the original net configuration for $D = 100$ m in Fig. 2.8(a) reveals that L_{max} is predominantly determined by the boundary cable elements, regardless of the subdivision n of the central hexagon.

One possible modification to address this issue is to shift the outermost rings of the central hexagon outward (see [63] for similar approaches). This was attempted, as shown in Fig. 2.8(b), by positioning the centers of the two outermost ($n + 1$ and n) cable rings at one-third of the maximum radial distance between the $n - 1^{th}$ ring and the perimeter truss, while distributing the remaining nodes equally in the radial direction. Mapping the tessellation in this manner preserves the original configuration of the perimeter truss, along with its static and kinematic determinacy, while maintaining the surface accuracy dictated by the subdivision n in the central hexagon. At the same time, it enhances the surface accuracy in the boundary net. However, if all cable net rings are shifted outward, as shown in Fig. 2.8(c), the surface accuracy at the center is compromised, and the fabrication of the cable net becomes more complex due to the lack of straight cable elements running across the entire diameter, unlike the nets in Figs. 2.8(a) and (b).

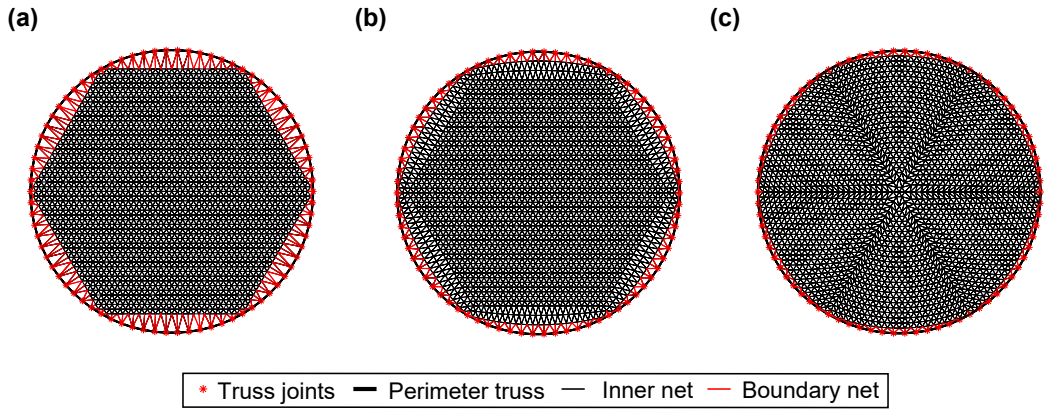

Figure 2.8: Cable net configuration for $D = 100$ m, $n_t = 13, n_c = 3$: a) original configuration, b) mapped configuration 1, and c) mapped configuration 2.

Table 2.2 presents the optimization results for the prestress distributions, comparing the original cable net configuration with the mapped version shown in Fig. 2.8(b). The objective function used for this comparison is the average batten force, as chosen in Section 2.2.2. The results demonstrate that reducing L_{max}, and consequently lowering the minimum tension requirement, leads to a substantial reduction in key metrics of interest, including structural mass. Although this mapping approach offers no advantages for smaller apertures, the benefits are significant for larger apertures, as shown in the results for $D = 200$ m.

Table 2.2: Comparison of cable net configurations for $D = 100, 200$ m, $F/D = 1.0$

Cable net configuration	Radius of Longeron (mm)	$\frac{P_{max}}{P_{min}}$	Maximum Compressive Force (kN)	Mass (kg)
$D = 10$ m				
Original	6.145	3.308	1.07	22.5
Mapped	6.297	4.338	1.15	22.9
$D = 100$ m				
Original	45.434	6.060	29.18	2,479
Mapped	38.956	6.598	18.40	2,184
$D = 200$ m				
Original	94.102	12.816	138.42	13,030
Mapped	68.742	10.060	53.96	9,815

However, the original cable net configuration was chosen for the rest of the analysis presented in this thesis due to its much simpler fabrication of the inner net using only straight cable elements, compared to the complex mapped version.

2.3 Structural Design

2.3.1 Metallic Mesh and Cable Net Design

For the reflector design, a knitted gold-plated molybdenum wire mesh with an areal density $\rho_{mesh} = 0.025$ kg/m^2 was chosen, with a biaxial prestress $\sigma =$ 5 N/m. The front and rear nets are composed of thin CFRP (carbon fiber reinforced polymer) strips made from M55J carbon fiber in a thermoplastic matrix [64]. This composite material has a density $\rho_n = 1,786$ kg/m^3 and a longitudinal modulus $E_n = 325.4$ GPa. A rectangular cross section of 6 mm width and 150 μm thickness was selected for all reflector apertures. The smallest separation between the front and rear nets (denoted $2s_0$) was kept constant at 0.1 m across all reflector designs considered in this study, as larger separations would increase the batten lengths. The pretension in the cable nets was derived from the optimization process described in Section 2.2.2. Using the net prestress, the resulting compression forces in the perimeter truss were determined through the equilibrium equations of the truss joints. The prestress analysis results for reflectors with apertures $D = 10$ m, 100 m, and 200 m are presented in Table 2.3.

Table 2.3: Prestress range (Nets: tension; Truss: compression), for $F/D = 1.0$

	Nets (kN)		Truss (kN)	
D(m)	Inner net	Boundary net	Longerons	Battens
10	0.042 ~ 0.114	0.045 ~ 0.139	0.947 ~ 1.072	0.046 ~ 0.052
100	0.357 ~ 2.160	0.357 ~ 1.838	25.794 ~ 29.182	0.484 ~ 0.567
200	0.700 ~ 8.967	0.700 ~ 7.000	120.220 ~ 138.420	1.545 ~ 1.859

2.3.2 Perimeter Truss Design

Due to the significant compressive forces acting on the perimeter truss, tubes with circular cross sections were selected for all structural members. A minimum diameter of 5 mm was chosen to avoid impractically small tube sizes.

Assuming pin-ended conditions, the global critical buckling load, P_{cr}, for a thin-walled circular tube with length l, cross-sectional radius r, and thickness t is given by:

$$P_{cr} = \frac{\pi^3 r^3 t E}{l^2} \tag{2.9}$$

where E is the longitudinal modulus.

The longerons, which experience the highest compressive forces, were sized first. Their thickness was set to 1.0 mm, and the radius was calculated using Eq. 2.9,

with a safety margin of 2. The battens and diagonals were then designed with the same cross-sectional radius as the longerons to simplify and lighten the joints of the perimeter truss. The minimum thickness for the battens was set at 1.25 mm, and it was confirmed that the buckling load from Eq. 2.9 exceeded the compressive forces acting on them.

Although the diagonals theoretically do not experience compression, they are loaded in bending during deployment. Thus, their size was simply set to match the longerons, but with a thickness of 0.75 mm.

The radius and thickness values for the longerons, battens, and diagonals for reflectors with apertures D = 10 m, 100 m, 200 m are presented in Table 2.4.

Table 2.4: Size of perimeter truss members, for $F/D = 1.0$

D(m)	Radius of Longeron/ Batten/Diagonal (mm)	Thickness of Longeron (mm)	Thickness of Batten (mm)	Thickness of Diagonal (mm)
10	6.15	1.00	1.25	0.75
100	45.43	1.00	1.25	0.75
200	94.10	1.00	1.25	0.75

2.3.3 Joint Design

The mass of the perimeter truss joints was estimated for a general aperture D and varying values of F/D using a parametric design process based purely on geometry. The structure consists of two types of joints: Type-1, which connects five structural elements (longeron, diagonal, batten, diagonal, and longeron), and Type-2, which connects three structural elements (longeron, batten, and longeron), as illustrated in Fig. 2.9(a).

The general configuration of both joint types is depicted in Figs. 2.9 and 2.10. The design features two parallel plates made of CFRP (with the same material properties as the struts and cable net elements) connected centrally to a plate made of 6061 aluminum alloy (ρ_{Al} = 2700 kg/m^3, E_{Al} = 69 GPa). This central plate is securely fastened to the batten, while the longerons and diagonals are attached to appropriate locations on the side plates via 6061 aluminum alloy sleeves and steel pins and bolts (ρ_S = 7800 kg/m^3, E_S = 210 GPa). These connections allow rotational movement, facilitating stowage and deployment.

Once the diameter of the longerons was determined, as discussed in Section 2.3.2, the positions of the pins attaching the longerons and diagonals to the plates were

meticulously planned to ensure adequate clearance, allowing the members to rotate freely around the pins. Note that the battens are rigidly connected to the joints. The thicknesses of the plates and sleeves were selected based on allowable margins for hole bearing failure at the pin attachments (~thickness ≥ 3× hole diameter [65]).

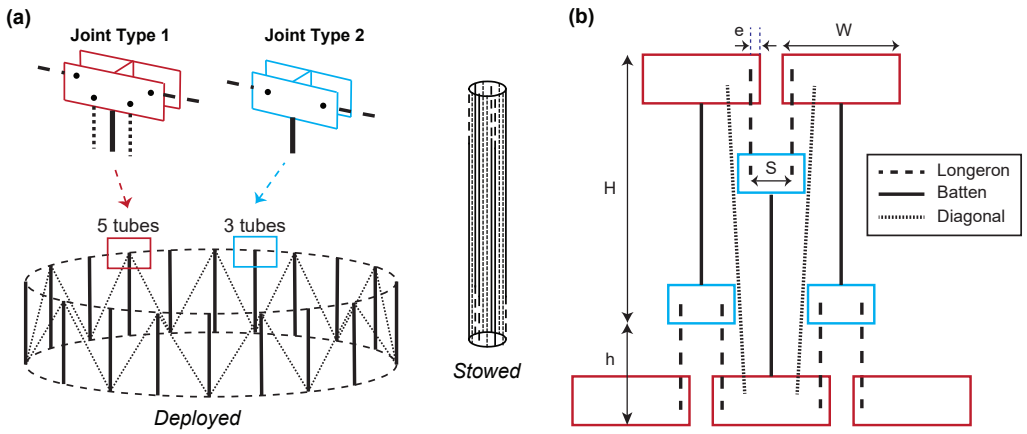

Figure 2.9: Perimeter truss: a) fully deployed and stowed configurations, and b) relative position of members in stowed configuration.

Both joints were designed with the CAD software SolidWorks and the mass of each joint type was obtained from SolidWorks. Figure 2.10 shows the Type-1 and Type-2 joints and the end sleeves that stiffen the tubular elements.

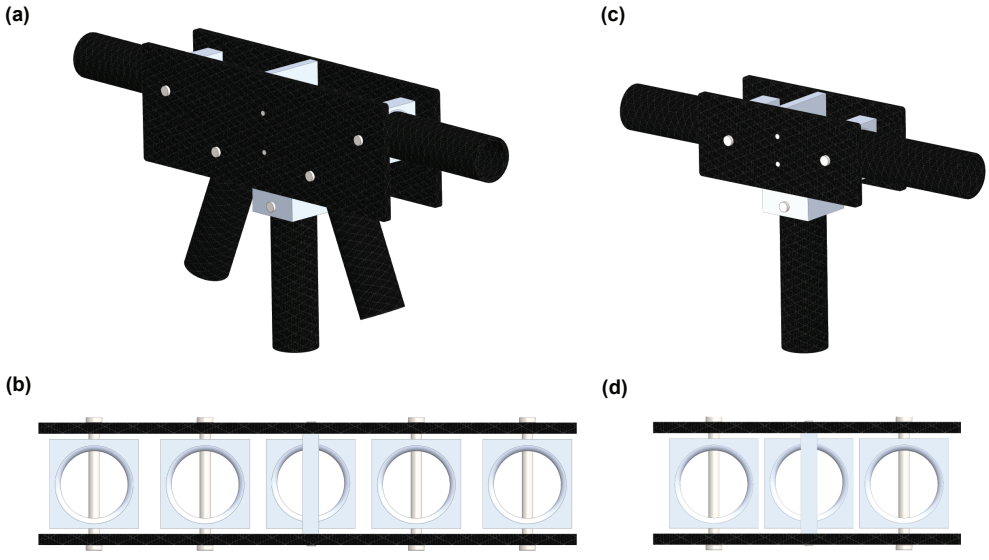

Figure 2.10: CAD images of a) Type-1 joint with 5 struts, b) Type-1 joint strut sleeves, c) Type-2 joint with 3 struts, and d) Type-2 joint strut sleeves.

The mass of the joints for apertures of D = 1 m, 10 m, 100 m, and 200 m, and F/D = 1.0, is presented in Table 2.5.

Table 2.5: Joint masses for F/D = 1.0

	Joint Mass (g)	
D(m)	Type-1	Type-2
1	18.0	10.3
10	45.2	23.2
100	2, 272	1, 076
200	10, 780	5, 284

2.4 Scaling of Mass and Volume

2.4.1 Estimating Mass and Stowed Volume

The total mass of the reflector was estimated by summing the contributions from the cable nets (m_n), metallic mesh (m_{mesh}), perimeter truss (m_{truss}), tension ties (m_{tt}), joints (m_j), and deployment actuators (m_{dep}):

$$m_{total} = m_n + m_{mesh} + m_{truss} + m_{tt} + m_j + m_{dep}. \tag{2.10}$$

The mass of each component was calculated based on the structural design described in Section 2.3. The mass of the cable net was determined from the cross-sectional area of the strips, multiplied by their total length and material density. The metallic mesh mass was calculated assuming full coverage of the front net's surface, where the area of the paraboloid was multiplied by the mesh's areal density. The perimeter truss mass was derived from the design of the longeron, batten, and diagonal members, as detailed in Section 2.3.2. The mass of the joints was estimated by linear interpolation of the values in Table 2.5. For the tension ties and seams in the mesh, m_{tt}, it was assumed to be twice the mass of the metallic mesh ($2\times m_{mesh}$). The mass of the deployment actuators was assumed to be 10% of the total reflector mass.

The stowed envelope of the reflector was assumed to be of cylindrical shape, as illustrated in Fig. 2.9(a). The diameter of this cylinder is determined by the perimeter of the stowed configuration, where adjacent joints are in contact. The height of the cylinder is defined by the lengths of the battens and longerons. Figure 2.9(b) presents a schematic showing the relative positions of the truss members at the joints and the design parameters influencing the stowed dimensions. In Fig. 2.9(b), H represents the total height of the fully deployed perimeter truss, while h defines the distance between the bottom edges of the Type-1 and Type-2 joints in the folded

configuration. The length of a Type-1 joint, the distance between the center of the hinge of the longeron and the edge of the joint, and the distance between the centers of the hinges of the longerons in a Type-2 joint are defined as W, e, and S, respectively. The perimeter of the stowed reflector P_{stowed} is then calculated as:

$$P_{stowed} = (W + S - 2e) \times (3n_t) \tag{2.11}$$

and then the diameter in the stowed configuration is given by $D_{stowed} = P_{stowed}/\pi$. The height of the stowed configuration is $H_{stowed} = H + h$.

2.4.2 Mass and Stowed Dimensions Results

The variation in the equivalent areal density of different reflector components is plotted in Fig. 2.11 against the aperture size, for $F/D = 1.0$. A comparison of the two graphs highlights the superior mass efficiency achieved with the optimal prestress distribution. For the design with two distinct tension tie forces (Fig. 2.11(a)), the areal density increases nonlinearly as the reflector diameter grows. This is mainly due to the rapidly rising mass of the battens and diagonals in the perimeter truss. In contrast, the design with the optimal prestress distribution, shown in Fig. 2.11(b), results in smaller compressive forces in the perimeter truss compared to the two-tension design. The difference between the two approaches is minimal for apertures below 50 m but, as the diameter increases, the lower prestress in the truss leads to smaller member sizes and nearly a one-third reduction in areal density for apertures around 200 m.

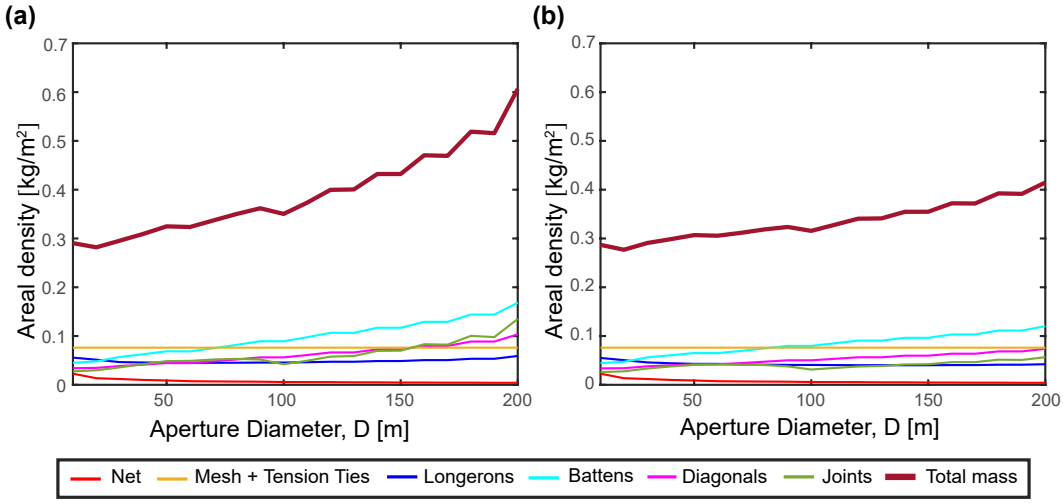

Figure 2.11: Areal density of reflector components ($F/D = 1.0$): a) non-optimal prestress design, and b) optimal prestress design.

Figure 2.12 presents the overall mass, stowed diameter, and height of the reflector for $F/D = 1.0$ across a diameter range of 10 m to 200 m.

Two launch vehicles, Falcon Heavy [66] and Starship [67], were selected to assess the feasibility of launching large-aperture mesh reflectors. In Fig. 2.12(b) and (c), the pink and blue solid lines represent the payload capacity limits for Falcon Heavy and Starship, respectively. According to the respective Users' Guides, the maximum payload mass limits to geostationary transfer orbit (GTO) are 26, 700 kg for the Falcon Heavy and 21, 000 kg for the Starship. Even the largest reflectors considered in this study remain well within these mass limits. However, launch envelope constraints, particularly the stowed diameter, are much stricter. Reflectors with apertures larger than 70 m exceed Falcon Heavy's payload capacity, while 100 m is the maximum aperture limit for launch aboard Starship.

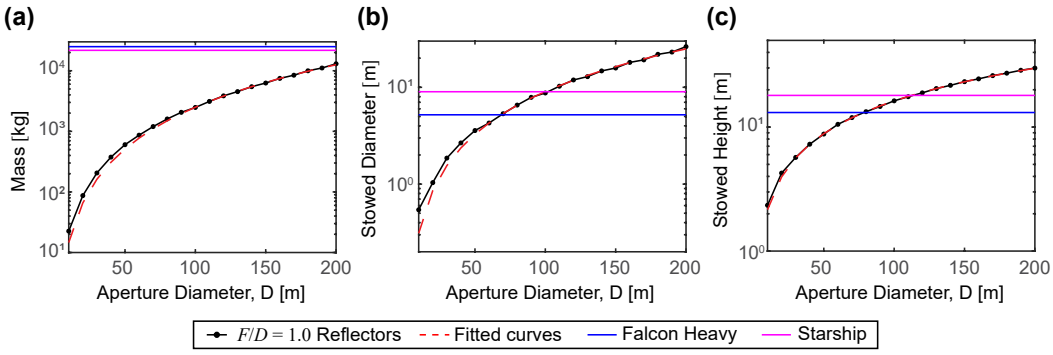

Figure 2.12: Scaling of deployable reflectors for $F/D = 1.0$: a) total mass, b) stowed diameter, and c) stowed height.

This scaling analysis provides valuable insights into the challenges of launching large-scale deployable mesh reflectors, showing that launch feasibility is primarily constrained by the stowed diameter of the reflector, followed by its height. The launch mass limit, in contrast, is not as restrictive. Given that extremely large space-borne deployable reflectors are impractical within current launch vehicle limitations, there is a clear need to explore alternative strategies, such as on-orbit assembly, to overcome these volumetric payload constraints.

2.4.3 Analytical Scaling Laws

The results presented in Section 2.4.2 can be used to establish analytical scaling laws for the mass and stowed envelope of deployable mesh reflectors designed with the optimized prestress distribution described in Section 2.2.2.

To derive a mass scaling equation, the reflector components were categorized into three groups that scale similarly according to the structural design procedure; the mass of the perimeter truss including the joints, the mass of the cable net, and the mass of the mesh and tension ties. Each mass category was expressed as a separate power function of the aperture diameter D, as illustrated in Fig. 2.13. The mass data of each category were fitted to this power law using MATLAB's curve fitting algorithm, ensuring a 95% confidence interval for the results. The coefficients of the power law terms, c_1, c_3 and c_5, were scaled to reflect the mass of the deployment actuators, which was set at 10% of the total mass. The resulting scaling law for the mass (in kg) of reflectors with $F/D = 1.0$ is:

$$m_{total} = 0.022D^{2.452} + 0.054D^{1.492} + 0.067D^2. \tag{2.12}$$

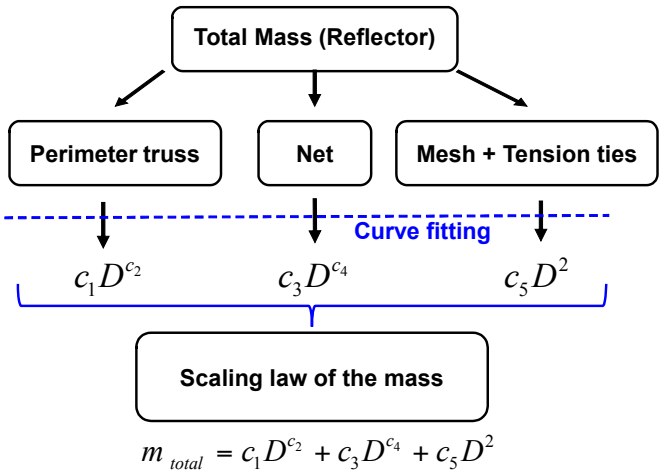

Figure 2.13: Process of establishing a scaling law for the total mass.

The perimeter truss is clearly the largest contributor to the mass, with $c_2 > 2$, followed by the mesh and tension ties, and finally the cable net. Figure 2.12(a) plots the detailed mass of reflectors with $F/D = 1.0$ alongside this analytical expression, demonstrating that Eq. 2.12 closely follows the total mass of the reflector.

When considering the stowed diameter and height of the deployable reflector, the contributions from the cable nets, mesh, and tension ties are negligible, see Fig. 2.9. Instead, the stowed envelope size is primarily influenced by the perimeter truss members and joints. Consequently, single-term power functions were used to derive the following analytical expressions for the diameter and height:

$$D_{stowed} = 0.011D^{1.464} \tag{2.13}$$

$$H_{stowed} = 0.286D^{0.877} \tag{2.14}$$

which have been plotted in Fig. 2.12(b) and (c).

2.4.4 Scaling Studies for Deeper Reflectors

Mass and stowed volume scaling plots for $F/D = 0.5, 0.7$, generated using the same overall design methodology, are presented in Fig. 2.14. The corresponding joint masses for apertures of $D = 1$ m, 10 m, 100 m, and 200 m are listed in Table 2.6. In the plots, black circular dots and red crosses represent the quantities calculated for $F/D = 0.5$ and $F/D = 0.7$ reflectors, respectively.

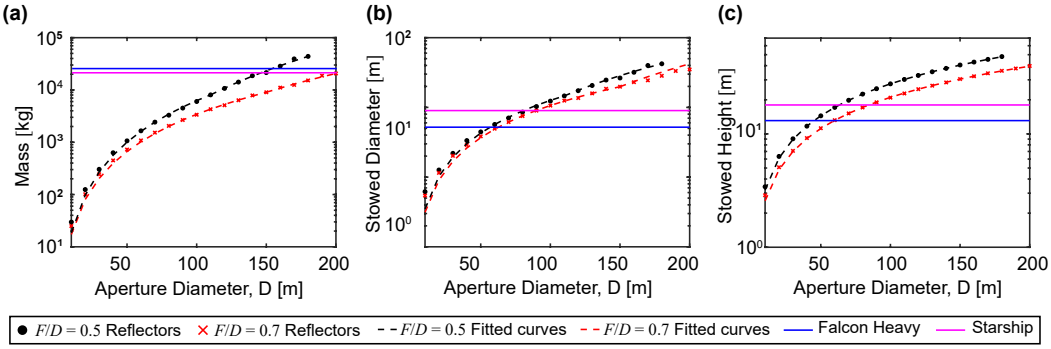

Figure 2.14: Scaling of deployable reflectors for $F/D = 0.5$ and 0.7: a) total mass, b) stowed diameter, and c) stowed height.

Table 2.6: Joint masses for $F/D = 0.5, 0.7$

	Joint Mass (g)			
	$F/D = 0.5$		$F/D = 0.7$	
D(m)	Type-1	Type-2	Type-1	Type-2
1	18.0	10.3	18.0	10.3
10	40.5	21.2	45.2	23.2
100	2,343	1,107	2,217	1,051
200	18,448	9,290	15,381	7,687

These plots show that both the mass and stowed envelope increase as the reflectors become deeper, i.e., as F/D decreases. Reflectors with $F/D = 0.5$ and aperture diameters greater than 140 m are constrained by the payload mass capability of the launchers. As with the $F/D = 1.0$ case, the primary challenge is not the mass,

but the launch envelope restrictions. However, for $F/D = 0.5$ and $F/D = 0.7$, the stowed height becomes the most restrictive factor, as opposed to the stowed diameter, due to the increased depth of the cable nets. For reflectors with $F/D = 0.5$, an aperture diameter of 50 m is the limit for the Falcon Heavy, while the Starship can accommodate up to 60 m. For $F/D = 0.7$, the aperture limit increases to 60 m for the Falcon Heavy and 80 m for the Starship.

Analytical scaling laws for the mass and stowed envelope of reflectors with $F/D = 0.5$ and $F/D = 0.7$ were established using a similar approach to that used for $F/D = 1.0$, which involves grouping reflector components into three distinct categories. However, it was observed that reflectors with $n \geq 32$ exhibit different trends compared to those with $n < 32$. As a result, separate analytical expressions were formulated for each case, and are plotted on Figs. 2.14(a-c). Specifically, for $F/D = 0.5$, reflectors with $D \geq 110$ m have $n \geq 32$, while for $F/D = 0.7$, reflectors with $D \geq 150$ m have $n \geq 32$.

The analytical expressions for the total mass (m_{total}), stowed diameter (D_{stowed}), and stowed height (H_{stowed}) for $F/D = 0.5$ are as follows:

$$
\begin{aligned}
m_{total} &= \begin{cases} 0.014 \times D^{2.767} + 0.064 \times D^{1.5} + 0.063 \times D^2 & (n < 32) \\ 0.003 \times D^{3.572} + 0.064 \times D^{1.5} + 0.063 \times D^2 & (n \geq 32) \end{cases} \\
D_{stowed} &= \begin{cases} 0.0097 \times D^{1.557} & (n < 32) \\ 0.0006 \times D^{2.155} & (n \geq 32) \end{cases} \\
H_{stowed} &= \begin{cases} 0.370 \times D^{0.9368} & (n < 32) \\ 0.363 \times D^{0.9411} & (n \geq 32). \end{cases}
\end{aligned}
\tag{2.15}
$$

The analytical expressions for the total mass (m_{total}), stowed diameter (D_{stowed}), and stowed height (H_{stowed}) for $F/D = 0.7$ are as follows:

$$
\begin{aligned}
m_{total} &= \begin{cases} 0.024 \times D^{2.500} + 0.059 \times D^{1.485} + 0.061 \times D^2 & (n \leq 32) \\ 0.002 \times D^{3.052} + 0.059 \times D^{1.485} + 0.061 \times D^2 & (n \geq 32) \end{cases} \\
D_{stowed} &= \begin{cases} 0.00922 \times D^{1.531} & (n \leq 32) \\ 0.00004 \times D^{2.633} & (n \geq 32) \end{cases} \\
H_{stowed} &= \begin{cases} 0.319 \times D^{0.910} & (n \leq 32) \\ 0.294 \times D^{0.926} & (n \geq 32). \end{cases}
\end{aligned}
\tag{2.16}
$$

2.5 Scaling of Natural Frequencies of Vibration

2.5.1 Finite Element Model and Boundary Conditions

A geometrically nonlinear, high-fidelity finite element model was developed in ABAQUS/CAE 2017 to analyze the natural frequencies of vibration for deployable mesh reflectors. The model incorporated all structural components, each individually represented, as described below.

The front and rear nets were modeled using truss elements (T3D2), where each edge of a triangular facet consisted of a single truss element. The perimeter truss members—longerons, battens, and diagonals—were modeled with 20 beam elements (B31). Pin joints, allowing relative rotation, were used to connect adjacent elements. The metallic mesh was represented as point masses distributed across the nodes of the front net. Additionally, the mass of the joints and deployment actuators was modeled as point masses connected to the joints of the perimeter truss. A PREDEFINED STRESS FIELD was assigned, corresponding to the prestress levels for each structural component, as determined in the optimization process in Section 2.2.2. Tension tie forces were applied to the inner nodes of both the front and rear nets. The model was set up in the operational geometric configuration of the reflector, with the prestress applied, ensuring minimal geometry changes during the geometrically nonlinear iteration to reach the prestressed equilibrium configuration.

The first step involved performing a static equilibrium analysis under the predefined stress field and tension tie forces. This provided the deformed geometry and stiffness of the reflector. A subsequent modal analysis was then carried out for the structure under the boundary conditions of interest and at equilibrium, to determine the natural frequencies and their corresponding mode shapes.

Two boundary conditions were considered. The first assumed that the reflector was attached to a massive spacecraft via a *prime batten*, designed to avoid interference with the perimeter truss deployment. This batten, shown in Fig. 2.15(a), was connected to the perimeter truss at three joints in the upper truss layer and one joint in the lower layer. In ABAQUS, this batten-supported boundary condition was implemented by restricting the six degrees of freedom (DoFs) at these four joints, as depicted in Fig. 2.15(b).

The second boundary condition assumed a free-free scenario, capturing the increasing dominance of the reflector's dynamics relative to the spacecraft as its size increases.

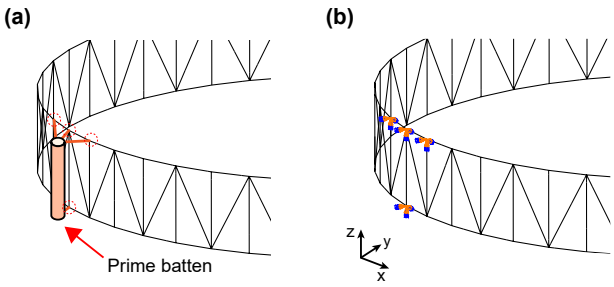

Figure 2.15: Batten-supported boundary condition: a) prime batten, and b) boundary conditions in finite element model.

2.5.2 Natural Frequencies and Mode Shapes

Key results from the finite element modal analysis for reflectors with $F/D = 1.0$ are presented in Fig. 2.16. The log-log trend for the lowest natural frequencies, shown in Fig. 2.16(a), forms a straight line with a negative slope, indicating that the frequencies follow a negative power law as the reflector diameter increases. Typical mode shapes are illustrated in Fig. 2.16(b) and Fig. 2.16(c), respectively, for the batten-supported and free-free boundary conditions.

For the batten-supported boundary condition, two dominant mode shapes emerge: a lateral mode, where the structure rotates around the prime batten, and a vertical mode, where the structure behaves as a cantilever, moving primarily in the z-direction as it vibrates up and down. The natural frequencies of these modes are rather close to each other, with the vertical mode being dominant for reflectors with $D < 25$ m, while the lateral mode becomes dominant for $D > 25$ m.

Under the free-free boundary condition, the fundamental mode exhibits a saddle-like shape, as depicted in Fig. 2.16(c). Notably, the fundamental frequency in the free-free case is significantly higher—about an order of magnitude—than in the batten-supported scenario.

The modal analysis results were fitted to power laws, as shown in Fig. 2.16(a), with RMS errors of 0.014, 0.003, and 0.116 Hz for the lateral, vertical, and saddle modes, respectively. The analytical expressions for the natural frequencies (in Hz) for $F/D = 1.0$ are as follows:

$$\begin{aligned} f_{lateral} &= 217.2 \times D^{-1.699} \\ f_{vertical} &= 88.43 \times D^{-1.419} \\ f_{saddle} &= 738.1 \times D^{-1.357}. \end{aligned} \tag{2.17}$$

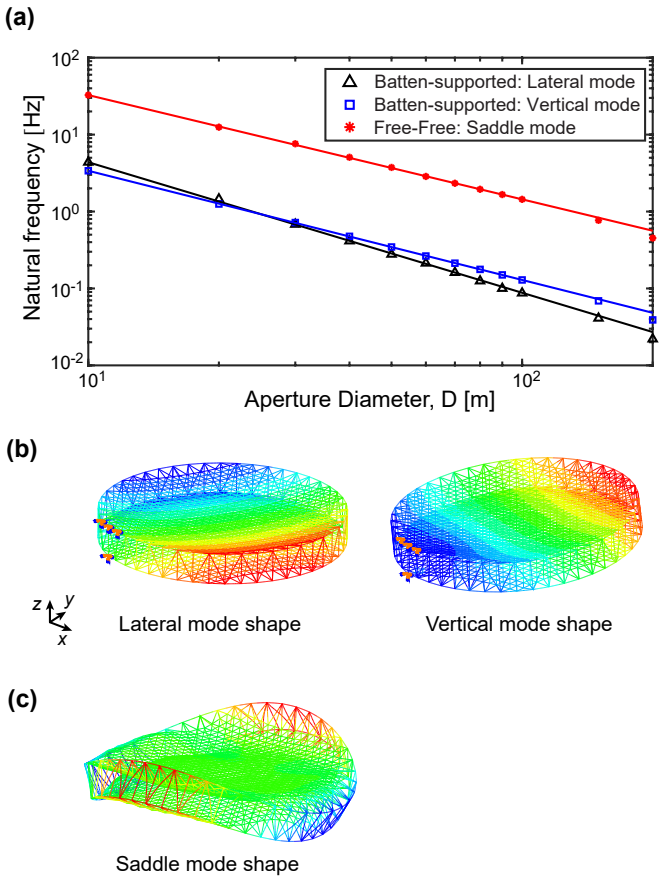

Figure 2.16: Natural frequencies and mode shapes for $F/D = 1.0$: a) frequency trends, b) first two mode shapes for prime-batten support condition, and c) first mode shape for free-free condition.

The prestressed modal analysis for mesh reflectors with $F/D = 0.5$ and $F/D = 0.7$ followed a similar procedure as the one used for $F/D = 1.0$. The corresponding scaling laws for natural frequencies were derived and are presented in Fig. 2.17.

For the batten-supported boundary condition, the first two natural frequencies correspond to the lateral and vertical modes, respectively. Unlike the $F/D = 1.0$ case, the lateral mode is the fundamental mode across all aperture diameters for both $F/D = 0.5$ and $F/D = 0.7$. Under the free-free boundary condition, the fundamental vibration mode is saddle-like, with frequencies significantly higher than those observed under batten-supported conditions.

In log-log space, all natural frequencies form straight lines with negative slopes, indicating a similar power-law relationship as for the case of $F/D = 1.0$ where the natural frequencies decrease as the reflector diameter increases. The results from

the modal analysis have been fitted to power laws as before, and the corresponding analytical expressions for reflectors with $F/D = 0.5$ is as follows:

$$\begin{aligned} f_{lateral} &= 218.1 \times D^{-1.839} \\ f_{vertical} &= 158.3 \times D^{-1.477} \\ f_{saddle} &= 1005 \times D^{-1.407}. \end{aligned} \tag{2.18}$$

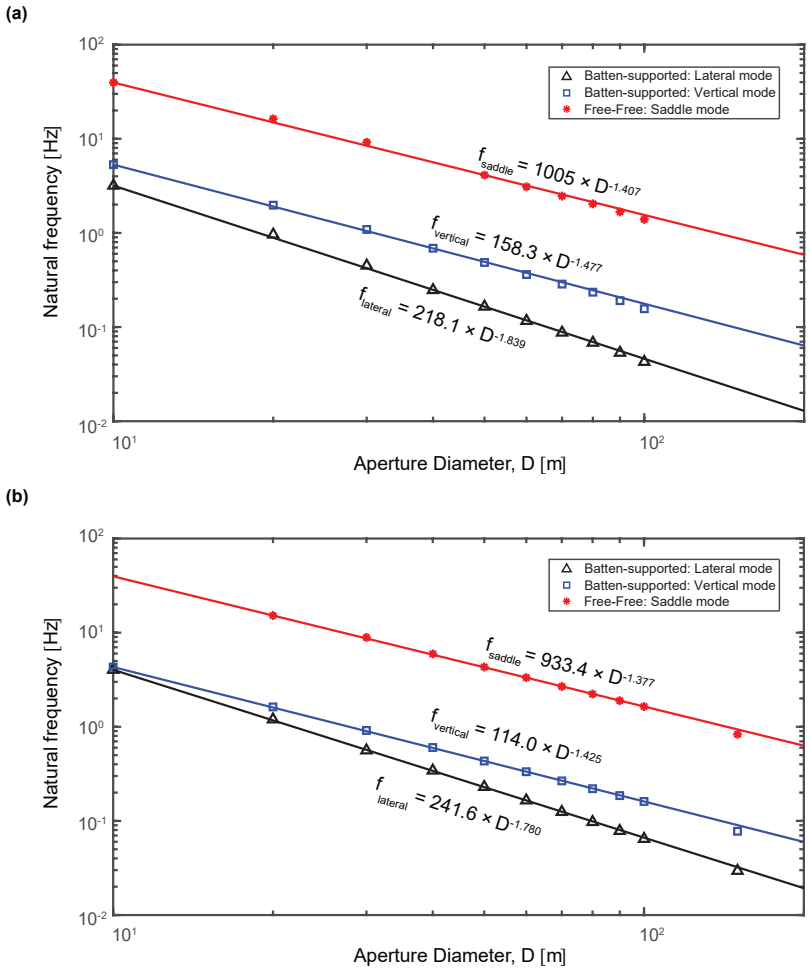

Figure 2.17: Natural frequency trends: a) $F/D = 0.5$, and b) $F/D = 0.7$.

For reflectors with $F/D = 0.7$, the analytical expressions are:

$$\begin{aligned} f_{lateral} &= 241.6 \times D^{-1.780} \\ f_{vertical} &= 114.0 \times D^{-1.425} \\ f_{saddle} &= 933.4 \times D^{-1.377}. \end{aligned} \tag{2.19}$$

2.5.3 Semi-Analytical Models for Fundamental Frequencies

While the high-fidelity modal analysis provides precise estimates of natural frequencies and mode shapes for reflectors of various apertures, the computational

demands become substantial for larger reflectors due to the increasing number of structural elements. For instance, the high-fidelity models for $D = 100$ m and $D = 200$ m contain approximately 15000 and 32000 structural elements, respectively. A semi-analytical model offers a faster yet accurate alternative for estimating these modal parameters.

Figure 2.18 illustrates the semi-analytical approach. The concept is to homogenize the mesh reflector to an edge-stiffened circular elastic plate. The cable nets are modeled by a flat continuum disk with equivalent stiffness, while the perimeter truss is represented as an equivalent hoop attached to the disk's outer edge. This approach can be applied to all mode shapes, though the model details vary. Here, the semi-analytical model for the lateral mode (the lowest frequency mode for larger apertures under batten-supported boundary condition) and the saddle mode are presented.

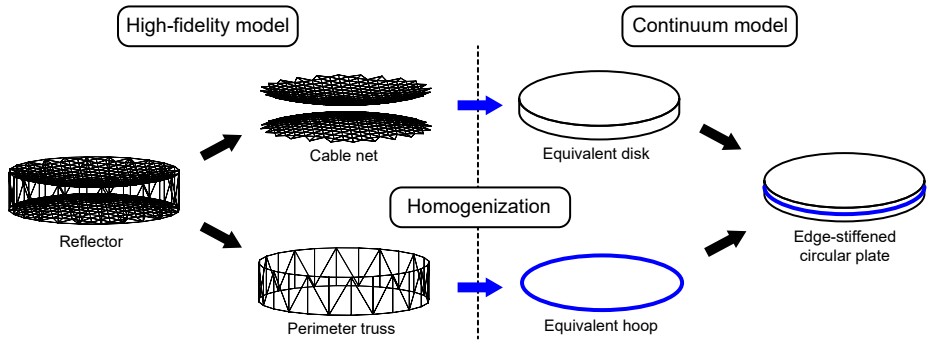

Figure 2.18: Semi-analytical modeling scheme.

For the batten-supported boundary condition, the lateral mode corresponds to an in-plane vibration where the reflector rotates about the three fixed joints in the perimeter truss that are constrained by the prime batten. This mode can be modeled as a 1-DoF mass-spring system, as shown in Fig. 2.19(a), where m_{eq} is the total mass, and I_{eq} is the moment of inertia of the reflector around a horizontal axis through its center of mass. The equivalent torsional stiffness, k_{eq}, of the torsional spring attached to the rigid bar of length $D/2$ is derived from an elastic analysis of the equivalent edge-stiffened continuum disk subjected to the same boundary conditions as the reflector, and loaded by an external couple, as shown. The three supports of the disk represent the constraints imposed by the prime batten on the upper ring of longerons.

Figure 2.19(b) illustrates the homogenization of the front net's stiffness. The rear net is not considered, as the lower ring of longerons is effectively free to rotate. The

truss elements of the front net are assumed to be coplanar, with a uniform tessellation of equilateral triangles, with edge length L. The equivalent homogenized stiffness matrix for a single-layer truss tessellation, A_{SL}, is calculated by superposition of three parallel trusses [4], Fig. 2.19(b), with modulus E_n and cross-sectional area A_n:

$$A_{SL} = \frac{3\sqrt{3}E_n A_n}{4L}. \tag{2.20}$$

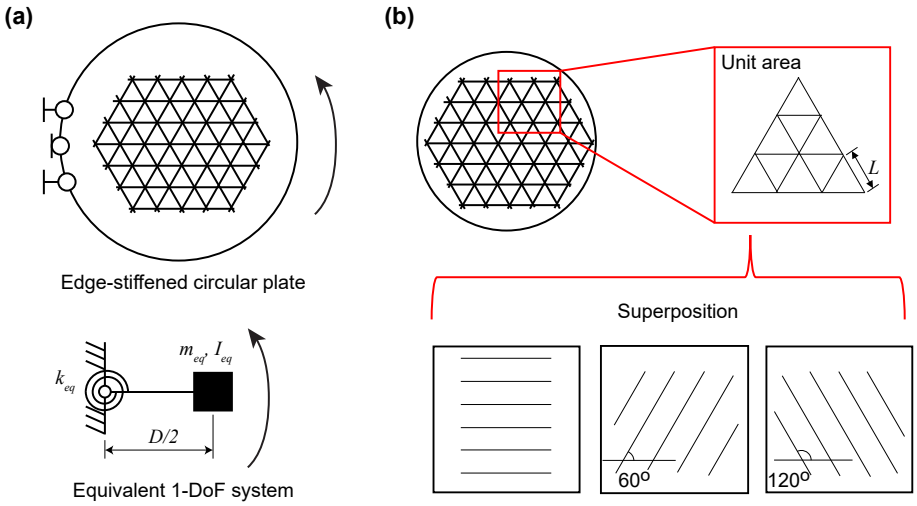

Figure 2.19: Semi-analytical model to estimate lateral mode: a) 1-DoF model, and b) homogenization of the net.

The equivalent continuum Young's modulus, E^*, and Poisson's ratio, ν^*, are (see Appendix A for details):

$$E^* = \frac{2\sqrt{3}E_n A_n}{3t_n L}, \quad \nu^* = \frac{1}{3}. \tag{2.21}$$

To complete the semi-analytical model of the edge-stiffened disk, a circular hoop, representing the longerons positioned along the perimeter of the front net and matching their cross-section, is attached to the disk's edge. As illustrated in Fig. 2.19(a), the equivalent torsional stiffness of the complete model, k_{eq}, is estimated by evaluating the rotation of this model under a given moment. The moment of inertia is the sum of I_{eq} and the parallel axis contribution, and the natural frequency is calculated from this system as follows:

$$f_{lateral} = 2\pi\sqrt{\frac{k_{eq}}{m_{eq}D^2/4 + I_{eq}}}. \tag{2.22}$$

Figure 2.20 compares the natural frequencies computed from the finite element analysis with those obtained from the semi-analytical approach. The results, also presented in Table 2.7, show that the lateral mode frequencies align well with the high-fidelity model, with errors reaching up to 22.27% for the largest diameters. This error is primarily due to differences between the actual cable net stiffness and the homogenized disk model. It is important to note, however, that Eq. 2.22 is applicable for all values of F/D, unlike the high-fidelity approach, which necessitates a separate model (and the associated computational costs) for each variation in F/D.

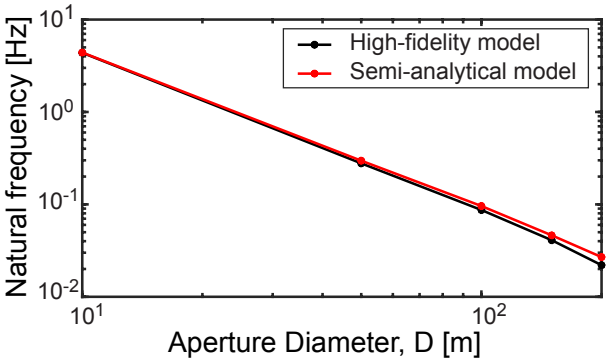

Figure 2.20: Natural frequency corresponding to lateral mode.

Table 2.7: Natural frequency of lateral mode (high-fidelity model vs. semi-analytical model)

	Natural frequency (Hz)		
D(m)	High-fidelity model	Semi-analytical model	Error (%)
10	4.346	4.371	0.58
50	0.276	0.294	6.54
100	0.086	0.095	10.30
150	0.041	0.046	12.39
200	0.022	0.027	22.27

As opposed to the lateral vibration mode, the saddle mode involves an out-of-plane motion under free-free boundary conditions, requiring the bending stiffness of the equivalent model to estimate k_{eq}. The semi-analytical model is therefore modified to estimate the bending stiffness of the prestressed nets and the perimeter truss's contribution. The bending and torsional stiffnesses of the continuum model are calculated by multiplying the in-plane continuum stiffness of each net by the square of the local distance between the nets [4].

This model can be further refined by accounting for the fact that the x, y plane projections of the triangles connecting the inner net to the perimeter truss are not equilateral. The in-plane stiffness of the central hexagonal region, composed of identical equilateral triangles, remains A_{SL} as before. The area between the perimeter truss and the central hexagon features a coarser cable pattern, as illustrated in Fig. 2.21(a). The equivalent material properties of the disk were derived by considering these distinct cable patterns, allowing for differences in angles and distances between the cables in the boundary region. The angle between the cables, β, is expressed as:

$$\beta = \tan^{-1}\left(\frac{L}{g}\right) = \tan^{-1}\left(\frac{4\left(2+\sqrt{3}\right)L}{D}\right). \tag{2.23}$$

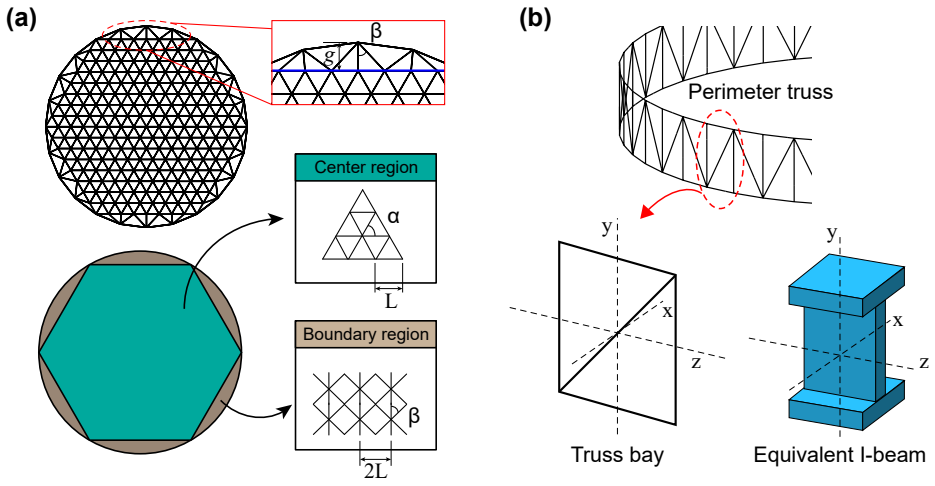

Figure 2.21: Semi-analytical model for free-free saddle mode: homogenization of a) net, and b) perimeter truss.

The ABD stiffness matrix for the equivalent disk was then obtained following the derivation for double-layer space frames outlined in [4]. Since the front and rear nets are identical, $A \approx 2A_{SL}$ and $D \approx A_{SL}(2z)^2$, where z is the distance between the two nets. Substituting Eq. 2.1 and using $r^2 = x^2 + y^2$, the ABD matrix at a radial distance r from the axis of the paraboloid is expressed as:

$$ABD\,(r) = \begin{bmatrix} A & B \\ B^T & D\,(r) \end{bmatrix} = \begin{bmatrix} 2A_{SL} & 0 \\ 0 & \left(2s_0 + \frac{r^2}{2F}\right) A_{SL} \end{bmatrix} \tag{2.24}$$

where the B matrix is zero, for symmetry.

The perimeter truss consists of identical bays, as shown in Fig. 2.21(b). In the proposed semi-analytical model for the saddle vibration mode, the perimeter truss was homogenized to an equivalent I-beam, having the same second moment of area as a bay for all axes. This equivalent hoop was again attached to the edge of the equivalent disk, and a modal analysis was performed on the continuum model using ABAQUS/CAE 2017.

Figure 2.22(a) compares the saddle mode frequencies obtained from the high-fidelity simulations with those from the semi-analytical model. The mode shape produced by the semi-analytical approach shows good qualitative agreement, as illustrated in Fig. 2.22(b), and the corresponding numerical values are provided in Table 2.8.

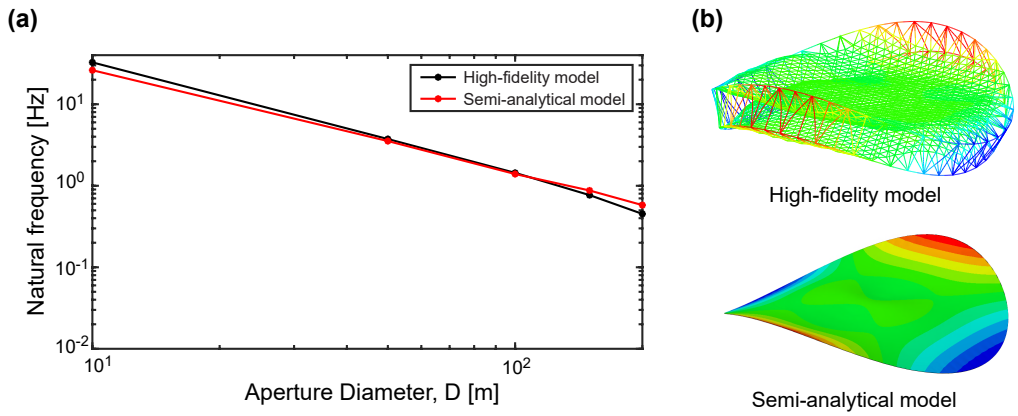

Figure 2.22: Natural frequency of free-free saddle mode: a) frequency comparison, and b) mode shape comparison.

Table 2.8: Natural frequency of saddle mode (high-fidelity model vs. semi-analytical model)

	Natural frequency (Hz)		
D(m)	High-fidelity model	Semi-analytical model	Error (%)
10	32.473	26.153	19.85
50	3.702	3.535	5.56
100	1.430	1.393	3.26
150	0.764	0.875	13.93
200	0.452	0.579	28.10

2.6 Chapter Conclusions

This chapter has presented the design and analysis of deployable mesh reflectors, spanning aperture sizes from 10 to 200 meters. The reflector geometry is tailored to

meet the stringent surface accuracy requirement of 0.6 mm, necessary for operation at a 10 GHz RF frequency. Through a comprehensive investigation of the reflector's kinematic and static properties, it was determined that a design composed entirely of triangular facets—without cross-wires—ensures both kinematic and static determinacy. This approach guarantees a unique shape and unique equilibrium solution under prestress. The prestress distribution across the structural elements is optimized by adjusting the tension tie forces applied to the net. Across all aperture sizes, the optimized designs exhibit a lower standard deviation in cable tension and reduced compressive forces on the perimeter truss compared to non-optimized designs.

The structural design methodology has been detailed, with mass and volume analyzed at the component level. For optimized designs, the areal density remains nearly constant as the reflector diameter increases, while non-optimized designs display a rising areal density with increasing size. Scaling laws for mass and volume are derived as functions of aperture diameter. The study concludes that the designed reflectors are feasible for launch with diameters up to approximately 70-100 meters using commercially available launch vehicles. More importantly, the findings emphasize that stowed volume, rather than mass, poses the primary constraint on the launch envelope, underscoring the necessity for innovative design approaches for ultra-large space structures.

Additionally, the natural frequencies of the reflector have been examined under two boundary conditions: batten-supported and free-free. Scaling laws for the fundamental frequencies are proposed based on high-fidelity simulations. A semi-analytical model has been developed for both boundary conditions, utilizing a homogenization technique that approximates the net and perimeter truss as equivalent continua. The semi-analytical model's predictions closely align with high-fidelity simulations while offering a substantial reduction in computational time (from about 48 hours to just a few minutes), with its validity extending to all F/D ratios.

This study has achieved its overall aim of providing practical insights into the design and scaling of deployable mesh reflectors, evaluating existing design approaches, and advancing the understanding of key metrics for assessing these structures for future applications. Moreover, this study has extended key metric data beyond the 25 m aperture presented in previous studies, thereby establishing a baseline for comparing large deployable mesh reflectors with ISA concepts, as discussed in Chapter 3.

Chapter 3

ISA CONCEPT FOR RING-LIKE STRUCTURES

This chapter incorporates work that has been published in the following proceedings:

J. Suh, S. P. Dassanayake, M. Thomson, and S. Pellegrino, "Scalable Concept for Reflector Antenna Assembled in Space," in *AIAA SCITECH 2024 Forum*, 2024, p. 0823. DOI: 10.2514/6.2024-0823.

J. Suh, S. P. Dassanayake, M. Thomson, and S. Pellegrino, "In-Space Assembly of Large Mesh Reflector Antennas," in *Aerospace Structures, Structural Dynamics, and Materials Conference, SSDM 2024 [Technical Presentation]*, 2024, p. 137 740.

J. Suh, S. Dassanayake, M. Thomson, and S. Pellegrino, "Concept for In-Space Assembly of Large Reflector Antennas," in *41st ESA Antenna Workshop ESTEC*, 2023.

3.1 Motivation

As discussed in Chapter 2, large deployable reflectors present several challenges, including constraints imposed by the size of launch vehicles, the risks associated with folding and unfolding delicate components, and the difficulty in maintaining surface accuracy under these conditions. While deployable reflector systems have proven very effective for current missions, they will struggle to deliver the structural integrity and precision required for apertures spanning hundreds of meters. These limitations have driven studies of ISA, which enables the construction of large reflectors directly in orbit. This method not only offers the possibility of removing the restrictions of launch vehicle dimensions but also mitigates the risks of deployment mechanisms. Additionally, ISA provides the flexibility to build and assemble complex structures with enhanced surface accuracy and improved resilience to in-orbit conditions.

The increasing demand for larger and more precise space structures, which surpass the physical and technical limitations of traditional deployable systems, has therefore heightened the need to develop ISA concepts for reflectors. As space missions require higher-resolution imaging, improved communication capabilities, and more advanced scientific instruments, the necessary aperture sizes for reflectors have grown substantially. ISA leverages advances in robotic technologies and on-orbit servicing, allowing for the construction, maintenance, and potential upgrades of space-based reflectors. This approach not only extends mission lifespans but also facilitates the deployment of structures that are too large or complex to be pre-assembled and launched from Earth. By enabling the ISA of ultra-large reflectors, new opportunities are unlocked for next-generation space missions, such as deep-space exploration and advanced communication systems, where the size and precision of reflectors are crucial to mission success.

In this chapter, an ISA concept is proposed for mesh reflectors and similar ring-like structures with a cable-based interior. The reflector design closely follows that of the deployable AstroMesh, but with a key distinction: the concept shifts from deployment to ISA. By transitioning to an in-space approach, the constraints tied to launching fully stowed configurations are bypassed. First, the mass and stowed volume of the ISA reflectors are calculated for apertures reaching up to 200 meters, utilizing the generalized design methodology developed in Chapter 2. This step is crucial for evaluating the launch feasibility of the proposed reflector within current vehicle limits. The analysis not only takes into account the physical dimensions of

the reflector but also assesses how these factors influence the viability of launching the components for ISA. Next, a detailed assembly scheme is introduced, focusing on the practical implementation of the concept. Central to this process is the use of a robotic system capable of autonomously constructing the large reflector in space. The centralized robotic system would handle the sequential assembly of the reflector's components, allowing for precise alignment and tensioning of the cables and facets to achieve the required surface accuracy. This method provides flexibility in scaling up the structure, enabling the creation of reflectors far larger than what could traditionally be deployed from Earth. The proposed approach offers a solution for building highly accurate, large-aperture reflectors, making it an ideal strategy for future space missions requiring enhanced performance and larger structural footprints.

3.2 Scaling of Mass and Stowed Volume for ISA Reflectors

ISA reflectors are designed with the same structural architecture as the deployable reflectors discussed in Chapter 2, featuring two cable nets and a perimeter truss. The same dimensions and material properties are assumed. However, all components are assumed to be modularly designed and stored separately as described next.

Both the front and rear cable nets, along with tension ties and metallic mesh, are fabricated and pre-assembled, then simply estimated to be compacted to one-twentieth of their original volume for stowage. The perimeter truss struts are assumed to be manufactured by cutting deployable omega beams, which are flattened and coiled onto a mandrel for compact storage. The strut spool dimensions are estimated as follows (see Fig. 3.1): the height of the core mandrel, H_{core} matches the flattened width of the strut, while the core diameter, D_{core} is set equal to the core height. As the flattened strut is coiled around the mandrel, the spool diameter increases, with the maximum diameter, D_{spool} limited to four times the core diameter. The spool height, H_{spool} remains the same as the core height. The total number of strut spools required is calculated based on the total length of the struts. The volume of the joint stack is determined based on its envelope. Once the total volume of the truss components is calculated based on these assumptions, the overall diameter and height are determined by assuming the components are packed compactly within a cylindrical envelope, where the height is twice the diameter, i.e., $H_{stowed} = 2D_{stowed}$.

The mass of the ISA reflectors can be readily calculated following the approach

introduced in Sections 2.3 and 2.4, and accounting for the lack of deployment actuators in Eq. 2.10.

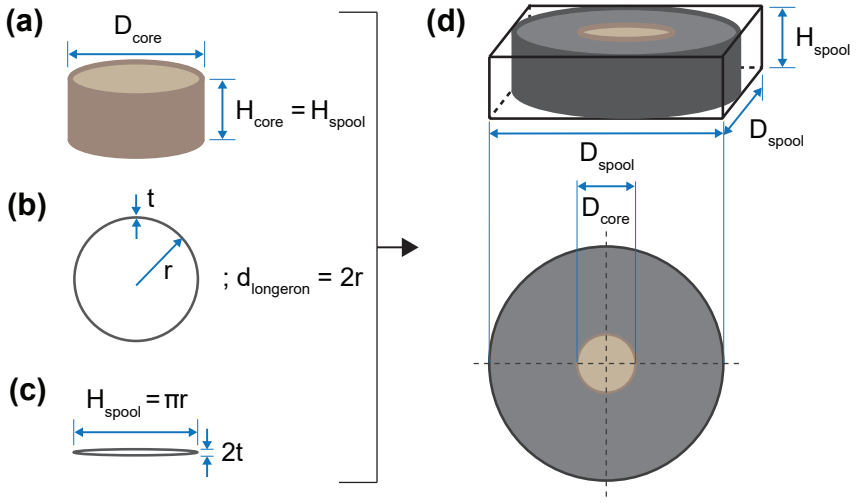

Figure 3.1: Coiled strut volume estimation: a) core mandrel, b) cross section of the strut, c) flattened strut, and d) strut spool.

Figure 3.2 shows the overall mass, stowed diameter, and height of the ISA reflector for an F/D ratio of 1.0 across a diameter range from 10 m to 200 m. The black dots represent the data points for deployable reflectors, while the red dots denote the data points for ISA reflectors. The pink and blue solid lines indicate the payload capacity limits for Falcon Heavy and Starship launchers, respectively, as previously discussed.

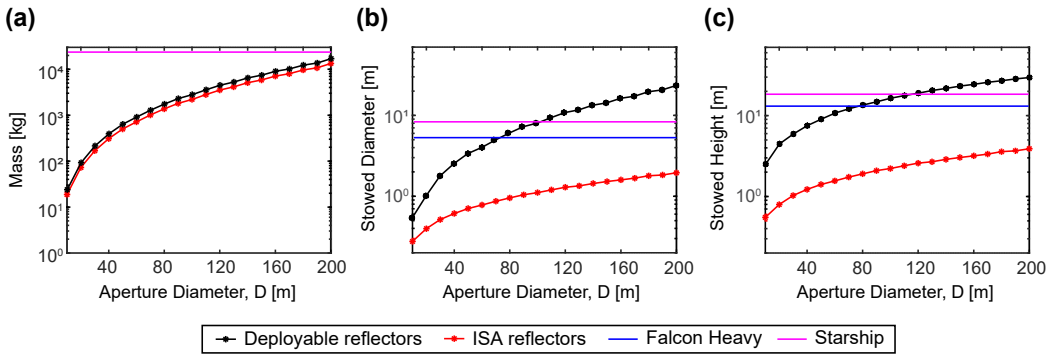

Figure 3.2: Scaling of ISA vs. deployable reflectors for $F/D = 1.0$: a) total mass, b) stowed diameter, and c) stowed height.

The total mass and stowed volume of the ISA reflectors were found to scale approximately quadratically with diameter. For deployable reflectors, the mass was not the primary constraint. However, as expected, ISA reflectors are lighter than their

deployable counterparts across all relevant aperture sizes. Volume, on the other hand, posed a constraint for deployable reflectors. In contrast, the stowed diameter and height of ISA reflector components fit comfortably within the fairing's limits, even for diameters up to 200 m. As a result, a single launch can accommodate an ISA reflector with a diameter exceeding 200 m, demonstrating remarkable potential.

3.3 In-Space Assembly Concept

3.3.1 General Overview

A linear in-space assembled truss concept has been proposed [9], where a three-dimensional truss is constructed as follows: three *SpiderFab* "Trusselator" heads extrude continuous 1st-order trusses to serve as longerons, while a fourth robotic head with 6 DoF fabricates and attaches cross-members and tension lines, creating a truss support structure with a 2nd-order hierarchy. As the structure extends, it simultaneously tensions and deploys a pre-built z-folded solar array blanket, as depicted in Fig. 3.3(a).

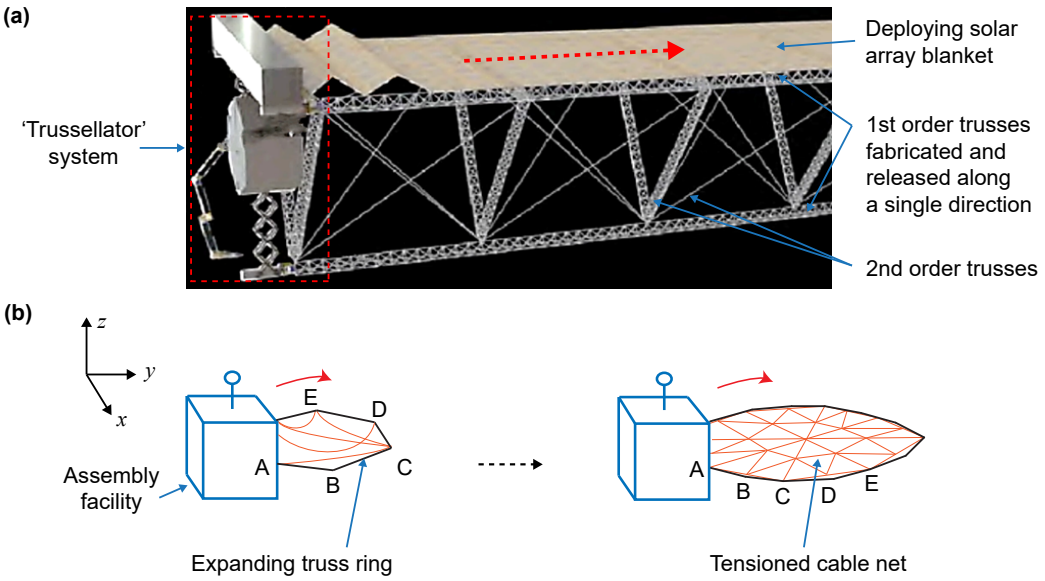

Figure 3.3: ISA concepts: (a) linear ISA trusses [9], and (b) proposed two-dimensional ISA for ring-like structures with a cable interior.

A defining characteristic of the mesh reflector architecture we are focusing on is its prismatic, ring-like perimeter truss. This allows for a similar, but two-dimensional, assembly concept compared to the Trusselator approach. In this concept (see Fig. 3.3(b)), a truss ring is constructed and extended from an assembly facility, gradually expanding as additional components are added. The cable interior,

initially slack, becomes tensioned during the deployment process, ensuring that the required structural stiffness and precision are achieved upon completion.

The core principle of the ISA concept thus developed for mesh reflectors is to design reflector components as modular units, or "Lego bricks," allowing them to be efficiently stored and transported within a specialized assembly facility, known as the *Truss Builder*. This facility, shown in Fig. 3.4, serves as the central hub for the entire construction process once the components reach their target orbit.

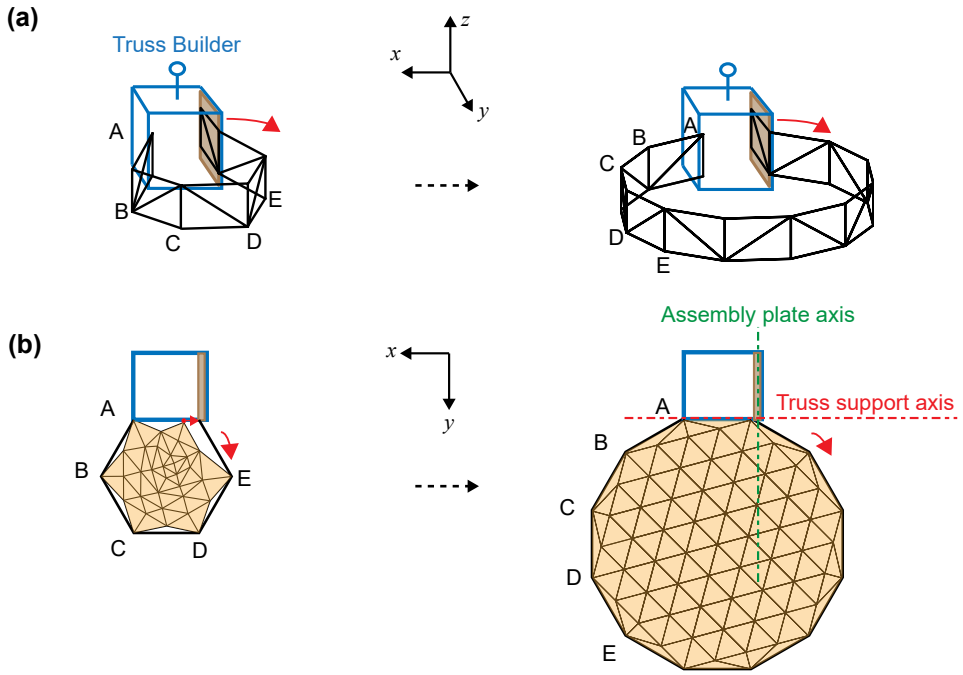

Figure 3.4: Schematic drawing of in-space polygonal ring assembly with cable interior: (a) truss assembly, and (b) cable net deployment.

The assembly process is highly streamlined and relies on simple, repetitive operations. Upon arriving in orbit, the truss builder begins assembling the structure by constructing a single bay of the perimeter truss. After each bay is completed, the corresponding node of the pre-folded cable net is connected to it (Fig. 3.4(b)) prior to bay release. The sequence is repeated—constructing and releasing each bay one at a time—until the entire reflector is fully assembled. The process is complete when the final bay is released from the truss builder, resulting in a fully deployed reflector.

The significance of this concept lies in the use of a single, stationary robot—the truss builder—for the autonomous assembly of large, polygonal, ring-like structures with a cable interior. By utilizing a stationary robot that remains in place throughout

the construction, the planning complexity of the assembly process can be significantly reduced. This design eliminates the need for multiple mobile robots, long challenging traverses or complex coordination between moving parts, which would otherwise increase the risk of failure and add to the overall system cost. Moreover, the modular nature of the components and the repetitive nature of the assembly process make this method highly scalable. The same approach can be applied to reflectors of various sizes, from small-scale to ultra-large structures, without significant changes to the assembly strategy.

3.3.2 Operations of the Truss Builder

In the proposed assembly scheme, the truss builder, along with all structural components (i.e., struts, joints, and the cable net), is folded and stowed during launch. On reaching the target orbit, the truss builder is deployed, making the reflector ready for assembly. The proposed truss builder is equipped with a metrology system for precise shape accuracy and vibration measurements. It also features multiple robotic subsystems designed to facilitate the construction and release of each bay of the perimeter truss, a central element of this assembly concept. The assembly plate, crucial to the process, serves as the platform where each bay is constructed. It is designed to slide in and out of the truss builder to release the completed bays, increasing the diameter of the ring-like structure. Joint and strut dispensers are located behind the assembly plate, holding the modules required for bay assembly. A gantry robot, acting as the *Manipulator* with three translational and one rotational DoF, is responsible for picking up and connecting the structural components. During the assembly, two truss supports, labeled S_1 and S_2, hold the ends of the perimeter truss. The edge of the truss builder in between serves as the bay that completes the truss ring. The folded cable net, stowed along this truss support axis (see Fig. 3.4(b)), has its net joints $C_{edge,i}$ secured by net attachment devices. As each bay is constructed, the slack net nodes $C_{edge,i}$ are attached to the corresponding truss nodes N_i. As the cables tighten, the interior net nodes C_j adjust accordingly. The reflective surface (i.e., the metallic mesh), is pre-attached to the front net and folded together with it. Consequently, the antenna assembly is completed once the truss builder releases the final bay and secures the net.

Figure 3.5 shows a two-dimensional view of the steps involved in the proposed assembly operation. As described, the truss bays B_i are sequentially assembled and released outward from the truss builder. Key components include the sliding assembly plate, the manipulator, and the net attachment device.

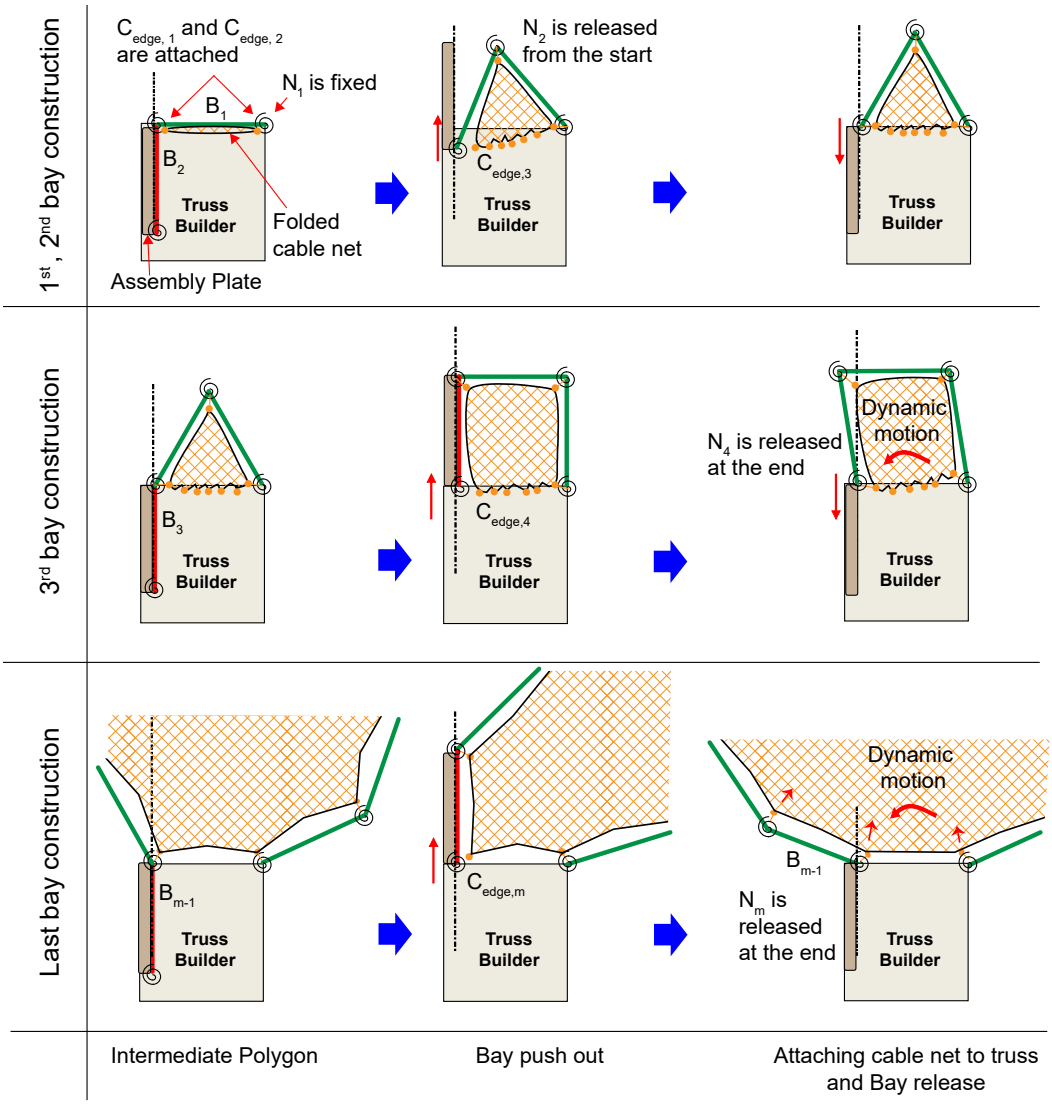

Figure 3.5: Two-dimensional view of truss assembly process: first, second, third, and final bay assembly.

At the start, two pre-built bays, B_1 on the outer wall and B_2 on the assembly plate, are connected to the truss builder, with their truss nodes N_1 and N_2 attached to the corresponding net nodes $C_{edge,1}$ and $C_{edge,2}$. The process begins with the assembly plate pushing out the pre-built bay B_2, after which the net attachment device connects net node $C_{edge,3}$ to the truss joint N_3, and the assembly plate retracts, deploying B_2. The remaining bays are similarly constructed. The manipulator picks up the joints and struts from storage, assembling each bay on the plate (indicated by red lines in Fig. 3.5), and the net attachment device connects the net nodes to the truss (indicated by orange dots in Fig. 3.5). Once a bay is completed, the assembly

plate pushes it out (released bays are indicated by green lines in Fig. 3.5) and retracts to prepare for the next bay. This process continues until all bays are assembled, with the push-out of the final bay, B_{m-1} (where m represents the number of sides in the final polygonal ring), and the application of a state of prestress to the fully assembled reflector. To ensure the structural stability of the partially complete structure during assembly, the joints are designed to be elastically deformable in torsion, with angle stops that maintain a polygonal shape for the released bays.

3.4 Chapter Conclusions

This chapter has introduced a novel scheme for robotically assembling large reflectors, based on the AstroMesh reflector architecture. The approach to the structural design of the reflector has been described, including the determination of mass and stowed volume for apertures up to 200 meters in diameter. The findings highlight the significant advantages of ISA reflectors over traditional deployable designs, particularly in terms of reducing the required launch envelope.

The proposed ISA scheme utilizes a centralized truss builder facility, launched into orbit with all necessary structural components and a simple robotic system. The truss builder automates the reflector assembly through a sequence of simple operations: constructing a bay of the perimeter truss, attaching the corresponding outer node of the cable net to the bay, and then pushing the completed bay out of the truss builder. The chapter outlines and discusses the detailed operations of the assembly facility for bay construction and release.

The flexibility of the proposed ISA concept is crucial for future space missions, which will require large reflectors for their applications in high-resolution imaging, advanced communications, and scientific observations. By simplifying the assembly process and enabling the construction of high-precision reflectors directly in space, the truss builder represents a significant advancement. This method offers a practical and scalable solution for building large, complex structures that would be challenging or infeasible with conventional deployable systems.

Chapter 4

SIMULATION OF ISA CONCEPT

This chapter includes both published work from the following proceedings and new, unpublished sections:

J. Suh, S. P. Dassanayake, and S. Pellegrino, "In-Space Assembly of Large Mesh Reflectors," in *AIAA SCITECH 2025 Forum [Accepted]*, 2025.

J. Suh, S. P. Dassanayake, M. Thomson, and S. Pellegrino, "In-Space Assembly of Large Mesh Reflector Antennas," in *Aerospace Structures, Structural Dynamics, and Materials Conference, SSDM 2024 [Technical Presentation]*, 2024, p. 137 740.

4.1 Motivation

ISA poses significant challenges, particularly as the number of structural components increases and different assumptions about the assembly sequence come into play. As outlined in Section 1.4, a critical issue is ensuring that the assembly process proceeds smoothly, avoiding potential snags, jams, or misalignments that can occur when components interact unexpectedly. The complexity increases with larger structures, making it difficult to predict how different parts will behave during assembly. As the structure grows, the risk of interference between components rises, leading to potential delays or complications that may hinder the overall process.

Another challenge lies in the order of assembly, which directly affects both the ease of construction and the structural integrity of the final design. A poorly planned sequence can introduce unnecessary stresses or misalignments. This necessitates careful planning, with each step of the assembly process thoroughly considered to maintain stability and functionality as new components are integrated.

To manage these issues effectively, advanced numerical simulations become essential, accurately modeling the entire assembly process and tracking the evolution of the structure as it grows. This not only helps predict how components will interact but also allows for optimization of the assembly sequence to avoid potential issues such as interference or instability. As space missions demand larger and more complex structures, robust simulation tools will be key to developing reliable ISA concepts, ensuring that structures are built efficiently and remain stable throughout their assembly and during operation in orbit.

In this work, a two-dimensional finite element model is introduced to predict the kinematics of large polygonal ring-like structures with a cable interior during the assembly process by a single stationary robot. This model is based on the ISA concept presented in Chapter 3 and is developed using commercial finite element software. The focus of this chapter is on the numerical model setup and the novel simulation techniques designed to capture the complexities of sequential assembly for large-scale structures.

The example structure used in this study consists of six bays, providing a practical scenario to refine the simulation technique and gain an accurate understanding of the evolving assembly process. This example aids in evaluating the structural behavior during each phase of the assembly, including the tensioning of the cables and the formation of the polygonal perimeter truss. Along with simulating the kinematics of the assembly, the study focuses on identifying and modeling critical design

considerations for the stationary robot. These considerations, aimed at optimizing the robot's performance to ensure a robust and efficient assembly process, are further explored in Chapter 5.

4.2 Numerical Simulation Setup

The proposed assembly concept involves sequentially constructing and releasing each truss bay, leading to intermediate configurations that are challenging to predict analytically. As each truss bay is pushed out perpendicular to the truss support axis, it rotates upon release due to elastic reactions in the joints, as shown in the third column of Fig. 3.5. This rotation causes vibrations with each released bay, potentially impacting the structural stability during the assembly process. Additionally, the simulation must handle tensioned cables throughout the process. These cables, critical for preserving the truss's structural integrity and final shape, exert forces that may induce oscillations and interfere with the assembly as they are secured to the truss joints. Disruptions can also arise from the locking of truss joints during assembly. This can lead to misalignments or increased stress in the structure, which may compromise the overall functionality.

In addition, achieving the desired final configuration of the structure is of utmost importance, as any deviations could affect the precision and functionality of the reflector. Lastly, adequate prestressing of the structure at the conclusion of the assembly process is critical, as it ensures that the truss remains rigid and stable under operational conditions. Without sufficient prestress, the structure may experience deformation or instability, undermining its performance.

Accurately predicting these dynamic responses is crucial to ensuring the overall reliability and precision of the assembly process, particularly in space, where even small deviations can compromise the structure's operational performance.

Given the prismatic geometry of the structure (see Fig. 2.1), the assembly process can be effectively modeled in two dimensions, as shown in Fig. 4.1. This two-dimensional model focuses solely on the truss elements forming a single perimeter ring of the polygonal truss in the horizontal plane (i.e., longerons) and is supported at one bay, incorporating a single integrated cable net. The forces exerted by the reflective metallic mesh on the cable net are not included in the model.

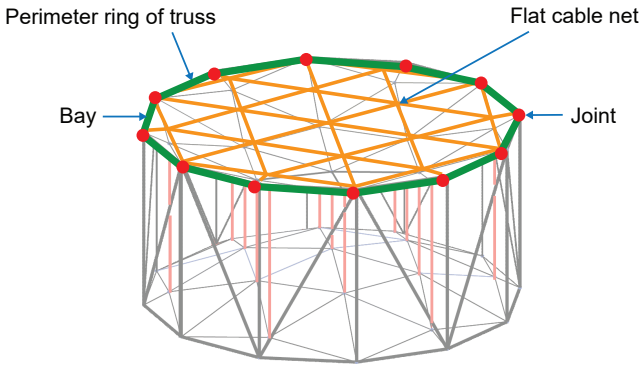

Figure 4.1: Simulation approach: perimeter ring and a single cable net.

4.2.1 Model Definition

This simulation aims to investigate the kinematics of polygonal ring-like structures with a cable interior, during assembly. Starting from the initial configuration of the truss supports which represent the truss builder, the assembly process sequentially adds each bay to the structure. As each bay is incorporated, cables are systematically attached to the corresponding truss nodes and tensioned, ensuring the structure maintains its geometric configuration and contributing to the truss' overall stiffness. The truss supports ensure precise positioning and securing of each bay, allowing the assembly to progress smoothly and ensuring that the final structure meets its intended shape and functionality.

A geometrically nonlinear finite element analysis was performed using ABAQUS/CAE 2020. The finite element model was established by modeling each perimeter truss bay as a two-dimensional rod, with a length matching the longeron of the lab-scale prototype (L_B = 0.3264 m) described in Chapter 6, and discretized into 10 two-node beam elements (B33). The joints between adjacent bays were modeled as pinned connections with Multi-Point Constraints (MPCs), allowing relative rotational DoF. Torsional stiffness at the joints was provided by defining ROTATION connector elements (see Fig. 4.2(b)), with the stiffness value set at k = 0.018 Nm/rad. Angular velocity-proportional damping (c = 50 Nms/rad) was applied at the joints, and joint masses were modeled as equivalent point masses at the corresponding truss nodes (N_i). The cross-sectional dimensions were selected to ensure that the stiffness of each bay was preserved. The following material properties for the bays were defined: high-modulus CFRP with E_{CFRP} = 325.4 GPa, Poisson's ratio ν = 0.3, and density ρ_{CFRP} = 1786 kg/m^3, similar to the structural design outlined in Section 2.3. Since all perimeter truss joints have identical rotational

stiffness, and the two end joints at the truss builder (N_1 and N_{12}) are disconnected in the final configuration (see Fig. 4.2(a)), short rods (b_1, b_2) of 10% the bay length, with the same material, cross-section, and mesh characteristics, were modeled at the ends. These short rods enable the definition of rotational springs at the joints between b_1-B_1 and b_2-B_{11}, but do not influence the kinematics of the structure during assembly.

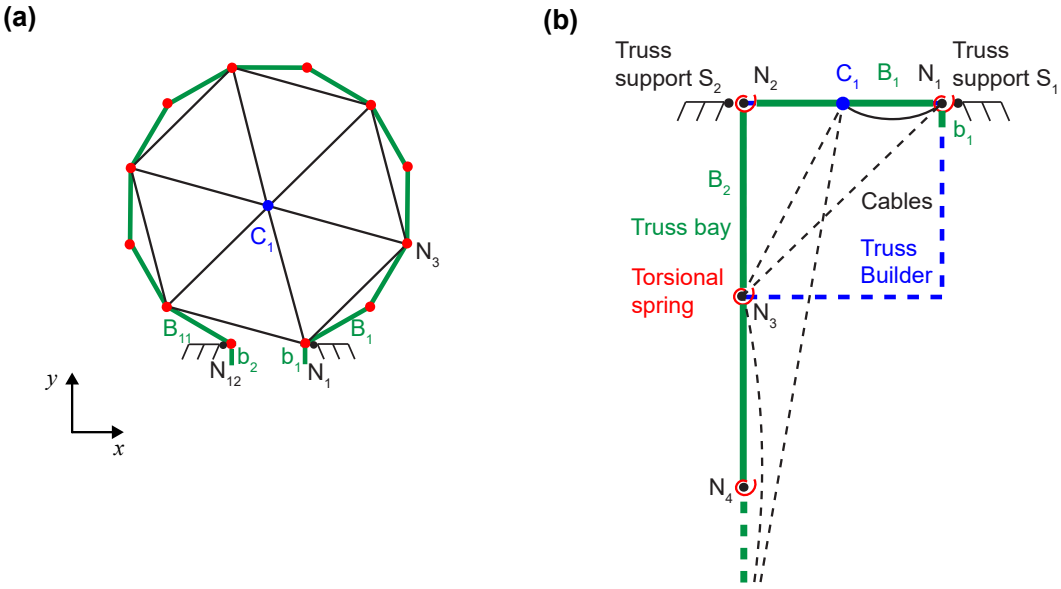

Figure 4.2: Finite element model definition for a) an example polygonal ring geometry, and b) corresponding initial configuration where rods and cables are modeled with their final connectivity.

4.2.2 Modeling the Cable Net

The two-dimensional cable net obtained by flattening the three-dimensional cable net does not not yield a unique equilibrium solution, which is essential for the design. To ensure that the structure is adequately prestressed and achieves its functional configuration, all truss members must be in compression, and all cable net elements must be in tension.

The cable net configuration was simplified as follows: consider a linear combination of the N_e equilibrium solutions $[F_c]_j$ that exist for a simplified two-dimensional cable net configuration. The coefficients a_j are optimized to minimize the average cable force $F_{c,\,avg}$, using MATLAB's *fmincon* function, while ensuring that all N_c cable net elements remain in tension and exceed a specified minimum force $F_{c,\,min}$. If real and bounded coefficients a_j are found, the desired prestress state exists for this simplified cable net configuration, and it is used in the model.

The mathematical formulation of this linear program is:

$$\left[\sum_{j=1}^{N_e} a_j [F_c]_j\right]_i = F_{c,\,i} > F_{c,\,min} \text{ for all } i \tag{4.1a}$$

$$a_{lower} < a_j < a_{upper} \tag{4.1b}$$

$$F_{c,\,avg} = \frac{\left(\sum_{i=1}^{N_c} F_{c,\,i}\right)}{N_c}. \tag{4.1c}$$

For this study, the linear programming coefficients a_j were assigned lower and upper bounds of [-500, 500] to ensure sufficient flexibility, and $F_{c,\,min}$ was set to 0.01 N. Figure 4.3(a) shows the adopted cable net configuration for the six-sided structure, featuring a prestress state in which all cables are under tension as desired, and all bays are under compression. In evaluating the self-stress states of the twelve-sided structure, the cable net simplification in Fig.4.3(b) led to slack cables, while the simplification in Fig.4.3(c) achieved the desired prestress distribution.

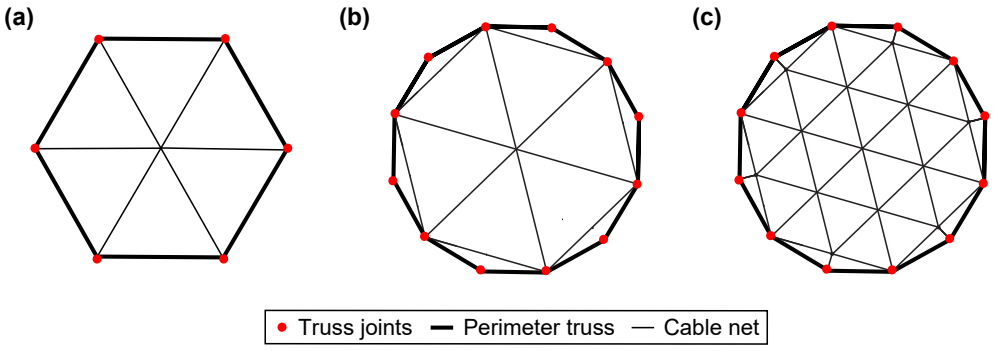

Figure 4.3: Simplification of cable net: (a) six-sided structure, and twelve-sided structure: (b) simplification-1, and (c) simplification-2.

Each cable is modeled using an AXIAL connector element with a specified nonlinear penalty function for stiffness, represented by the blue solid line in Fig. 4.4 and described by:

$$F_c = \frac{F_{c,\,max}}{1 + e^{-[c(u-u_0)]}}; c = 8000, u_0 = 0.5u_{lim}, F_{c,\,max} = 2000 \text{ N}. \tag{4.2}$$

This behavior reflects the properties of a high-modulus CFRP cable element (E_{CFRP} = 325.4 GPa) with a cross-sectional area of 6 mm x 150 μm, as specified in Section 2.3.1, under maximum tensile load, $F_{c,\,max}$. The unstressed reference length $l_{ref,\,ij}$ for each cable element ij is set to match the final flat configuration, i.e., at

the end of assembly, $u \approx 0$ and the cables experience minimal forces. In ABAQUS, the material stiffness is defined to maintain constant y-values beyond user-specified x-value limits. Hence the cable axial force, F_c, is defined to increase smoothly to $F_{c,\,max}$ at the limiting extension u_{lim}, approaching a strain of approximately 0.7%. The extension u_0 defines the midpoint of F_c's transition from zero to $F_{c,\,max}$.

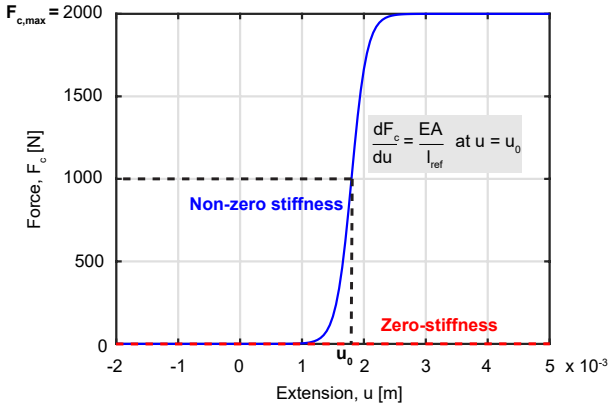

Figure 4.4: Specified nonlinear penalty function for cable stiffness in the finite element model.

The implicit direct-integration method used in ABAQUS/Standard is the Hilber-Hughes-Taylor (HHT) operator, an extension of the trapezoidal rule that solves dynamic equilibrium equations iteratively via Newton's method. Artificial damping is controlled by a numerical parameter, α, which influences the damping effect depending on the time increment and mode's oscillation period. The analysis described here focuses on two-dimensional motion using this Dynamic, Implicit integrator with maximum damping ($\alpha = -0.33$), providing up to 6% damping when the time increment is 40% of the oscillation period of the mode. Additionally, in the simulation, point masses are assigned at the intersecting nodes C_j, applying mass-proportional damping to account for material damping effects throughout the model.

It is important to note that the damping parameters in this simulation are selected primarily to ensure that the simulation steps can progress smoothly, rather than to achieve a specific damping ratio for the structure. The choice of damping is more focused on facilitating numerical stability and convergence during the analysis, rather than accurately reflecting physical damping characteristics of the actual system.

4.2.3 Simulation Steps

ABAQUS does not permit adding constraints or connector elements after the initial model setup, posing a challenge for simulating the sequential addition of

truss bays and the attachment of cable net nodes to truss joints, both essential for modeling the step-by-step assembly process. To overcome this, a simulation approach was developed where all truss bays were initially modeled as a series of connected rods with springs. Displacement and rotation boundary conditions were applied to simulate the 'push-out' and 'release' of each bay. A similar approach was utilized for attaching the cable net nodes. Initially, all cables were modeled with zero stiffness (represented by the red dashed line in Fig. 4.4) to prevent large fictitious extensions from imposing excessive forces on the structure. This initial modeling accounted for the significant extensions that occur when the cables are connected to the truss joints at the start of assembly, instead of connecting them just before pushing out the corresponding bay. These cables, shown by black dashed lines in Fig.4.2(b), are required to stretch by larger amounts. As the truss joints connected to the cables are pushed out, the cable stiffness is modified to its intended value (represented by the blue solid line in Fig. 4.4), effectively *activating* the cable and allowing it to become a part of and exert forces on the structure. Active cables are indicated by black solid lines in Fig. 4.2(b). Note that this approach fundamentally differs from the physical process, as it simulates a change in cable stiffness rather than the physical attachment of slack cables (see Appendix B for details).

The simulation sequence involved repeating bay translation, activating or modifying cable stiffness, and releasing the translated bay to simulate the 'bay push-out,' 'cable attachment,' and 'intermediate polygonal truss formation,' as shown in Fig. 4.5. The bays were pushed out at a speed of 10 mm/s.

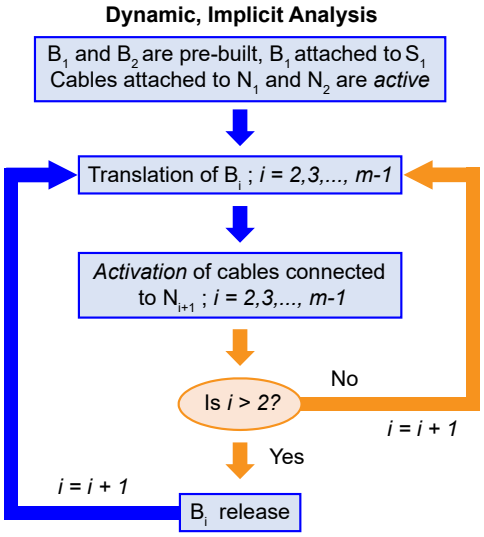

Figure 4.5: Framework of simulation steps.

The initial configuration of the bays and cables for the polygonal ring geometry shown in Fig. 4.2(a) is depicted in Fig. 4.2(b). Points S_1 and S_2 simulate the fixed supports of the truss builder in two-dimensional space. Figure 4.6 shows the boundary conditions used to simulate the assembly process. Truss node N_1 and bay element b_1 are fixed in translation at S_1 ($U_1 = U_2 = 0$ in Fig. 4.6(a)), while bay B_1 is free to rotate throughout the simulation ($UR_3 \neq 0$ for N_1). As bay B_2 is pushed out via the translational DoF (U_1, U_2) of node N_3, node N_2 is allowed to rotate in-plane, forming the first intermediate polygon, a triangle (see Figs. 4.6(a) and (b)). Once B_2 is pushed out, node N_3 is fixed in translation at S_2 while the cables connected to N_3 are activated. The modified DoFs during this activation step have been highlighted in red in Fig. 4.6(b).

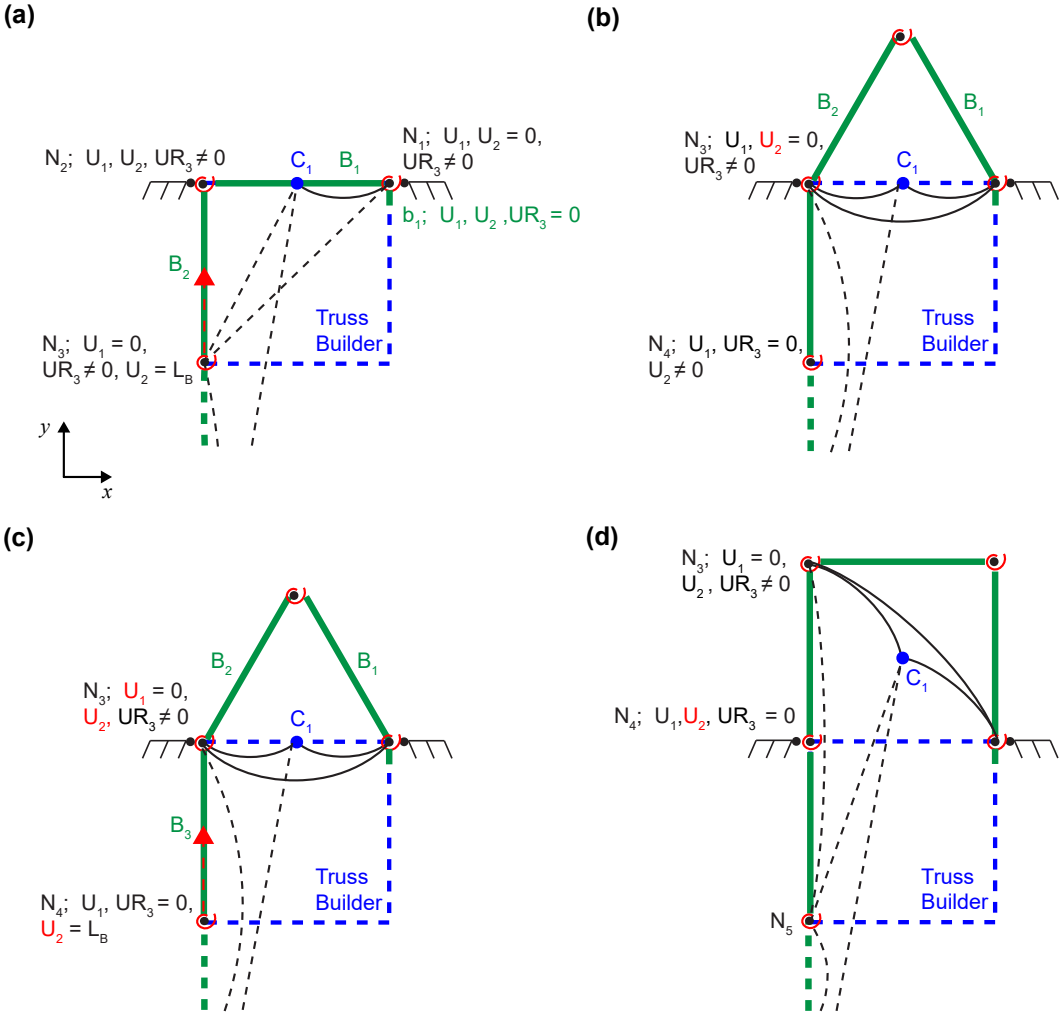

Figure 4.6: Boundary conditions when a) pushing-out bays B_1 and B_2, b) activating cables connected to N_3, c) pushing out bay B_3, and d) activating cables connected to N_4.

For subsequent bays ($i > 2$), the process repeats: bay B_i is pushed out while constrained to the assembly plate (not modeled) by controlling the translational DoFs of nodes N_i and N_{i+1} (highlighted in red in Fig. 4.6(c)). As the corresponding cables are activated, node N_{i+1} is fixed in translation at S_2, while node N_i is also fixed (see U_1 and U_2 in Fig. 4.6(d)). The translational DoF in 1-direction, U_1 at node N_i is released to simulate the retraction of the assembly plate, forming an intermediate polygon with i sides (Fig. 3.5, third column). Throughout, bay element b_2 moves with B_{11}, and at end of the assembly, node N_{12} remains fixed at S_2 alongside b_2. The free nodes of cable net C_j are initially placed at even spacing between S_1 and S_2, and they are free to rotate and translate in the plane as the cables are 'attached' to the perimeter truss during assembly.

4.3 Tuning the Simulation for a Six-Sided Structure

The assembly process simulation involves the interaction of multiple parameters. To ensure accurate results, it was necessary to fine-tune the parameters of the simulation technique. The tuning process used a six-sided structure with six cables and a single interior cable node C_1 (see Fig. 4.7). We begin by identifying the associated parameters.

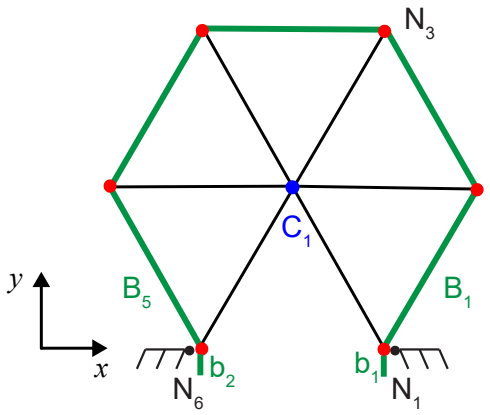

Figure 4.7: Geometry of six-sided structure.

4.3.1 Angle Stops

Figure 4.8(a) shows a section of a typical ring-like truss, with the perimeter truss shown in green and the cables in black. The cable connecting nodes N_{i-1} and N_{i+1} is designed to be shorter than the sum of the lengths of bays B_{i-1} and B_i, as dictated by the cable net configuration:

$$\overline{N_{i+1}N_i} + \overline{N_iN_{i-1}} > \overline{C_{edge,\,i+1}C_j} + \overline{C_jC_{edge,\,i-1}}. \tag{4.3}$$

In the proposed assembly scheme, before bay B_i is pushed out, the edge cable node $C_{edge,\,i+1}$ is held at the front of the truss builder (see Fig. 4.8(b)). As the truss builder pushes out bay B_i mounted on the assembly plate, the cable between nodes $C_{edge,\,i+1}$ and $C_{edge,\,i-1}$ transitions from slack to tensioned. If node N_i is pushed outward relative to the assembly plate, this tensioned cable could potentially jam the plate or become damaged. Hence, to ensure a smooth assembly, the intermediate perimeter truss configurations are required to be convex polygons (see Fig. 3.5, second column), by introducing angle stops at each joint with a torsional spring. Since all bays are defined as a series of co-linear rods in the initial step of the simulation, the angle stop range, α, is limited to a maximum of π radians (see Fig. 4.8(c)), thereby preventing outward kinking of the truss nodes. However, no angle stops are applied at nodes N_1 and N_m $(m = 6)$, allowing them to bend outward as needed to achieve the intermediate polygonal shapes and final truss configuration (see Fig. 4.7). This angle stop definition was applied consistently throughout the simulation study.

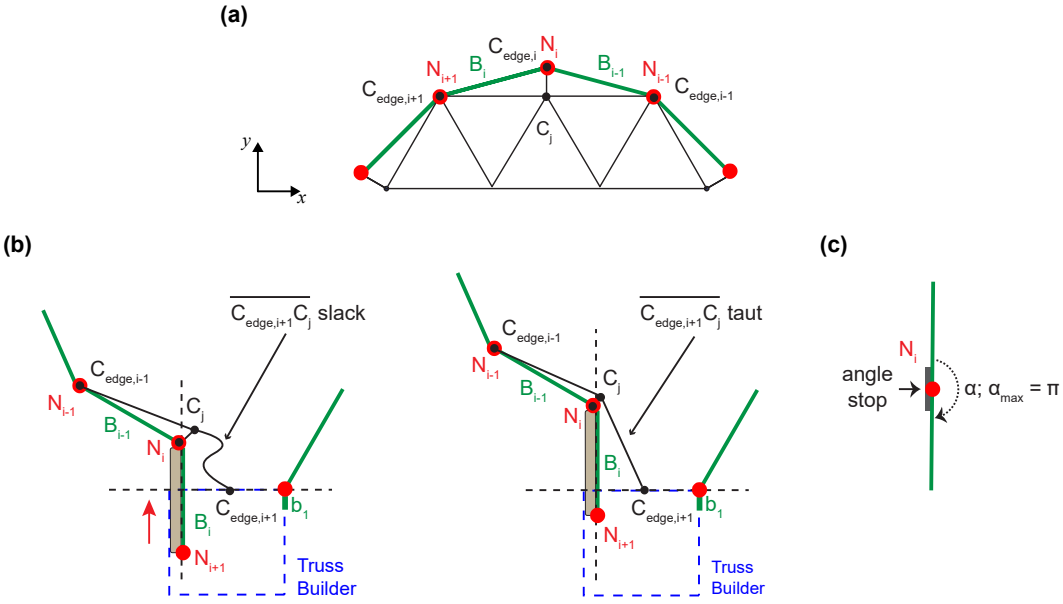

Figure 4.8: Angle stops: a) geometry of the structure, b) cables transitioning from slack to taut during bay push out, and c) definition of angle stop.

4.3.2 Assembly Plate Orientation

The orientation of the assembly plate, i.e., the angle θ at which each truss bay is pushed out with respect to the face of the truss builder is a crucial parameter in the

truss builder design. It imposes a constraint on the range of motion of the structure during assembly. As illustrated in Fig. 4.9(a), pushing out each assembled bay perpendicular to the truss face, as initially proposed, forces the structure to become heavily distorted. Tilting the assembly plate provides more space and allows a more uniform shape (see Fig. 4.9(b)). The angle of the assembly plate, θ, plays a significant role in the process: a distorted shape increases the tension in the cable net and requires additional corrections to align the ring to its intended configuration. Consequently, it is essential to evaluate how the assembly plate angle affects shape distortion to ensure efficient assembly. For the six-sided structure, three assembly plate orientations were selected: $\theta = 90°, 80°, 60°$.

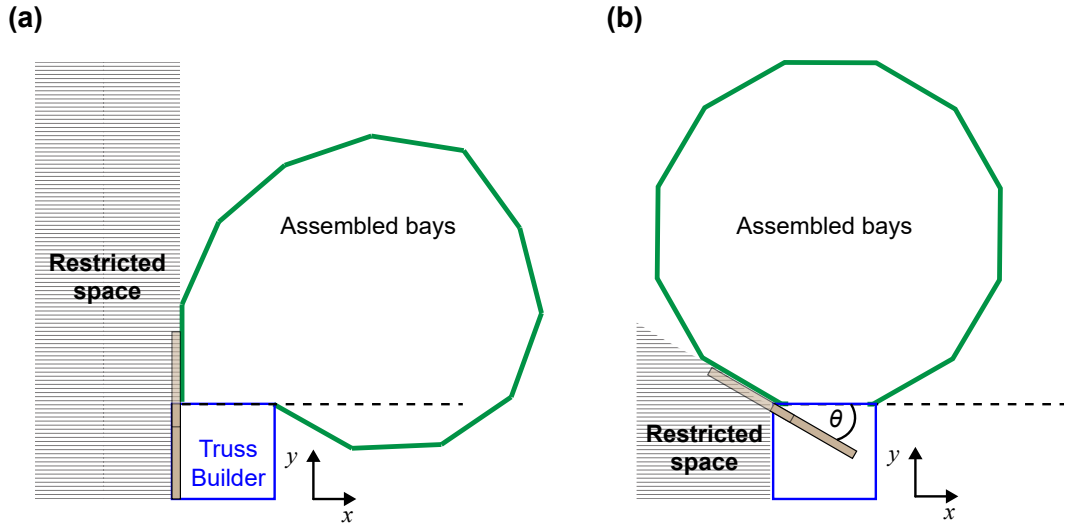

Figure 4.9: Two assembly plate orientations: a) perpendicular to the truss builder face: $\theta = 90°$, and b) tilted at angle $\theta < 90°$.

4.3.3 Damping Coefficients

Since the simulation involves a dynamic integration of the motion of the structure, mass-proportional damping was applied to the moving nodes, particularly C_j. For a given nodal mass, the Rayleigh damping coefficient α_R was selected to be sufficiently high to avoid numerical instabilities. To understand the effect of different damping coefficients, a sensitivity study was conducted for $\alpha_R = 0.5, 5.0, 7.5, 10$, with a nodal mass of 0.020 kg.

Table 4.1 summarizes this sensitivity study, highlighting the effects of different assembly plate orientations and damping factors. The maximum and root-sum-of-squares (RSS) variation of the final axial extensions u_i of the cables from their

expected final values (set at $u_{i,\ expected} = 0;\ i = 1, 2, \ldots, 6$ by design) was used as the metric for comparison. Only simulations that successfully achieved the desired final shape with an RSS error less than or equal to 12 mm were considered. The table shows that all assembly plate orientations produced the desired shape for certain damping factors. While the magnitudes of the variation in extensions change with θ, the smallest variations, approximately one-third lower compared to other angles, and thus the most favorable results, are observed for $\theta = 60°$. The effect of the damping factor magnitude on the variations for a given θ is minimal, as evidenced by the small changes in the corresponding extensions. Therefore, the lowest damping coefficients which allowed for successful completion of the simulations were adopted for each assembly plate orientation.

Table 4.1: Sensitivity to assembly plate orientation and damping coefficient

$\theta(°)$	$\alpha_R(\mathrm{s}^{-1})$	Final shape achieved	$\lvert\Delta u_i\rvert_{max}$(mm)	$\sqrt{\sum_{i=1}^{6} \Delta u_i{}^2}$(mm)
90	0.5	✓	6.84	7.48
	5.0	✓	6.84	7.48
	7.5	✓	6.84	7.48
	10.0	✓	6.84	7.48
80	0.5	×		
	5.0	✓	6.88	7.52
	7.5	✓	6.87	7.51
	10.0	✓	6.87	7.52
60	0.5	✓	4.60	5.09
	5.0	✓	4.56	5.06
	7.5	✓	4.49	5.00
	10.0	✓	4.59	5.09

4.4 Simulation Results for the Six-Sided Structure

Figure 4.10 presents the simulation results for the progression of cable extension during the assembly of the six-sided structure with $\theta = 90°$, alongside snapshots of the intermediate shapes of the structure. Cables are color-coded for clarity. Each snapshot shows only the active cables, while the graph distinguishes between active cables and inactive cables with solid and dotted lines, respectively. At the start of the assembly, B_1 and B_2 are pre-assembled, and cables 1 and 2 are active according to the ISA concept. Vertical lines on the graph mark transitions between different assembly phases: from 'bay translation' to 'cable activation' and then to 'bay release.' The greyed-out region in the graph indicates slack cables ($u_i < 0$).

The results show that all cables successfully reach their unstressed length by the the 100% assembly point, as required. The graph illustrates the evolution of cable net extensions, providing insight into the intermediate shapes of the structure during assembly and confirming whether the final configuration meets expectations. As expected, cables 3-6 experience positive extension at the start of assembly since they are modeled with their final connectivity. However, they are inactive, as indicated by dotted lines, and hence do not exert forces on the structure until activated. This is reflected in the snapshots of the intermediate shapes.

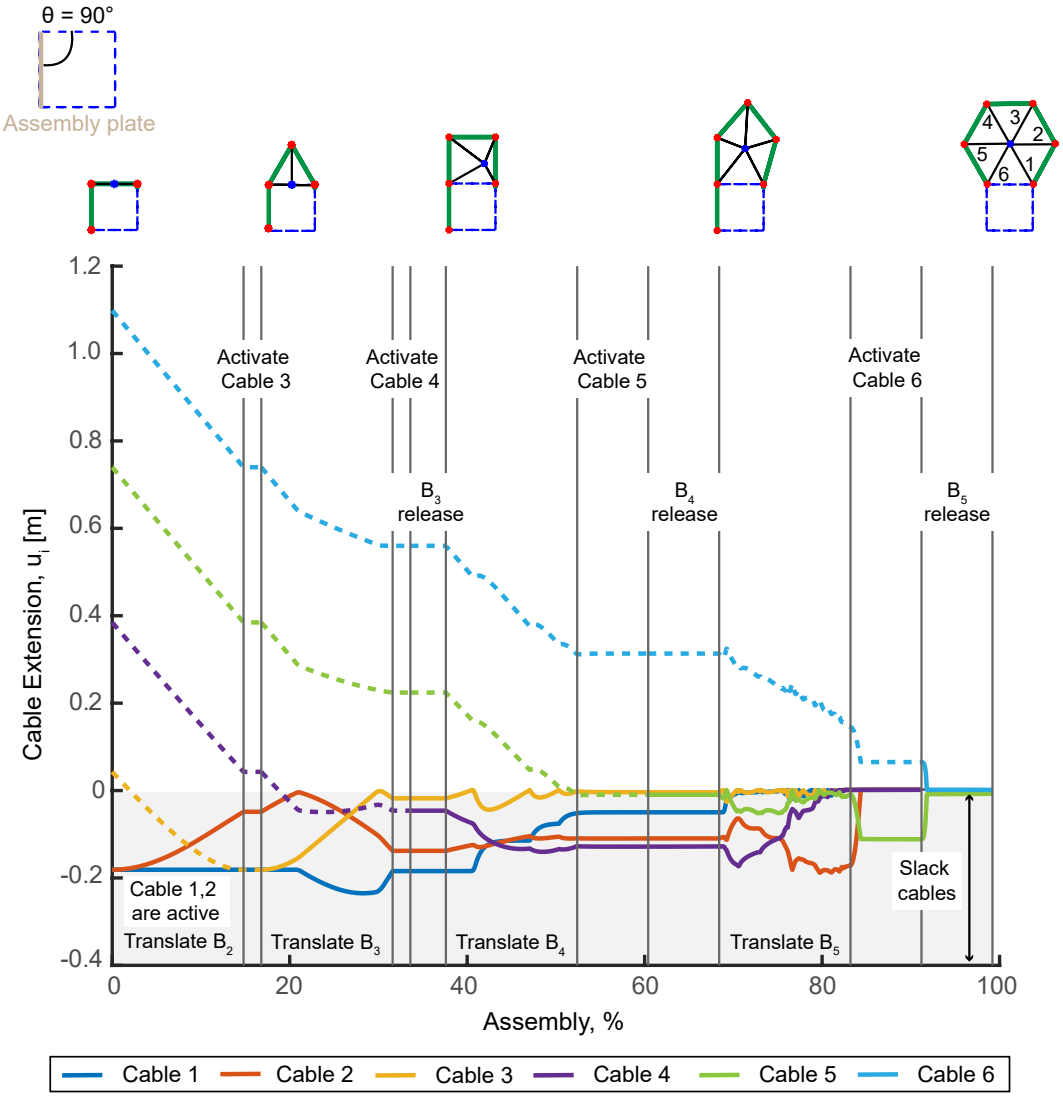

Figure 4.10: Cable extension results for the six-sided structure; $\theta = 90°$.

Another important detail is that each cable is activated when it is near or within the slack region, which in the simulation helps to minimize the dynamic forces

applied to the structure during the activation steps. Throughout the process, at least one active cable remains slack until the final cable is activated and the last bay is released, marking the desired end of the assembly.

Close observation of the intermediate shapes reveals that regular polygons are not achieved upon releasing the respective bays. This is due to the angle stops at the joints, which restrict the anti-clockwise rotation of the truss node at S_2 (see the next bay ready for assembly in the snapshots). The intermediate rings tend to rotate anti-clockwise at S_2, but the angle stops prevent them from going beyond the assembly plate angle. Taut cables may also be responsible for the non-regularity observed in the intermediate polygons. The final polygonal configuration is regular, as intended, with all cables active and nearly prestressed.

Figure 4.11 presents the simulation results for the assembly with $\theta = 60°$. Although the final configuration—a regular hexagon—is achieved also in this case, it is evident that the intermediate shapes vary depending on the value of θ, as emphasized in Fig. 4.12. This variation highlights the significance of the assembly plate orientation to the assembly process.

The effect of the more symmetric structure deployment on the cable interior is particularly evident from the comparison of cable extensions in Figs. 4.10 and 4.11 during the translation of B_5. For the $\theta = 60°$ case, the cable extensions exhibit a smoother transition and reach the desired prestress level more rapidly compared to the $\theta = 90°$ case. This results in a more controlled and gradual activation of the final set of cables, facilitating a more stable and precise completion of the assembly process.

This variability in intermediate shapes is expected to be more pronounced in larger polygonal rings, where the assembly plate angle significantly impacts the geometry and stability of the structure during assembly. The influence of the assembly plate angle on these intermediate shapes and its implications for the assembly of larger structures are discussed in Chapter 5.

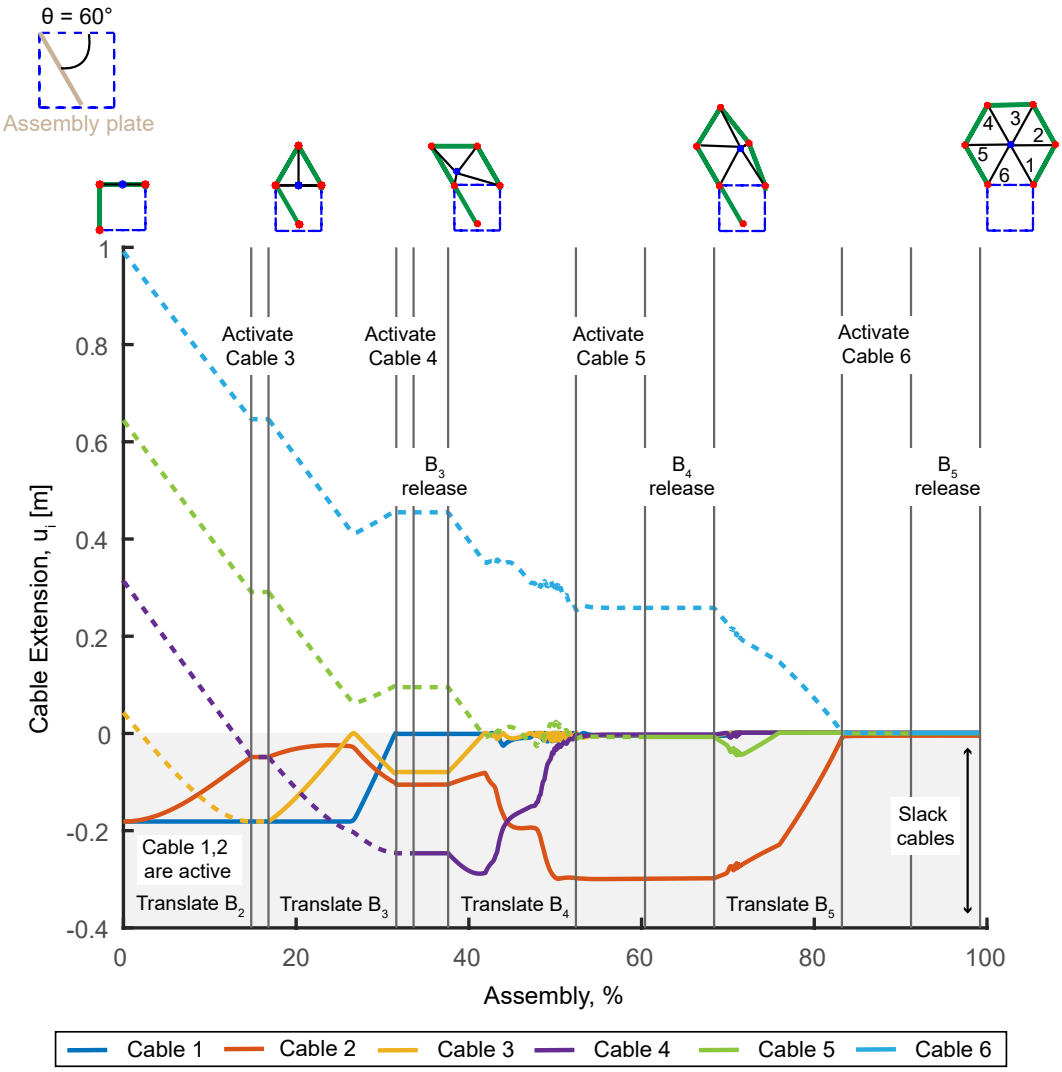

Figure 4.11: Cable extension results for the six-sided structure; $\theta = 60°$.

4.5 Chapter Conclusions

This chapter has introduced the numerical simulation setup for the proposed ISA concept for large polygonal ring-like structures using a two-dimensional finite element model. This model, implemented in ABAQUS/CAE 2020, simulates the kinematics of a six-sided structure with a cable net interior assembled by a single stationary robot. The focus was on modeling the sequential assembly of the truss bays and the attachment of the cable net and ensuring that accurate final configurations could be achieved.

The simulation revealed that achieving the final desired shape—specifically, a regular hexagon—was successful for various assembly plate orientations. However, the intermediate shapes differed significantly depending on the assembly plate orien-

tation, an effect that is expected to be more pronounced in larger polygonal rings. A sensitivity study of damping coefficients demonstrated that varying these values has minimal impact on the magnitude of cable extension variations for a given assembly plate orientation. The lowest damping coefficients that permitted successful simulation completion were adopted for the study. This approach ensured that the simulations accurately reflected the assembly process without numerical instability.

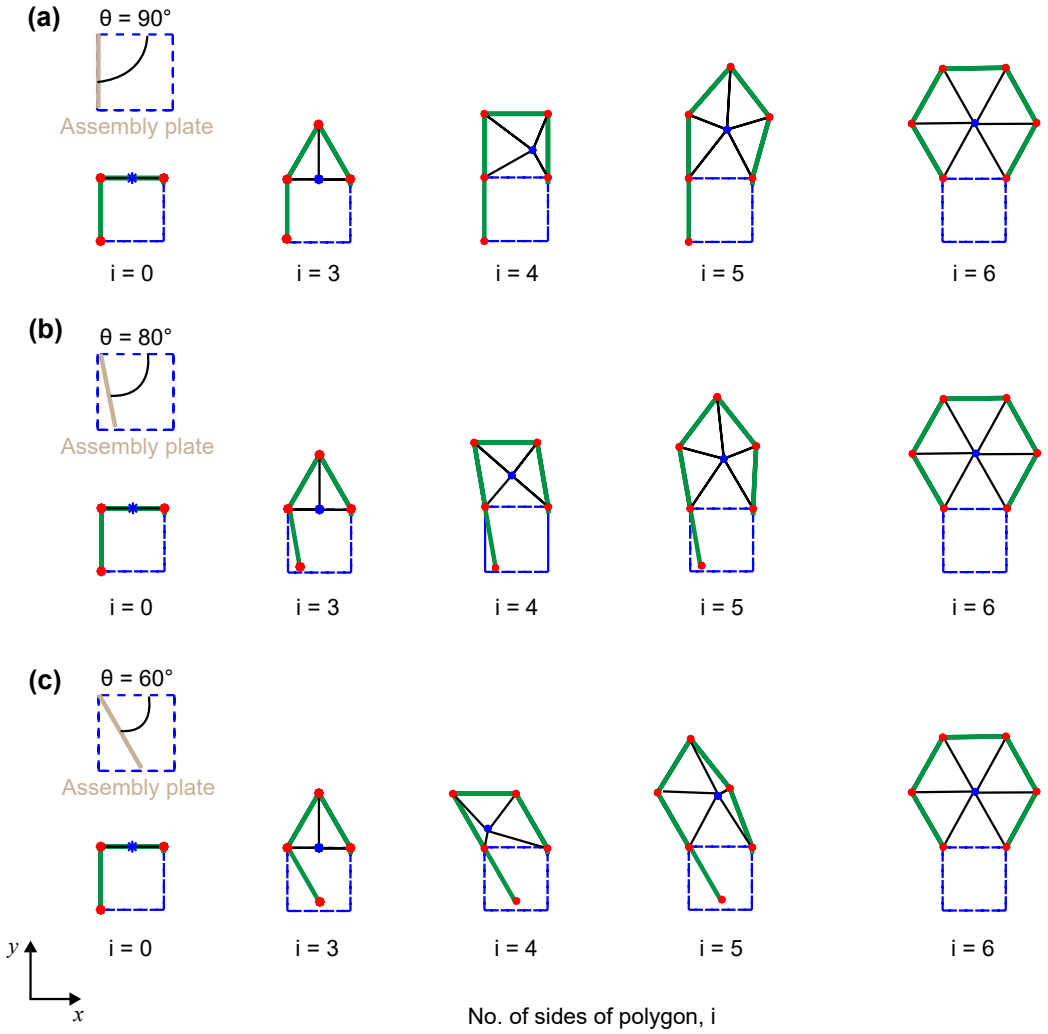

Figure 4.12: Intermediate polygonal shapes: (a) $\theta = 90°$, (b) $\theta = 80°$, and (c) $\theta = 60°$.

The innovative simulation techniques developed offer sufficient confidence at this stage to evaluate the feasibility of the proposed ISA concept for larger ring-like structures. Chapter 5 further explores this by identifying key design considerations and potential improvements to the stationary robot to enhance efficiency and robustness of assembly.

Chapter 5

SIMULATION OF TWELVE-SIDED REFLECTOR

5.1 Motivation

To evaluate the feasibility of the proposed ISA concept for larger structures, a twelve-sided polygonal ring structure with forty eight cable elements was selected as the baseline model (see Fig. 5.1). Using the simulation techniques outlined in Chapter 4, this study aims to explore the inherent challenges of assembling ring-like structures with a cable net interior. Key issues such as potential snags, misalignments, and the critical importance of the assembly sequence are analyzed. Additionally, the approach to prestressing the structure is analyzed to assess its effects on overall structural integrity and efficiency, offering insights into optimizing the ISA process for future large-scale applications.

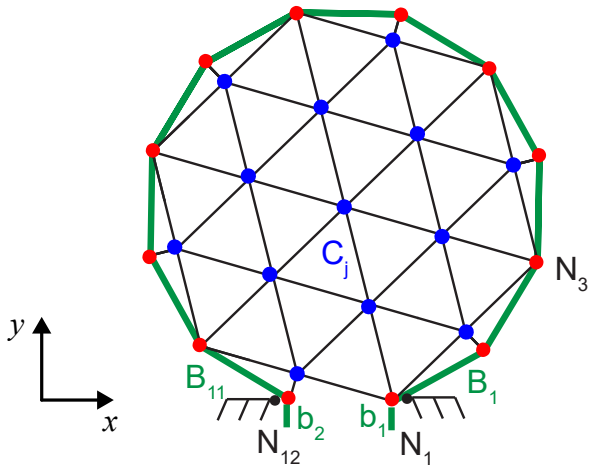

Figure 5.1: Geometry of twelve-sided reflector.

The dimensions and number of bays for the twelve-sided polygonal ring structure were chosen to match the 1.4-meter lab-scale prototype of the ISA concept currently under development, as described in Chapter 6. The original cable net configuration designed for $D = 1.4$ m, using the generalized design method detailed in Chapter 2 was simplified while adhering to the constraints specified in Section 4.2.2. This approach ensures that the simulation accurately reflects the prestress requirements of

the design and remains consistent with the characteristics of the prototype, allowing for a meaningful comparison and assessment of the proposed ISA concept.

5.2 Effect of Assembly Plate Orientation

While the orientation of the assembly plate did not impact the final shape for the six-sided structure, this finding does not hold for larger structures. An intuitive observation is that orienting the assembly plate at the supplementary angle to the interior angle of each i-sided intermediate polygon during assembly, $\theta_{cr,\,i}$, could help avoid distortions or bias in the shape of the ring (see Fig. 5.2). This approach would ensure that the structure naturally forms the correct polygonal shape upon release of the final bay. However, this approach would also require adjusting the plate orientation at each B_i push-out step, increasing process complexity. Therefore the identification of a single effective orientation for the entire assembly is necessary.

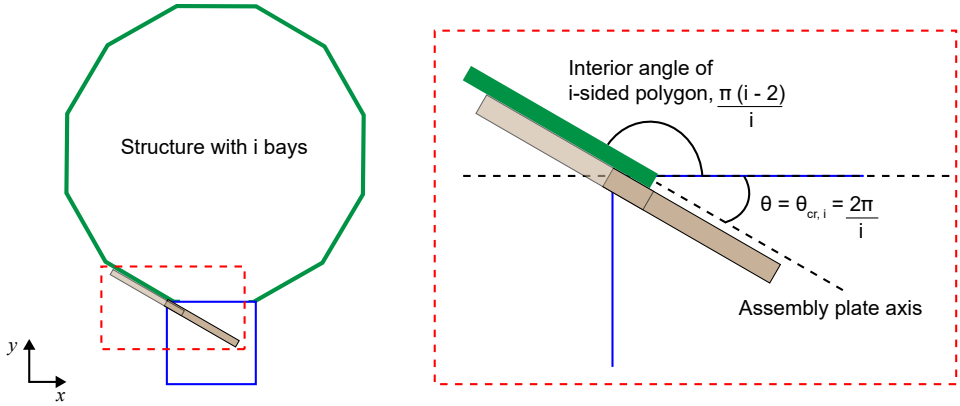

Figure 5.2: Relationship between critical assembly plate orientation, θ_{cr} and interior angle of perimeter truss.

Numerical simulations were conducted using three distinct assembly plate orientations: $\theta = 90°$, $60°$, and $30°$. These angles represent different scenarios: $\theta = 90°$ where the assembly plate is moved perpendicular to the truss support axis, $\theta = 30°$ corresponding to θ_{cr} for a twelve-sided polygon, and $\theta = 60°$, a midpoint between the two. Figure 5.3 shows 11 snapshots of the intermediate shapes during assembly.

For $\theta = 90°$, the shape of the structure is consistently biased to the right as bays are added (see Fig. 5.3(a)), due to the constraint imposed on the left side by the assembly plate. This results in excessive tension on the final set of cables, ultimately jamming the process and preventing the structure from achieving the intended dodecagonal shape upon release of the last bay. In contrast, for $\theta = 30°$, the intermediate polygons are flatter and a clear leftward bias can be seen, with the final

set of bays aligning closely to the desired shape (see Fig. 5.3(c)), as anticipated for $\theta = \theta_{cr,\,12}$. However, this configuration still introduces distortions in the first half of the ring structure, i.e., in bays B_1 to B_5.

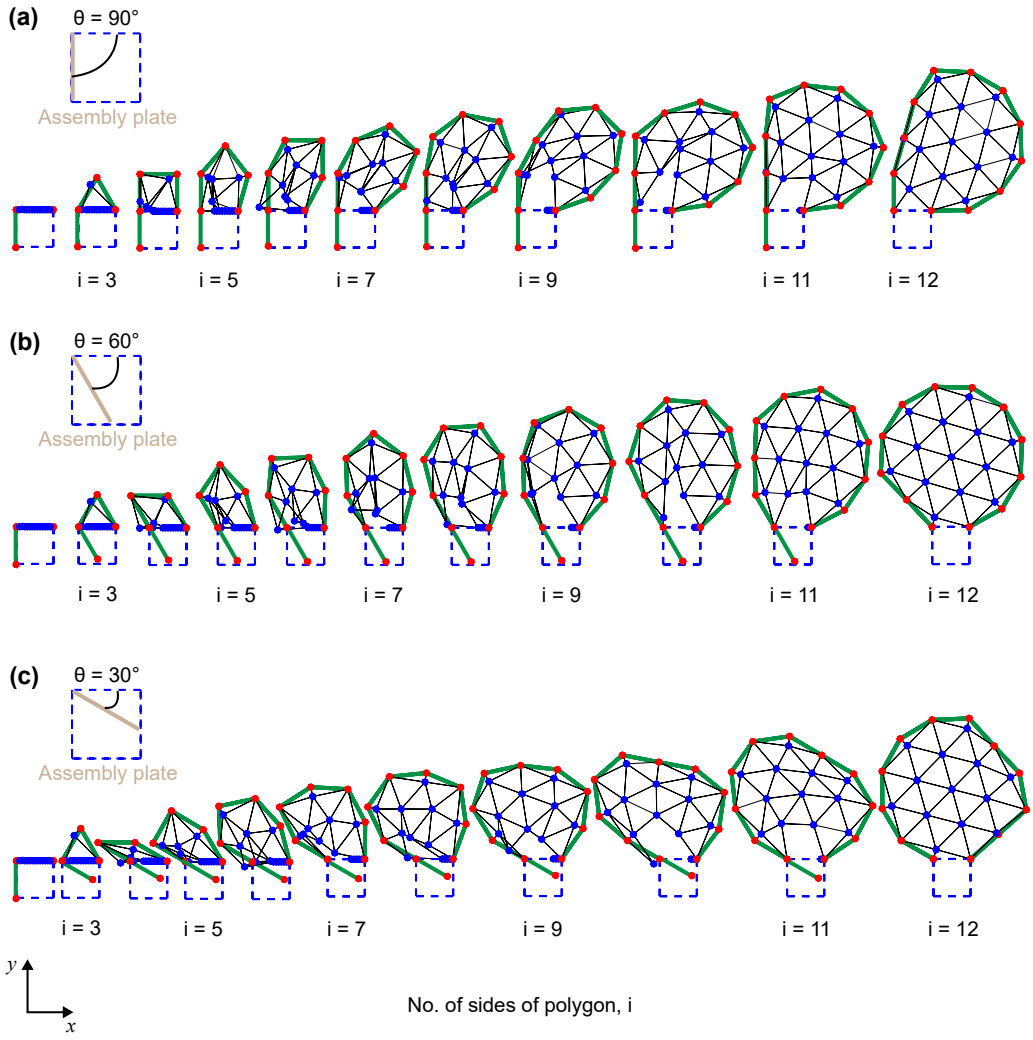

Figure 5.3: Effect of assembly plate orientation: (a) $\theta = 90°$, (b) $\theta = 60°$, and (c) $\theta = 30°$.

The intermediate case $\theta = 60°$, produced the most balanced result (see Fig. 5.3(b)), achieving a configuration that is closest to the target polygonal shape while maintaining relatively symmetric deployment throughout the assembly process. Although determining an angle that achieves the final desired shape while maintaining symmetric intermediate shapes is not straightforward, these results demonstrate that the proposed ISA concept is highly sensitive to the assembly plate orientation. Further optimization of the angle will be important to ensure both precision and efficiency in larger-scale deployments.

5.3 Effect of Prestressing Method

The proposed ISA concept depends on releasing the final bay of the ring to trigger the formation of the desired final configuration and to apply prestress to the structure. However, as discussed in Chapter 4 and Section 5.2, some cables may become excessively tensioned, which can disrupt the remaining assembly process. To address this issue, alternative methods for applying prestress at various stages of assembly were investigated.

A novel approach was developed, yielding promising experimental results with the lab-scale prototype by successfully achieving the intended final shape and effectively prestressing the structure. This method of prestressing is as follows (see Fig. 5.4): after deploying the first two pre-built bays (B_1 and B_2), the edge cable $C_{edge,3}$ is connected to node N_3, and the assembly plate is retracted. At this point, truss support S_1 is moved closer to the assembly plate along the truss support axis. The remaining bays are then assembled and released while S_1 stays stationary in this position, and this is key to ensuring that the cables remain slack during assembly, thereby preventing any disruptions to the assembly process. Once the final bay (B_{m-1}) is released, prestressing is carried out by moving S_1 back to its original position. This has the effect of stretching the cable net and applying the necessary tension to the structure.

It is important to emphasize that initiating the prestressing process of the structure requires the movement of a component at the final stage of assembly. In the original concept, this component was the final bay, whereas in the modified concept, it is the truss support S_1. Regardless of the approach, effective prestressing of the structure can only be achieved if the cables are also sufficiently tensioned by the end of assembly. Essentially, cables must fulfill conflicting requirements at different stages of assembly: they need to remain slack during the assembly process to ensure smooth progression, but they must be tensioned at the end to achieve the correct shape and structural stiffness.

As detailed in Section 4.2.2, the simulation setup is such that cables are intentionally modeled to be nearly slack at the end of assembly, with $u \approx 0$, meaning the final shape is not prestressed. Modifying the prestressing method—from moving the last bay to moving the truss support—only allows the cables to remain slack during assembly, facilitating a smoother assembly process and helping the structure approach the desired final shape more effectively. The process of attaining final prestress will be further examined in Section 5.5.3.

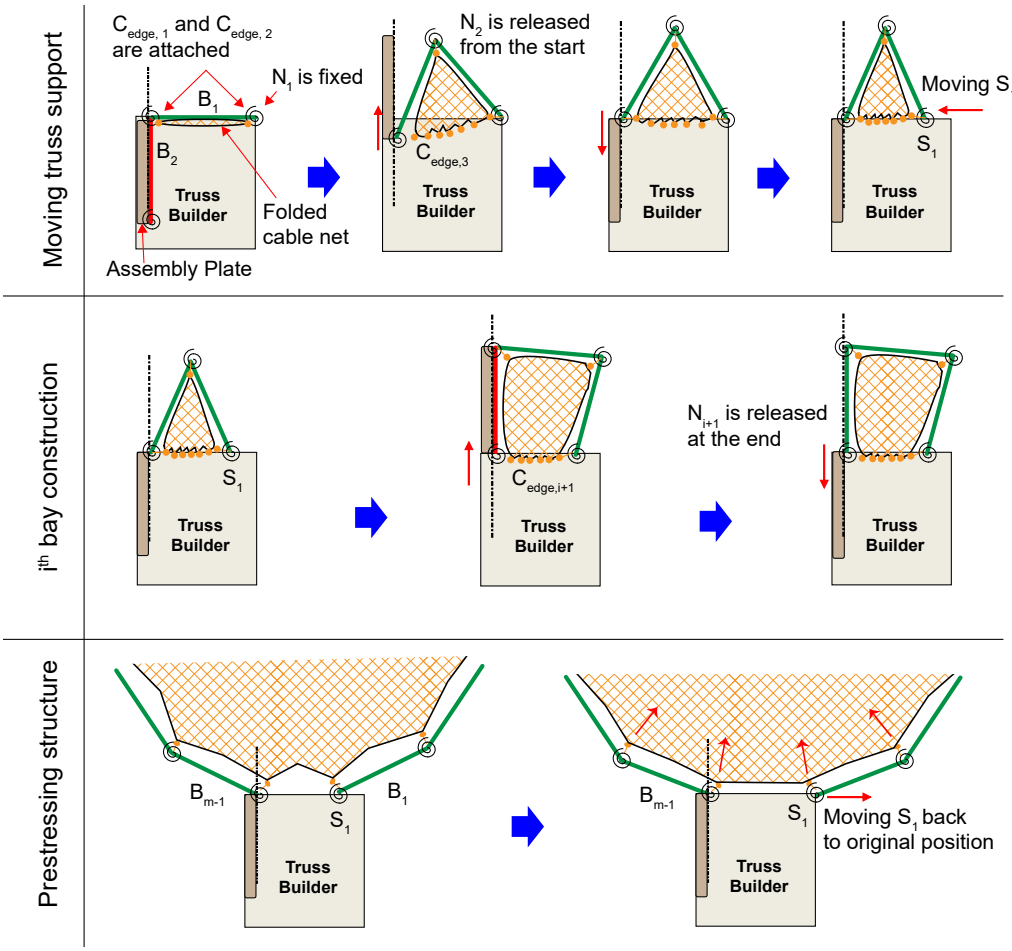

Figure 5.4: Two-dimensional view of the modified prestressing method: moving truss support, i^{th} bay assembly and prestressing the structure.

Figure 5.5 shows the simulation results for both methods of prestressing, with the assembly plate set at $\theta = 60°$. The deployment of the ring for the moving truss support case (see Fig. 5.5(b)), remains relatively symmetric and similar to the case of the moving last bay (see Fig. 5.5(a)), though the former is stretched along the y-direction due to the truss supports being positioned closer together. After releasing the last bay, the polygonal shape for the moving truss support case closely approximates the final shape achieved with the moving last bay case (see $i = 12$ in Fig. 5.5(a)). However, the final adjustment of resetting the truss support triggers the formation of precise polygonal shape of the truss, transforming the assembly from its preliminary state into the desired configuration, as shown in Fig. 5.5(b). This outcome confirms the effectiveness of the modification and underscores the critical importance of considering not only the effect of the assembly plate orientation but also the prestressing method in achieving the desired final shape.

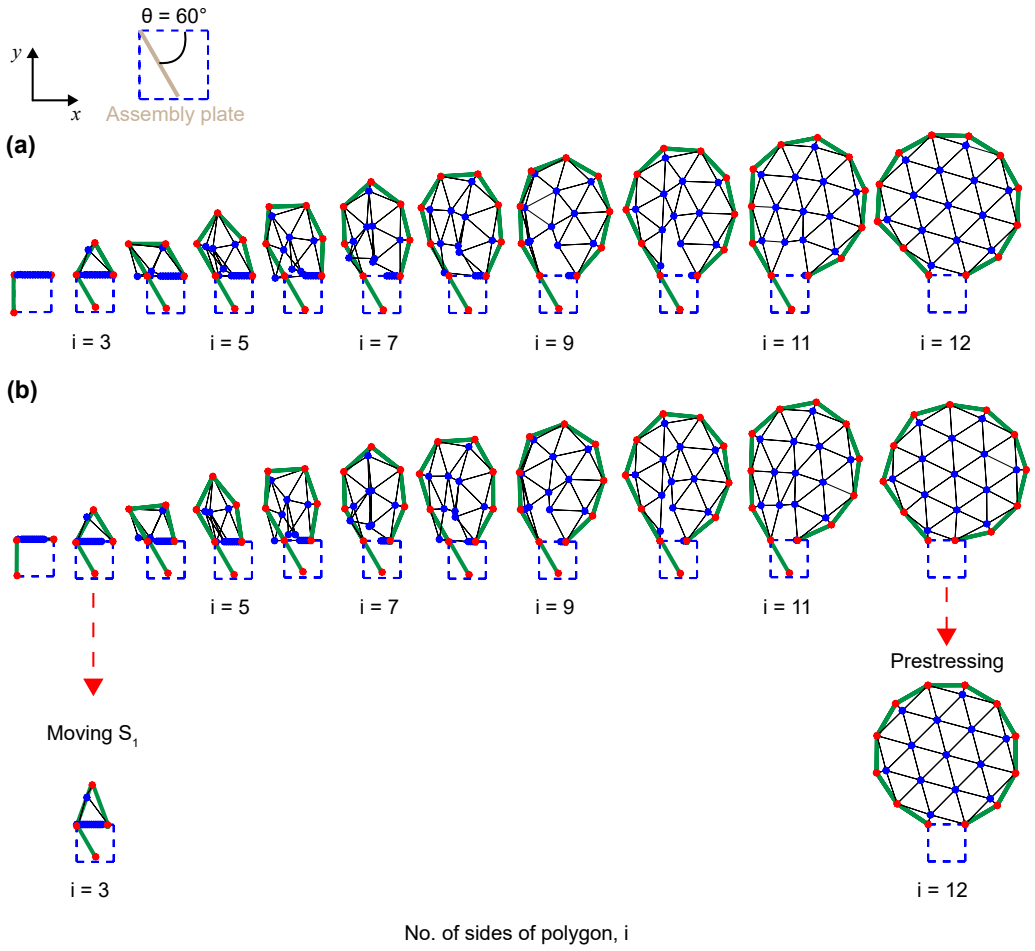

Figure 5.5: Effect of the prestressing method: $\theta = 60°$, (a) moving last bay: S_1 is fixed (b) moving truss support: S_1 is moved by 0.1 m at the start and reset at the end of assembly.

5.4 Effect of Cable Net Orientation

The ISA concept replaces one of the bays with the truss builder, that supports the structure during and after assembly. While the six-sided structure's cable net remains symmetric relative to the truss support, regardless of the chosen bay, the twelve-sided structure does not share this symmetry (see Figs. 4.7 and 5.1), indicating that there are two options for placing the truss builder, as illustrated in Fig. 5.6. Hence there are two possible orientations for the cable net relative to the truss builder. A comparison of these orientations highlights a significant difference: orientation 2 includes a cable element connecting node N_{12} to node N_{10}, while orientation 1 does not. This difference is significant, particularly when relying on the release of the last bay B_{m-1} to trigger the final polygon formation, prestressing the structure. In orientation 1, it may be more difficult to achieve the desired shape near node N_{11}.

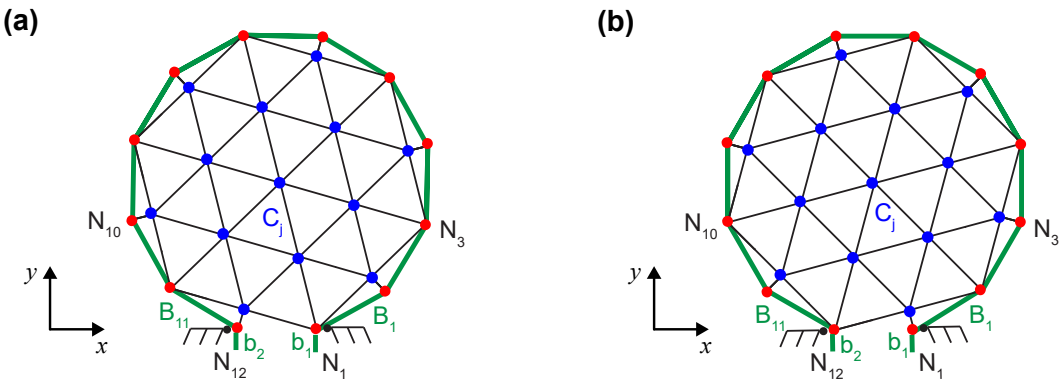

Figure 5.6: Two configurations of the cable net: (a) orientation 1 (b) orientation 2.

Figure 5.7 illustrates this with simulation results for both orientations, prestressing the structure by moving the last bay and at an assembly plate angle of $\theta = 60°$. The final configurations are mirror images, with key differences during assembly emphasizing the importance of the cable net configuration near the nodes. In orientation 1, the last two bays are collinear at nodes N_{10} through N_{12} as expected, while in orientation 2, the first two bays are collinear at nodes N_1 through N_3.

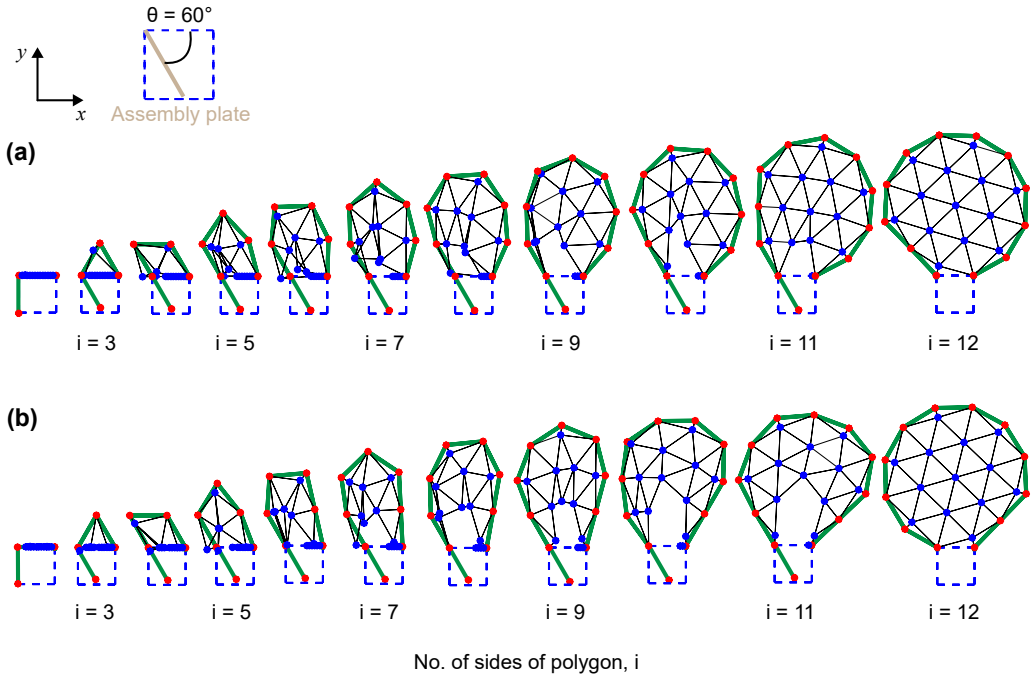

Figure 5.7: Effect of cable net orientation relative to the truss support: prestressing by moving last bay and at $\theta = 60°$, (a) orientation 1 (b) orientation 2.

Examining the final configurations for the case of prestressing the structure by moving the truss support (see Fig. 5.8) shows that both orientations achieve the desired polygonal shape for this method of prestressing. A comparison of truss shapes before prestressing shows similar differences between the two orientations as observed when moving the last bay. This suggests that it is indeed this final step that enables the structure to achieve the desired configuration, regardless of the cable net orientation. Thus, the orientation of the cable net is considered more critical when prestressing relies on the movement of the last bay.

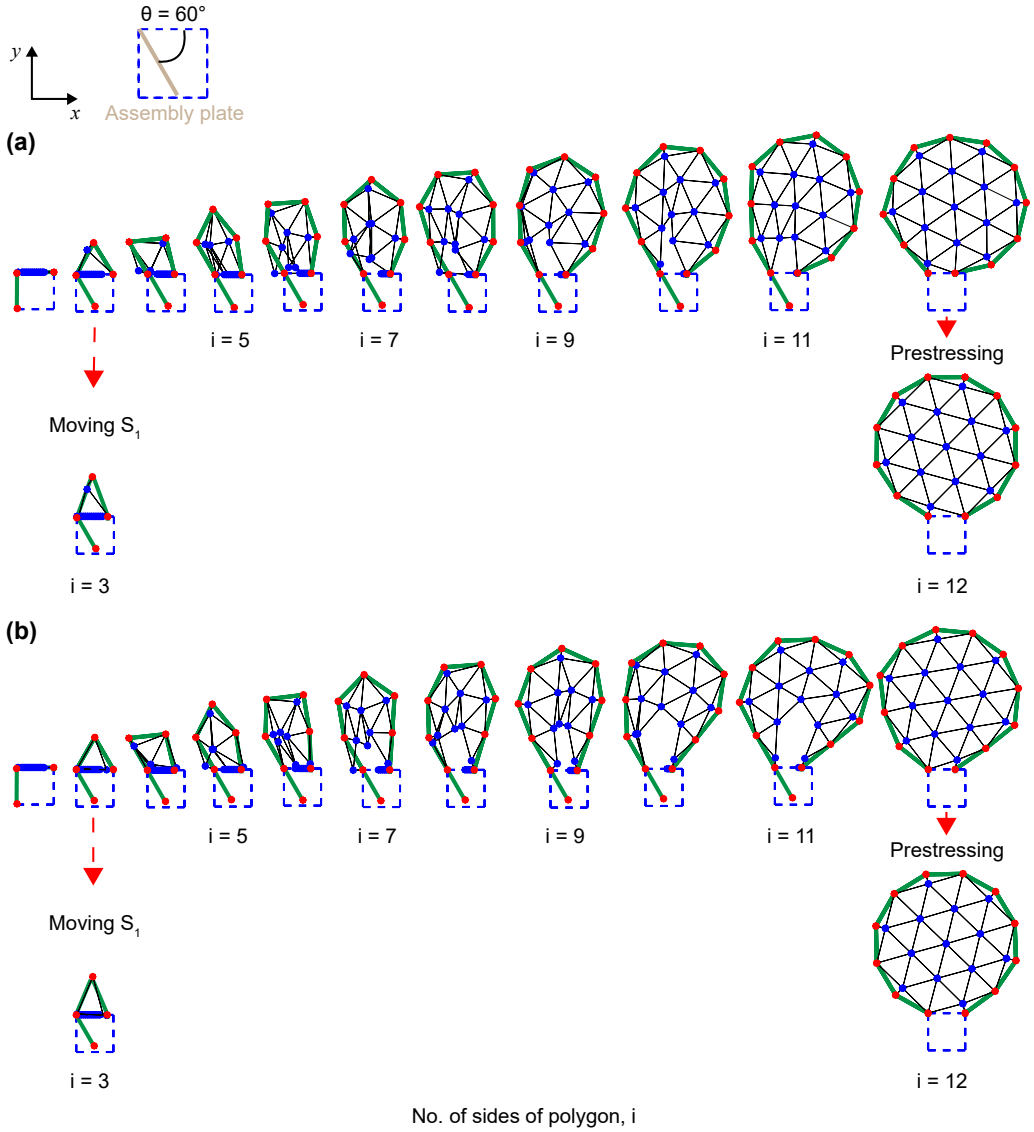

Figure 5.8: Effect of cable net orientation relative to the truss support: prestressing by moving truss support and at $\theta = 60°$, (a) orientation 1 (b) orientation 2.

5.5 Further Considerations for Assembly Simulation

5.5.1 'Jamming' Condition

In some instances, nodes became 'jammed' during assembly disrupting the process. This led to the conjecture that this occurs when the active cables and the truss form a "tensegrity" structure that self-locked and could not move. This issue was resolved by introducing a disturbance into the structure, by applying small displacements to affected truss nodes, which allowed the assembly to proceed as intended. For example, Figure 5.9 shows a case where the assembly became jammed during the activation of cables connected to node N_{10} indicated by black dotted lines). Moving node N_9, as indicated by the red arrows (see Fig. 5.9(a)), prior to the cable activation step allowed the cable activation step and therefore the overall simulation to continue till completion, and obtain the final configuration indicated in Fig. 5.7(b).

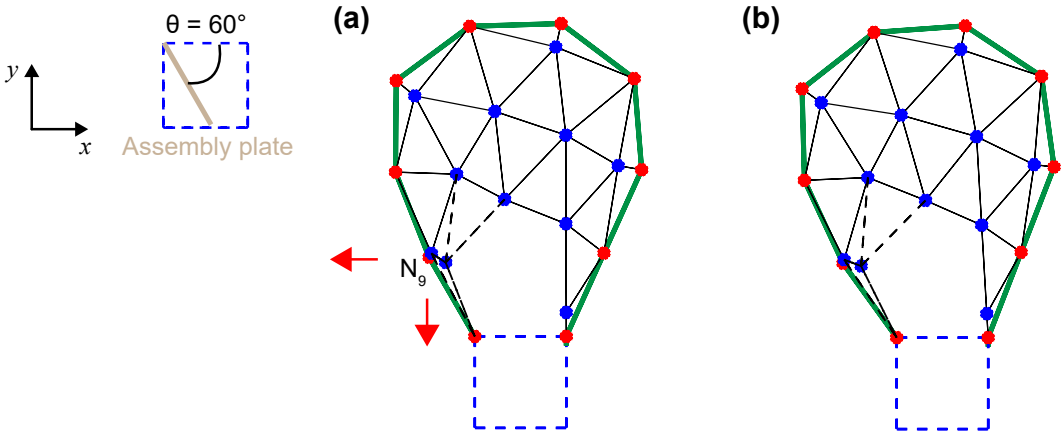

Figure 5.9: 'Jamming' condition for $\theta = 60°$, orientation 2 and prestressing by moving last bay: (a) 'jammed' configuration, and (b) resolved configuration.

5.5.2 Cable Activation and Bay Release Sequence

It was also observed that the sequence of steps towards the end of the assembly—specifically the order of 'cable activation' and 'bay release'—had a significant impact on the process. This is caused by large tensions in the cables that develop due to the constrained position of the last bay on the assembly plate, which in turn disrupts the assembly. Specifically for the $\theta = 60°$ case, releasing bay B_{11} before activating the cables connected to node N_{12} enabled the assembly to be completed successfully and achieve the desired final shape. This adjustment was effective even when moving the last bay for prestressing, demonstrating the critical role of step sequencing in overcoming tension-related issues and ensuring successful assembly.

5.5.3 Prestressing at the Final Assembly Stage

Referring to the case shown in Fig. 5.3(b), although the simulation did not 'jam,' the final shape is not fully correct, because node N_{11} is collinear with nodes N_{10} and N_{12}. Upon examining the corresponding graph that tracks the evolution of cable extensions, particularly during the last stage of the assembly (see the insert in Fig. 5.10(a)), it is evident that some cables have become slack, which likely explains the deviation in the final configuration.

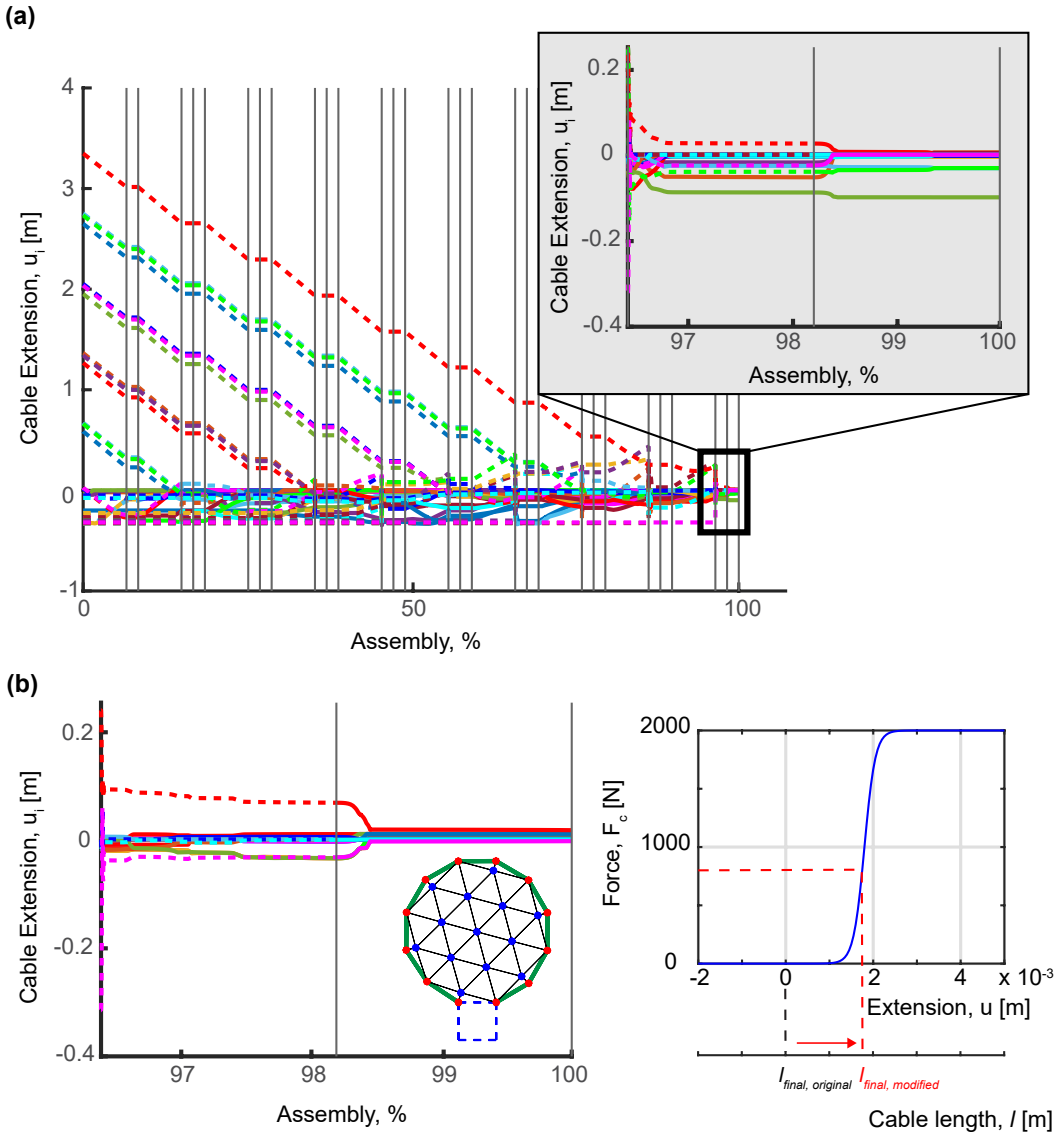

Figure 5.10: Cable extension results for the twelve-sided reflector: $\theta = 60°$, orientation 1 and prestressing by moving last bay, (a) original cable stiffness definition, and (b) modified cable stiffness definition to reflect prestress.

According to the cable stiffness definition discussed in Section 4.2.2, the cables were initially designed to be unstressed at the end of assembly (i.e., at $u \approx 0; F_c \approx 0$) to allow for smooth continuation of the assembly process. However, if the stiffness is redefined by adjusting the final length of the cable so that cables are prestressed at the end of assembly (i.e., at $u \approx 0; F_c \neq 0$), the cables will have to remain under tension as intended, ensuring the correct shape is achieved. This is demonstrated in Fig. 5.10(b), where the modified cable stiffness leads to the desired final configuration, as shown in the inset.

In summary, the successful completion of the ring-like structure in the simulation, along with its effective prestressing, relies on both the prestressing method and the cable stiffness model used. The chosen prestressing approach ensures uninterrupted assembly (see Fig. 5.5), while the stiffness model is crucial for reflecting the actual prestress at the end. Maintaining cable tension with an appropriate stiffness model enables the structure to achieve the desired configuration and stability.

5.6 Chapter Conclusions

This chapter has addressed, through simulations, the major challenges of assembling and prestressing large polygonal-ring structures using the proposed ISA concept. These difficulties are compounded by the challenge of accurately representing real-world conditions in simulations. However, it is essential to interpret the simulations carefully, as robust simulations become increasingly important for predicting intermediate assembly shapes and ensuring continuity as the structure scales, given that full-scale models are impractical for optimizing ISA concepts.

Simulations of a twelve-sided polygonal ring revealed that the assembly plate orientation and prestressing method are critical in ensuring successful assembly and achieving the final desired configuration. Specifically, an assembly plate angle of $\theta = 60^\circ$ offered the best balance, avoiding excessive distortions during intermediate stages. That said, the simulations suggest there may be multiple angles for successful assembly, indicating a solution space rather than a single, unique solution.

The key to the success of the ISA concept is the method of prestressing, whether by releasing the final bay or adjusting the truss support position. Both methods, albeit novel, were shown to be effective, provided the cables are sufficiently tensioned at the end of assembly. Additionally, ensuring smooth progression through assembly required careful sequencing of steps, particularly during the final stages where premature cable tension could cause disruptions.

The numerical simulations have demonstrated the importance of a carefully-defined cable stiffness model, where the correct application of tension ensures that the final structure forms the desired polygonal shape per original design. Adjusting the stiffness model to reflect actual prestress at the end of assembly played a crucial role in maintaining the required structural integrity. Overall, this simulation study captures key design features and provides a fundamental understanding of how different assembly sequences, assembly plate orientations, and cable net configurations affect the process. It also underscores the need for further optimization of the assembly parameters, including plate orientation and prestressing techniques, to achieve precision and efficiency in future large-scale ISA applications.

Chapter 6

EXPERIMENTAL DEMONSTRATION OF ISA CONCEPT

This chapter includes both published work from the following proceedings and new, unpublished sections:

J. Suh, S. P. Dassanayake, and S. Pellegrino, "In-Space Assembly of Large Mesh Reflectors," in *AIAA SCITECH 2025 Forum [Accepted]*, 2025.

J. Suh, S. P. Dassanayake, M. Thomson, and S. Pellegrino, "Scalable Concept for Reflector Antenna Assembled in Space," in *AIAA SCITECH 2024 Forum*, 2024, p. 0823. DOI: 10.2514/6.2024-0823.

J. Suh, S. P. Dassanayake, M. Thomson, and S. Pellegrino, "In-Space Assembly of Large Mesh Reflector Antennas," in *Aerospace Structures, Structural Dynamics, and Materials Conference, SSDM 2024 [Technical Presentation]*, 2024, p. 137 740.

J. Suh, S. Dassanayake, M. Thomson, and S. Pellegrino, "Concept for In-Space Assembly of Large Reflector Antennas," in *41st ESA Antenna Workshop ESTEC*, 2023.

6.1 Motivation

In parallel with the simulations described in Chapters 4 and 5, the DARPA NOM4D team (Dr. Jong-Eun Suh, Alan Truong and Charles Sommer) at the Space Structures Lab is constructing a lab-scale prototype to demonstrate the proposed ISA concept in space by 2026. This prototype features a twelve-sided reflector with a diameter of $D = 1.4$ meters. It is modularly designed and will be assembled using a truss builder prototype.

These experiments are crucial for validating the findings of the simulations. Specifically, these tests will help verify the accuracy of the two-dimensional simulation model in predicting the kinematics of the three-dimensional assembly process and evaluate whether the identified design considerations—such as assembly plate orientation, method of prestressing, and cable net orientation—are broadly applicable. This validation is particularly important given that future predictions about the kinematics of larger structures will rely on two-dimensional simulations.

This chapter compares the results from the lab-scale experiments with those from the simulations to evaluate the applicability and accuracy of the two-dimensional model in predicting the behavior of larger, more complex structures. This comparison will offer valuable insights into the reliability of the simulations and their potential for scaling to full-sized applications.

6.2 Design of In-Space Assembly Facility

To evaluate the feasibility of the proposed ISA concept, prototypes of each component, including the truss builder, have been manufactured and are currently being demonstrated in the laboratory. Figure 6.1 shows a CAD illustration of the target reflector. For an aperture size of 1.4 meters, the design outlined in Chapter 2 specifies $n = 4$ subdivisions of the reflective surface, which necessitates 12 bays for the perimeter truss. Since the truss builder substitutes the final bay of the perimeter truss, a total of 45 struts—comprising 22 longerons, 12 battens, and 11 diagonals—along with 24 joints, are required. The dimensions for the longeron, batten and diagonal (see Fig. 6.1(b)) are determined based on the geometry of a reflector with an F/D ratio of 1.0.

6.2.1 Lab-scale Reflector Prototype

Figure 6.2 illustrates the modular design of the reflector's structural components, intended for assembly by a simple robot, to minimize system complexity. A general overview of the reflector prototype is as follows. The joints are 3-D printed

using Polylactic Acid (PLA) with a CraftBot Plus Pro printer (see CAD image in Fig. 6.2(a)) and include bearings and torsional springs to provide rotation and stiffness.

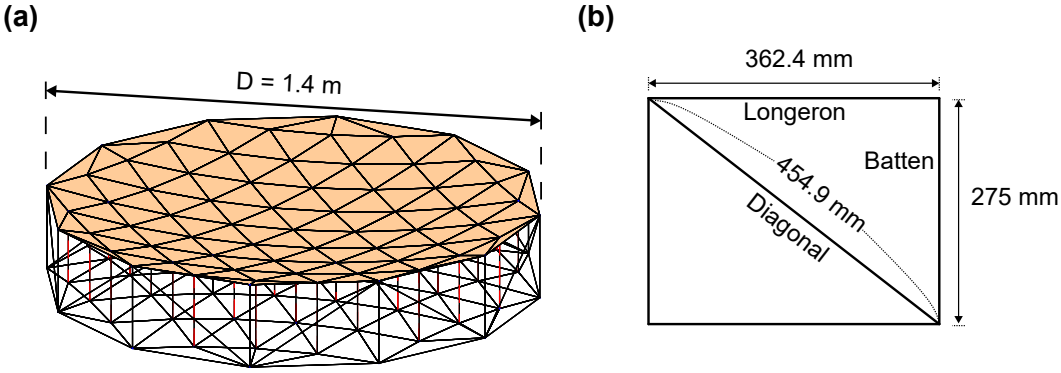

Figure 6.1: Lab-scale demonstration: a) target reflector, and b) dimensions of struts.

The initial prototype described here employs both permanent and electromagnets to secure the joints to the assembly plate. Each joint features recessed surfaces with permanent magnets to assist in aligning the struts. The struts, made from 6 mm diameter pultruded composite tubes, are equipped with magnetized caps that fit securely into these slots through a combination of friction and magnetic attraction, see Figs. 6.2(a) and (b). A circular permanent magnet, along with guiding cones, aids in mounting the joints on the assembly plate. The assembly plate is equipped with electromagnets that activate during bay construction and deactivate during bay release, enabling the connection between the joint and the assembly plate.

The cable net assembly for the mesh reflector includes a front and rear cable net and tension ties. The nets are made from 50 μm thick Kapton film, patterned with the design obtained for $D = 1.4$ m and $F/D = 1.0$, per Section 2.2.1. The front net has a Nylon knitted mesh attached underneath, and a push-latch device connects the nets to the perimeter truss joints, see Fig. 6.2(c). The tension ties, depicted in Fig. 6.2(d), consist of extension springs and strings and are used to maintain the tension of the net. The string length is specifically designed to achieve the necessary tension in the cable net assembly when fully deployed. The springs are sealed in rubber tubes to prevent tangling. The net prototype is stored in a fan-folded configuration within the truss builder. Before each bay release, the push-latch devices at the cable net nodes $C_{edge,\,i}$ are sequentially attached to the corresponding truss joints.

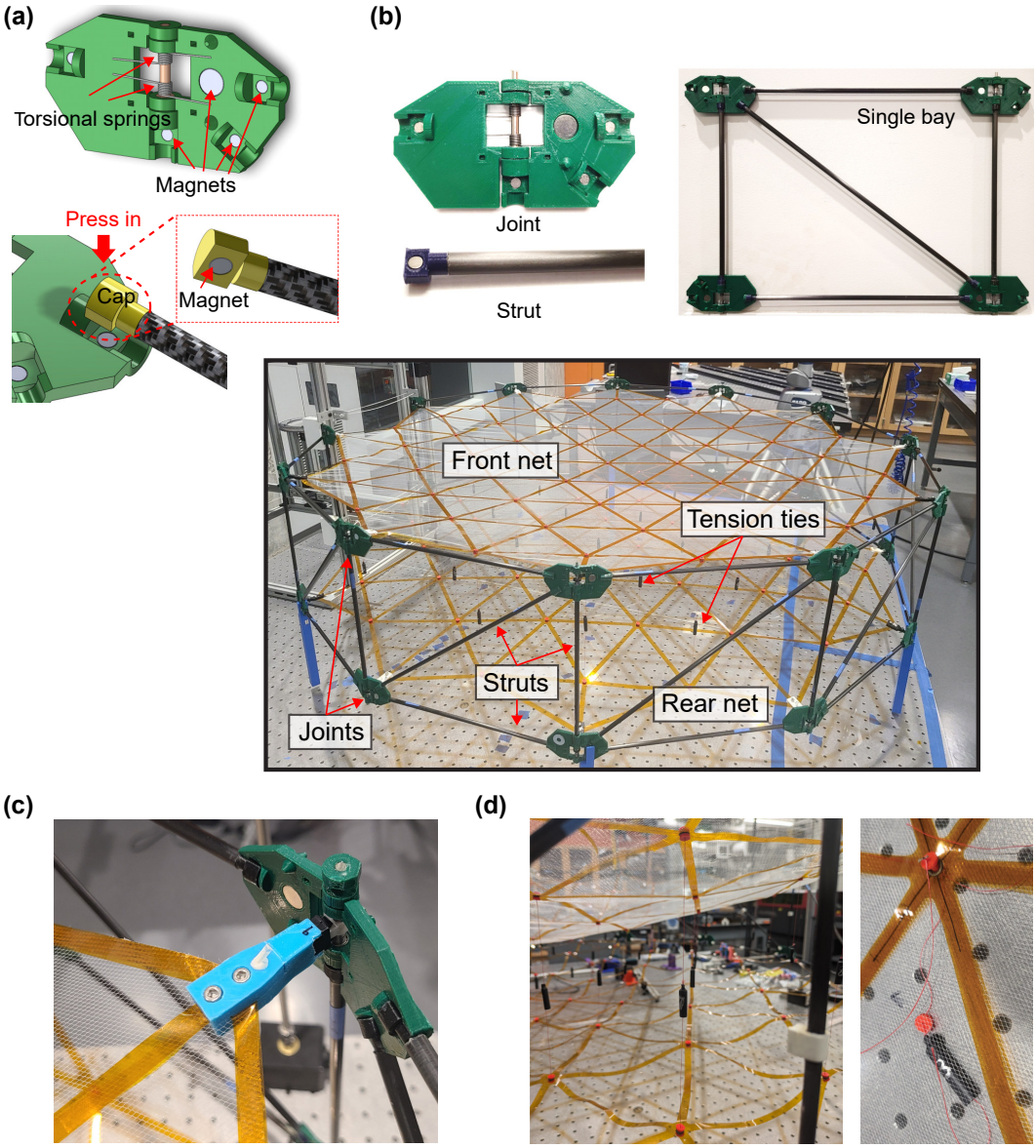

Figure 6.2: Reflector prototype, $D = 1.4$ m: a) CAD drawing of the joint and joint-strut attachment, b) prototypes of the joint, strut, and a single bay, and prototype of cable net with c) a push-latch device installed at the outer node of cable net and attached to the truss, and d) a tension tie.

6.2.2 Truss Builder Prototype

The truss builder prototype (Fig. 6.3(a)) consists of the following key components: the assembly plate, the strut storage, and the manipulator. It performs four major robotic operations, each supported by specific mechanical devices.

The sliding assembly plate handles the 'bay push-out and retraction,' while the joint mounting plates, equipped with electromagnets, secure the joints during

construction, facilitating the 'bay hold and release.' The 'bay construction' involves the joint and strut storage and is carried out by the manipulator, which has 4 DoF (translation in x, y, and z axes, and rotation in Rz). The manipulator, which includes two linear stages, a push actuator, and a rotator, positions the struts and joints from the storage onto the assembly plate (Fig. 6.3(c)). The strut storage is arranged around the perimeter of a circular drum, rotating to bring each strut to the pick-up position. The manipulator's electromagnet interacts with the permanent magnets in the strut sleeves to secure and release the struts. The sleeves are designed to prevent strut rotation during manipulation.

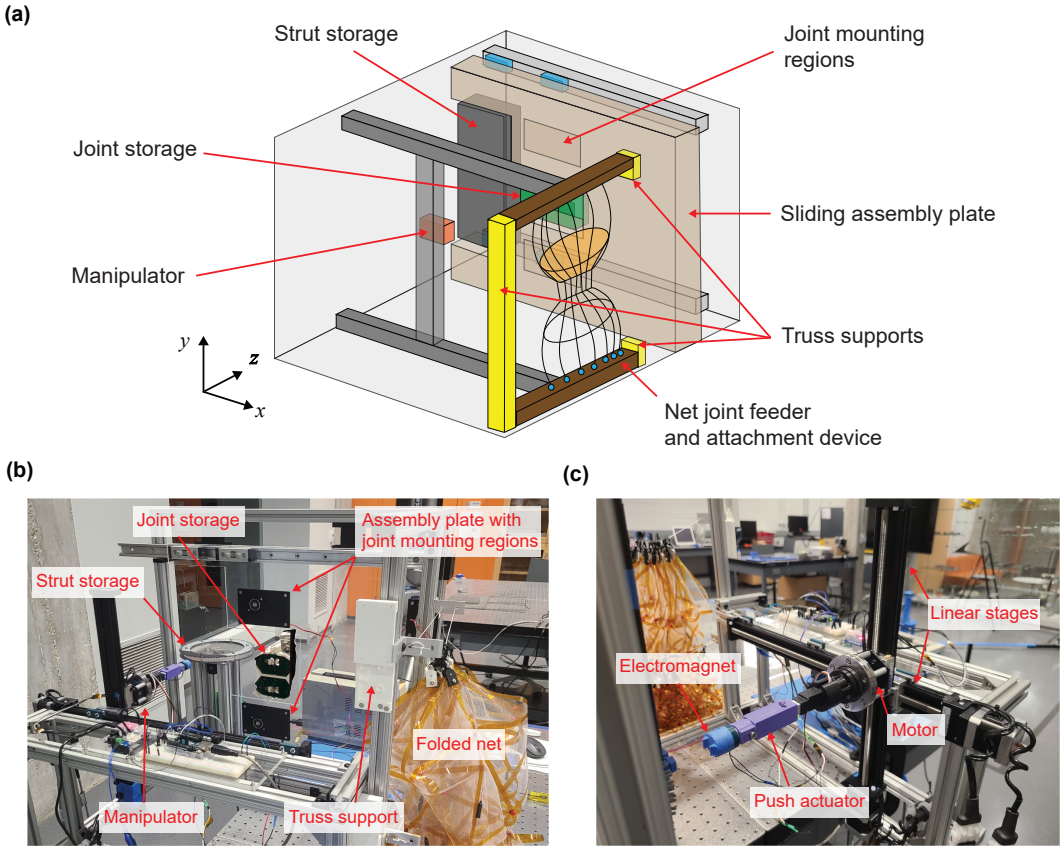

Figure 6.3: Truss builder prototype: a) schematic drawing of truss builder and components, and prototypes of: b) truss builder and c) manipulator.

The 'net attachment' is accomplished by a net joint feeder and attachment device, which organizes the push-latch devices in the order of truss assembly and attaches them to the corresponding truss joints before the assembly plate retracts.

Once a bay is assembled, electromagnets mounted in end fixtures at the edge of the truss builder (i.e., truss supports introduced in Chapter 4, see Fig. 6.3(a)) hold

the released bay, providing sufficient clearance for the assembly plate to retract for the next construction cycle. A prototype based on this design is shown in Figs. 6.3(b) and (c).

6.3 Design Considerations

Efforts were made to validate the design considerations identified from the two-dimensional simulations in Chapter 5. Specifically, two assembly plate orientations, $\theta = 90°$ and $\theta = 60°$, were tested, along with two prestressing methods: moving the last bay and adjusting the truss support. It was quickly determined that the cable net orientation 2 was the preferred option, as it effectively mitigated excessive tension in the cables, reducing the risk of damage during the assembly process. This orientation provided better control over the cable tension and structural integrity.

6.3.1 Angle Stops and Assembly Plate Orientation

In the first experiment with a 90° assembly plate, the structure was assembled manually. One critical difference between this experiment and the simulation was the absence of angle stops in this version of the prototype. Without these stops, the structure had the freedom to form concave polygons during assembly, which posed the risk of overstretching and potentially damaging the cables that support the structure, see Fig. 6.4(d). These kinks and deformations required manual intervention to correct the shape and ensure that the assembly could continue. This manual correction process, while effective for this test, underscored the crucial role of angle stops in automated operations. By constraining the structure's movement and preventing the formation of concave polygons, angle stops help to preserve the integrity of the cables and streamline the assembly process, ensuring that the structure deploys with greater precision and less risk of damage.

Figure 6.4(e) shows the final assembled reflector achieving the desired shape. However, it is important to note that this outcome is largely due to manual interventions, and the shape might not have been achieved without them.

In the $\theta = 60°$ experiment, the prototype featured angle stops and utilized a minimal-interference gravity offload system, where supports hoisted the structure at intermediate truss nodes using strings to ensure continuous vertical alignment. This setup effectively simulated a zero-gravity environment and minimized external forces that could distort the configuration. These enhancements significantly improved the precision of the deployment. As expected, the angle stops played a key role in controlling the structure's movement, preventing the formation of unwanted

kinks and concave polygons that were problematic in the $\theta = 90°$ case. With these mechanisms in place, the assembly process was smoother and more symmetrical (see Figs. 6.5(a-c)), enabling a more controlled deployment of each bay. The deployment was significantly more consistent and predictable compared to the earlier tests as well.

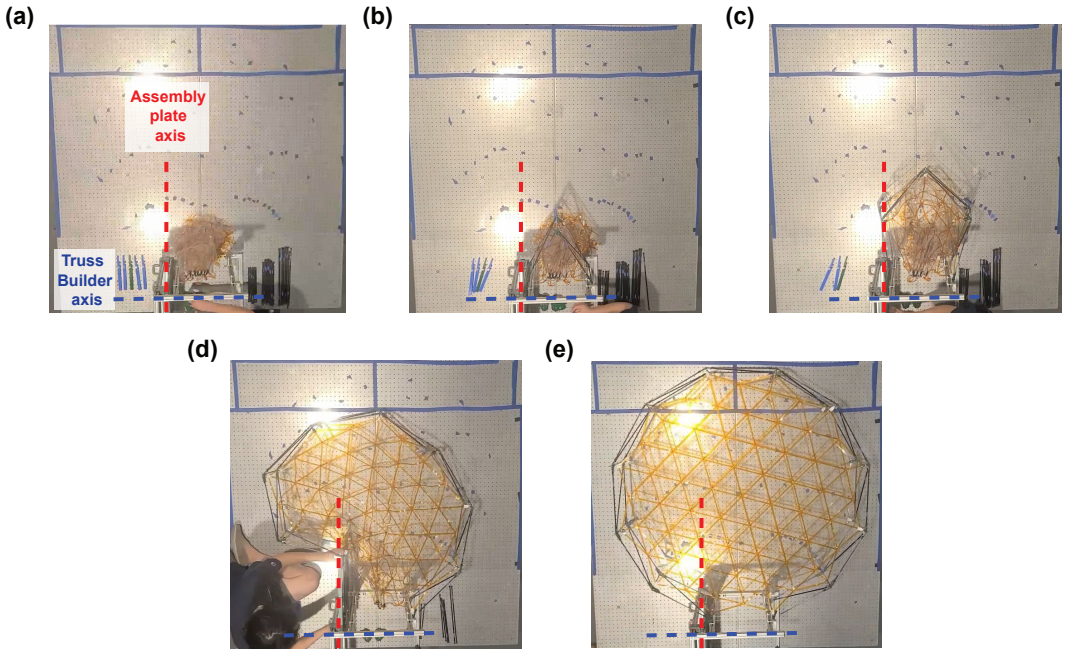

Figure 6.4: Reflector assembly demonstration for $\theta = 90°$: a) initial state, b) $i = 3$, c) $i = 5$, d) $i = 10$ with kink formation, and e) $i = 12$: completed reflector.

While the final assembled structure did not achieve good accuracy, the experimental results closely aligned with the expected configuration from the simulations, particularly towards the end of the assembly process, see Figs. 6.5(b) and (c). This agreement with the simulations confirmed the effectiveness of the design improvements, enabling smoother, more reliable assembly process and demonstrating that the structure could be successfully deployed with minimal intervention.

Simulations can be setup to follow any assembly plate angle between 0° and 90°. However, it is important to note that a smaller angle θ results in a reduced working space for the robotic manipulator, see Fig. 6.6. Therefore, a trial-and-error approach was used to determine a suitable angle between 90° and 60° that would offer more working space while ensuring an uninterrupted assembly process and achieving a shape closest to the desired one, ultimately selecting 72°.

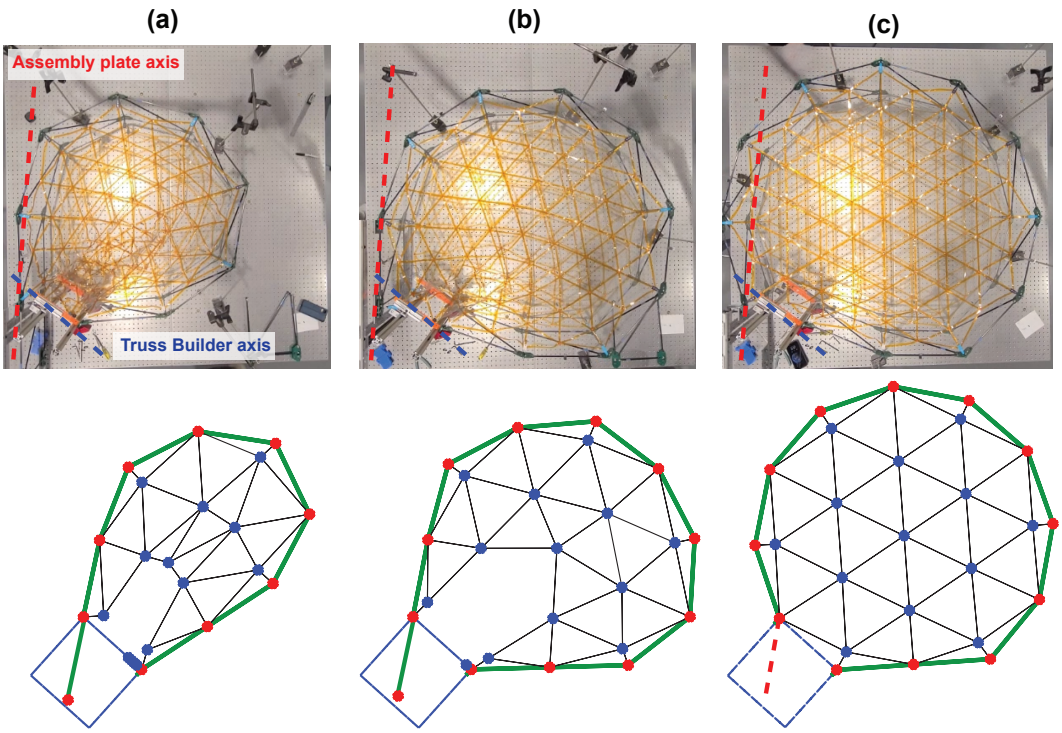

Figure 6.5: Comparison of experimental and simulation results for $\theta = 60°$: a) $i = 9$, b) $i = 11$, and c) $i = 12$: completed reflector.

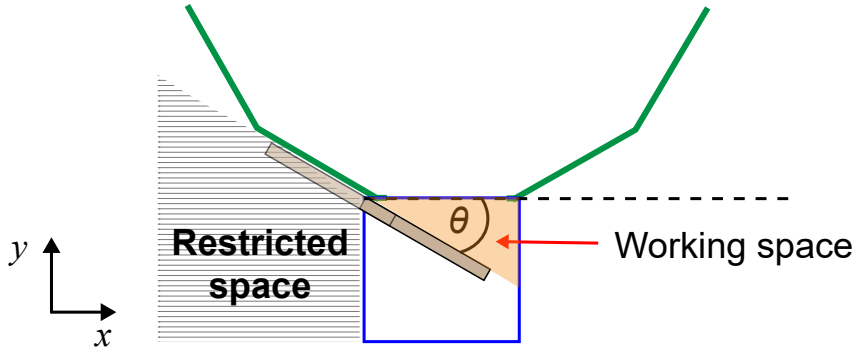

Figure 6.6: Relationship between θ and working space for the robotic manipulator.

6.3.2 Prestressing Method

The final configuration for the $\theta = 72°$ and cable net orientation 2, with prestressing achieved by moving the final bay as detailed in Section 5.3, shows that the nodes N_1-N_3 have become collinear (Fig. 6.7(a)), a result consistent with the simulations. A closer inspection reveals that the cable net is stretched undesirably due to the collinearity of the nodes when prestressing is achieved by moving the last bay, see Fig. 6.7(b). This observation underscores that the assembly plate ori-

entation is not the sole design consideration. The method of prestressing must also be addressed in the experimental setup, with cables remaining slack until the final stages of the assembly process to ensure smooth progression.

In the $\theta = 72°$ case, with prestressing imposed by adjusting the truss support, the assembly process starts with deploying the pre-built bays. After forming the initial polygon, the support is repositioned (Figs. 6.8(a) and (b)). Despite noticeable distortion, the assembly proceeds smoothly as more bays are added, causing the reflector's diameter to gradually increase. The shape of the truss becomes biased away from the assembly plate (Fig. 6.8(c-e)). However, as the support is gradually moved back at the end of the assembly, the shape of the reflector is corrected (Fig. 6.8(f)), with the cable net near the first joint still exhibiting some sagging. The final configuration, shown with an overlay of the simulation results, demonstrates a good qualitative match, highlighting the effectiveness of the modification made to the prestressing method.

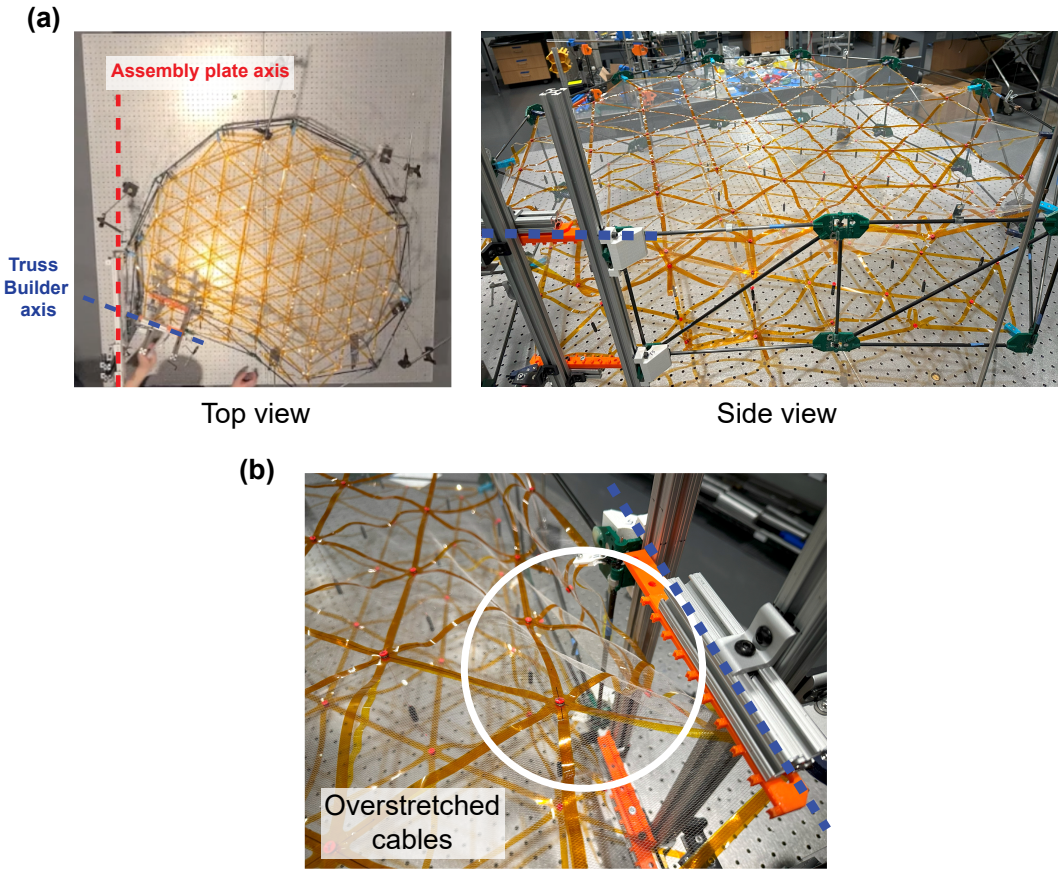

Figure 6.7: Reflector prototype assembled at $\theta = 72°$, prestressed by moving the last bay: a) collinear truss nodes, and b) undesirable stretching of cables.

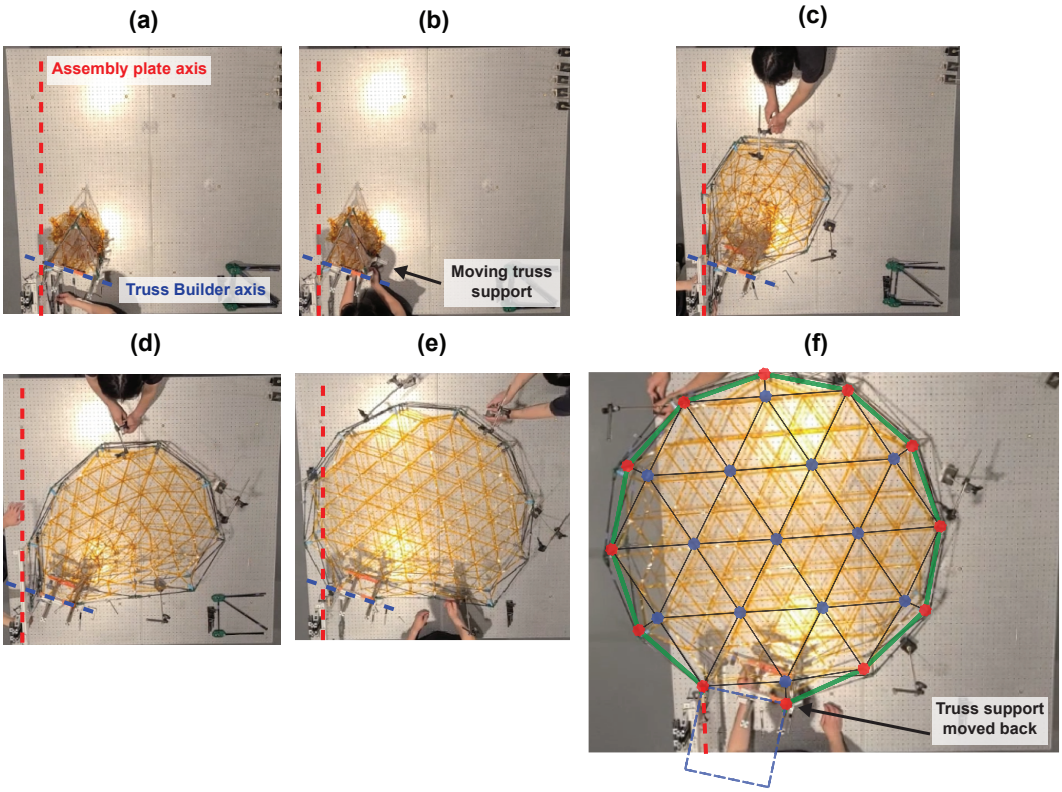

Figure 6.8: Assembly demonstration for $\theta = 72°$, prestressed by moving the truss support: a) $i = 3$, b) truss support S_1 moved, c) $i = 7$, d) $i = 10$, e) $i = 12$: prior to repositioning S_1, and f) $i = 12$: completed reflector, overlaid with the corresponding simulation result.

Based on these observations, a 72° assembly plate orientation was selected for future work on the prototype, with prestressing accomplished through adjustments to the truss support and the use of cable net orientation 2.

6.4 Chapter Conclusions

This chapter has described the proof-of-concept demonstrator, which has successfully verified the feasibility of the proposed ISA concept through a series of experimental validations. The entire assembly process was carried out within the truss builder, with each bay constructed and released as planned, and the folded net deployed progressively as more bays were added.

The experiments presented in this chapter have offered valuable insights into the design considerations and their practical effects, serving as critical test cases for comparing with the simulation results presented in Chapters 4 and 5. For the $\theta = 90°$ assembly plate case, the lack of angle stops led to structural distortions and

cable damage, underscoring their importance in maintaining precision. The $\theta = 60^\circ$ case, which included angle stops and a minimal interference gravity offload system, achieved a more controlled and symmetrical deployment, closely matching simulation predictions. In the $\theta = 72^\circ$ case, selected to improve the working space through trial and error, truss node collinearity matched simulation predictions. However, the issue of undesirable stretching in the cable net, as predicted by the simulations (for $\theta = 90^\circ$ and prestressing through movement of the last bay), was effectively addressed by carefully selecting both the assembly plate orientation and prestressing method.

The prototype reflector, designed for modular assembly by simple robots and manufactured using additive techniques, successfully demonstrated bay construction and release operations. Although the proof-of-concept demonstration of the assembly process is still in progress, the results confirm the viability of the proposed ISA scheme for large mesh reflectors and affirms the qualitative predictions made by two-dimensional simulations. It provides a robust basis for scaling the concept to full-sized applications and future space missions.

Chapter 7

SUMMARY AND PERSPECTIVES

7.1 Summary

This thesis has presented an in-depth exploration of mesh reflector design and simulation for In-Space Assembly (ISA). It has introduced a generalized design method to evaluate key performance measures, including mass, stowed volume, and natural frequency. A two-dimensional finite element model has been developed to predict the kinematics of large ring-like structures with a prestressed cable interior, assembled by a stationary robot.

The first part of the thesis has presented a rapid design approach for deployable mesh reflector antennas, based on the advanced AstroMesh architecture. It targets key metrics—mass, stowed volume, and natural frequency—for reflectors up to 200 meters in diameter, with focal length-to-aperture (F/D) ratios of 0.5, 0.7, and 1.0, at an operational radio frequency of 10 GHz and adhering to a surface accuracy requirement of 0.6 mm. The study has emphasized that optimizing prestress distribution and reducing cable net tension requirements can lead to much lower structural mass. Analytical scaling laws reveal that stowed volume, rather than mass, is the primary constraint for deployable mesh reflectors, supporting feasibility for launch diameters up to 70 - 100 meters with commercial launch vehicles. Additionally, a high-fidelity model and a semi-analytical model have been introduced for estimating fundamental natural frequencies of reflectors, the latter offering computational efficiency and validity for all F/D ratios.

The next part of the study has explored the design and feasibility of mesh reflectors for ISA, emphasizing their stowage in current launch vehicles. Building on the previously developed generalized design method, the research has examined reflectors up to 200 meters in diameter and introduces a novel ISA concept featuring a stationary robotic assembly facility. This facility, which remains compact during launch, assembles a perimeter truss in space by sequentially adding unit cells and attaching boundary nodes. The ISA method, leveraging the AstroMesh reflector architecture, minimizes launch envelope requirements and offers substantial benefits over traditional deployable designs. The truss builder's straightforward and scalable robotic operations provide a viable solution for constructing large, complex struc-

tures essential for future space missions, including high-resolution imaging and advanced communications.

A two-dimensional finite element model has been introduced for predicting the kinematics of large ring-like structures with a prestressed cable interior during assembly. This model, implemented in ABAQUS/CAE, refines the proposed ISA concept by simulating a six-sided perimeter truss with a simple cable net, focusing on improving computational efficiency and accuracy. The simulation uses a dynamic time integration to capture the assembly process, including the sequential addition of truss bays and cable net attachment, revealing successful achievement of the desired regular hexagon shape for various assembly plate orientations. Sensitivity studies of the damping coefficients indicated minimal impact on cable extension variations, with lowest coefficients that ensure stability chosen for the study. The results emphasize the need for precise planning and simulation to achieve stable final structures in space.

This numerical simulation setup lays the groundwork for improving assembly efficiency and robustness of the stationary robot. The thesis focused on a twelve-sided truss structure with a complex internal cable network to understand its nonsymmetric deployment in space. The study examines how assembly sequences, assembly plate orientation (notably $\theta = 60°$), and prestressed cable management affect the stability and desired final configuration. Key findings highlighted the need for precise prestressing and careful sequencing to prevent disruptions and emphasize the importance of an accurate cable stiffness model to meet design specifications. These insights are crucial for optimizing autonomous assembly systems and enhancing the precision and efficiency of large-scale space structures.

A lab-scale prototype developed to validate the ISA concept features a twelve-sided perimeter truss and a 1.4-meter diameter. Designed and tested by a team at the Caltech Space Structures Lab, the prototype has confirmed the ISA concept and verified the simulation approach. Experiments demonstrated that large, high-precision ring-like structures can be assembled in space using the proposed robotic system. Successful assembly, especially with a $60°$ plate orientation, confirmed the qualitative predictions and highlighted the need for angle stops together with the minimal interference gravity offload system to ensure accurate predictions. The simulation techniques provide a solid foundation for identifying key design considerations crucial for scaling to full-sized applications and future space missions.

Overall, this research has advanced the design and deployment of large structures in space, with significant implications for the future of space construction, potentially leading to new space habitats, satellite systems, and critical infrastructure necessary for extended space missions.

7.2 Future work

This thesis established the foundational background for designing mesh reflectors, introduced an ISA concept to address current limitations, and developed simulation techniques for evaluating the proposed concept and ISA of other large, ring-like structures with a prestressed cable interior.

There are at least three significant research directions that stem directly from the findings of this thesis. First, minimizing the cable element tension requirement through alternative reflective surfaces such as corrugated Kapton films to reduce structural mass, and shifting from magnet-based assembly systems to mechanical latches to resolve performance issues in space. Second, developing strategies to optimize the packaging of components and the assembly facility to accommodate increasingly large structures. Third, improving the accuracy of two-dimensional simulation techniques by incorporating out-of-plane deformations, comparing quantitative simulation predictions with experimental data, and ensuring that the model effectively captures mass and stiffness properties of the structure.

As described in Chapter 2, the minimum tension requirement of cable elements is driven by the length of the cable elements, and the biaxial prestress of the reflective metallic mesh. This thesis explored methods to shorten cable elements, but current metallic meshes necessitate high biaxial prestress. Reducing this prestress is essential for decreasing the load on the perimeter truss, which can lead to smaller component sizes, enhancing mass and volume efficiency. In collaboration with the Bargatin Group at the University of Pennsylvania, alternative reflective surfaces are being investigated, including perforated Kapton films with an aluminized side for enhanced reflectivity, see Fig. 7.1(a). These materials have shown the potential to achieve lower prestress levels of about 0.1 - 0.2 N/m—approximately a $1/50$ reduction—while significantly reducing the structural mass without sacrificing performance. Figure 7.1(b) shows that as biaxial prestress decreases, the mass of a 200-meter diameter structure is significantly reduced, decreasing from about 11,000 kg to approximately 2,200 kg. Future work will involve exploring the integration of perforated Kapton films with the cable net, focusing on their attachment

methods and performance to ensure that the structural efficiency and reflectivity of the system meets design specifications.

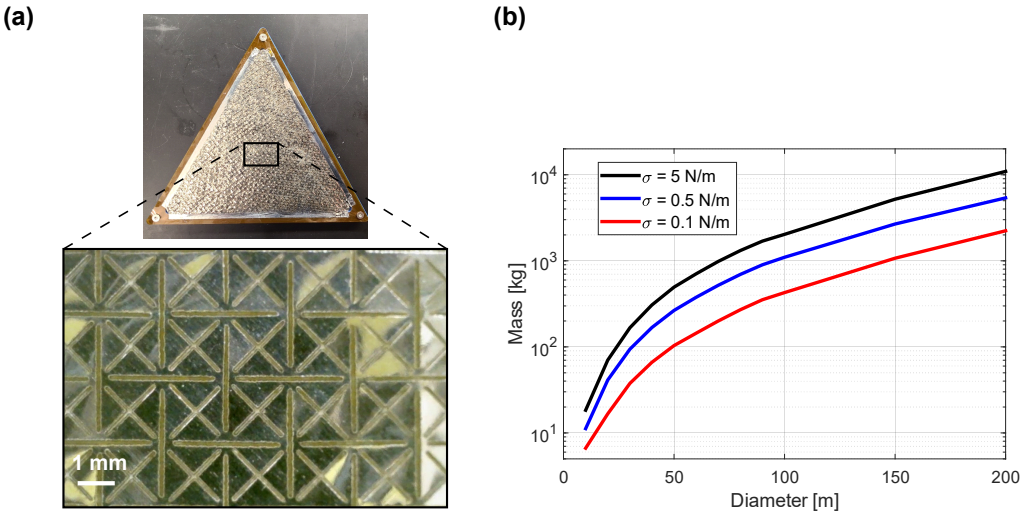

Figure 7.1: Perforated Kapton films, 25.4 μm thick, with a 100 nm aluminized coating on one side for reflectivity: a) a single facet of cable net, with a magnified view of the perforation, patterned using a CO_2 laser, and b) achievable reduction of mass with lowered biaxial prestress, σ for $F/D = 1.0$.

The current assembly system uses permanent and electromagnets for securing and releasing components. However, permanent magnets pose several challenges in space, including risks of radiation-induced and thermal demagnetization [68], [69], oxidation in Low Earth Orbit (LEO) [70], and brittleness that can lead to fracturing [71]. These issues necessitate protective measures such as Alodine-coated aluminum shielding and encapsulation with thermal epoxy to ensure mechanical bonding and thermal conductivity. To address these challenges, the design should evolve to potentially eliminate magnets altogether. Instead, mechanical latches could be used for part handling and assembly mechanisms. If magnets are retained, they must undergo rigorous qualification tests, including thermal vacuum cycling, vibration, shock testing, and CTE mismatch analysis.

As structures increase in size, the ISA concept will require a more efficient packaging scheme to accommodate the growing number of struts and joints within the truss builder. This includes optimizing the stowage configuration to compactly store all components during launch and deploy them efficiently in space. Future advancements could integrate deployable booms as struts and utilize in-space manufacturing techniques, such as additive manufacturing [72], to construct and connect components (see Fig. 7.2). An additional crucial development is the stowage of the truss

builder itself. Strut length dictates bay size, directly impacting the overall dimensions of the truss builder. For example, at $D = 100$ m, the truss builder size would expand to around $6 \times 6 \times 14$ m^3, reaching the capacity of current commercial launch vehicles. Therefore, it is essential to devise an efficient method for folding and deploying the truss builder, ensuring that the components and assembly mechanisms remain intact throughout the process.

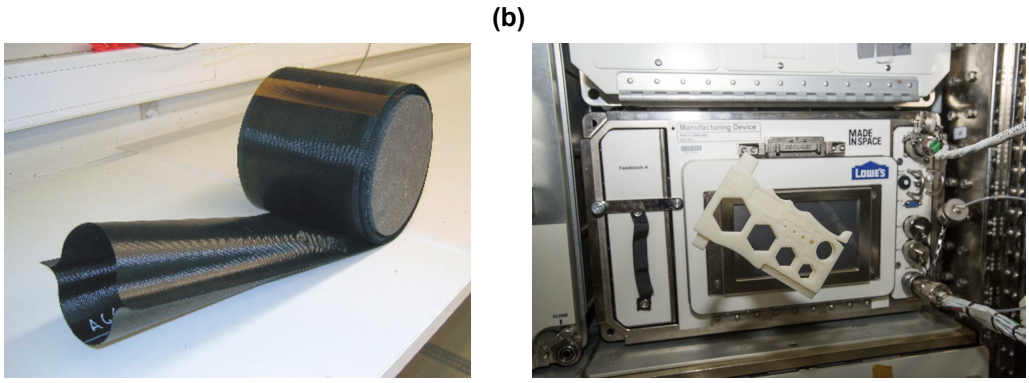

Figure 7.2: Potential enhancements to improve packaging efficiency: (a) deployable coilable Omega boom [73], and (b) additive manufacturing of components in space [74].

The accuracy of the two-dimensional model's quantitative predictions must be evaluated, particularly in capturing assembly process effects that may require a three-dimensional model. To achieve this, the simulation should be expanded to account for out-of-plane deformations, such as misalignments between the top and bottom rings of the perimeter truss. Comparing the two-dimensional and three-dimensional simulation approaches with experimental results will help ensure whether such effects are minimal and further validate the reliability of the two-dimensional model. Moreover, analyzing the natural frequencies of the intermediate polygonal structures—which lack stiffness due to absence of prestress—is crucial if assembly time scales are longer than the vibration periods, as unaddressed vibrations could affect the continuity and accuracy of the assembly process. Future adaptations could also include a three-dimensional model to measure the accuracy of the cable net's paraboloid surface at the end of assembly. This can be a direct extension of the two-dimensional model and therefore more computationally efficient than a high-fidelity model.

This thesis presented a solution space for assembling ring-like structures with a stationary robot. However, continued research is required to optimize various design elements of the proposed ISA concept, including the orientations of the assembly

plate and methods for prestressing. Identifying configurations that minimize distortions while maintaining stability and precision will be crucial for improving the feasibility of space-based structures, particularly for future missions that require large apertures.

7.3 Perspectives

The proposed ISA concept marks a pivotal shift in the design and construction of large-scale space structures. Utilizing a stationary robot for scalable, simple, and repetitive operations, this concept offers a versatile approach to assembling extensive space infrastructure, paving the way for groundbreaking advancements in space exploration and technology.

The core innovation of ISA lies in its departure from traditional deployable systems, which often face limitations in scalability and complexity due to constraints imposed by the launch vehicle's payload envelope. This paradigm shift is particularly significant for missions requiring vast infrastructure, such as space-based solar power systems, where large solar arrays could be assembled in orbit. Such applications not only advance space exploration but also hold promise for sustainable energy solutions on Earth.

This research renews interest in ISA by addressing technical challenges and exploring modular assembly techniques that have the potential to revolutionize the construction of space-based structures. The successful demonstration of the ISA concept through lab-scale prototype testing has validated the assembly process for reflectors using stationary robotic systems, demonstrating the potential of ISA to revolutionize large space-based infrastructure assembly and providing a robust foundation for future developments.

The transformative impact of this research extends well beyond technical feasibility, offering a new perspective on space construction and expanding possibilities for future space missions. Structures assembled using ISA could significantly improve imaging and communication technologies, enabling pioneering discoveries and a deeper understanding of our solar system and the universe. This advancement underscores the importance of continued research and development in this field.

AN ILLUSTRATION OF ISA REFLECTORS: CAN E.T. “PHONE HOME” AFTER ALL?

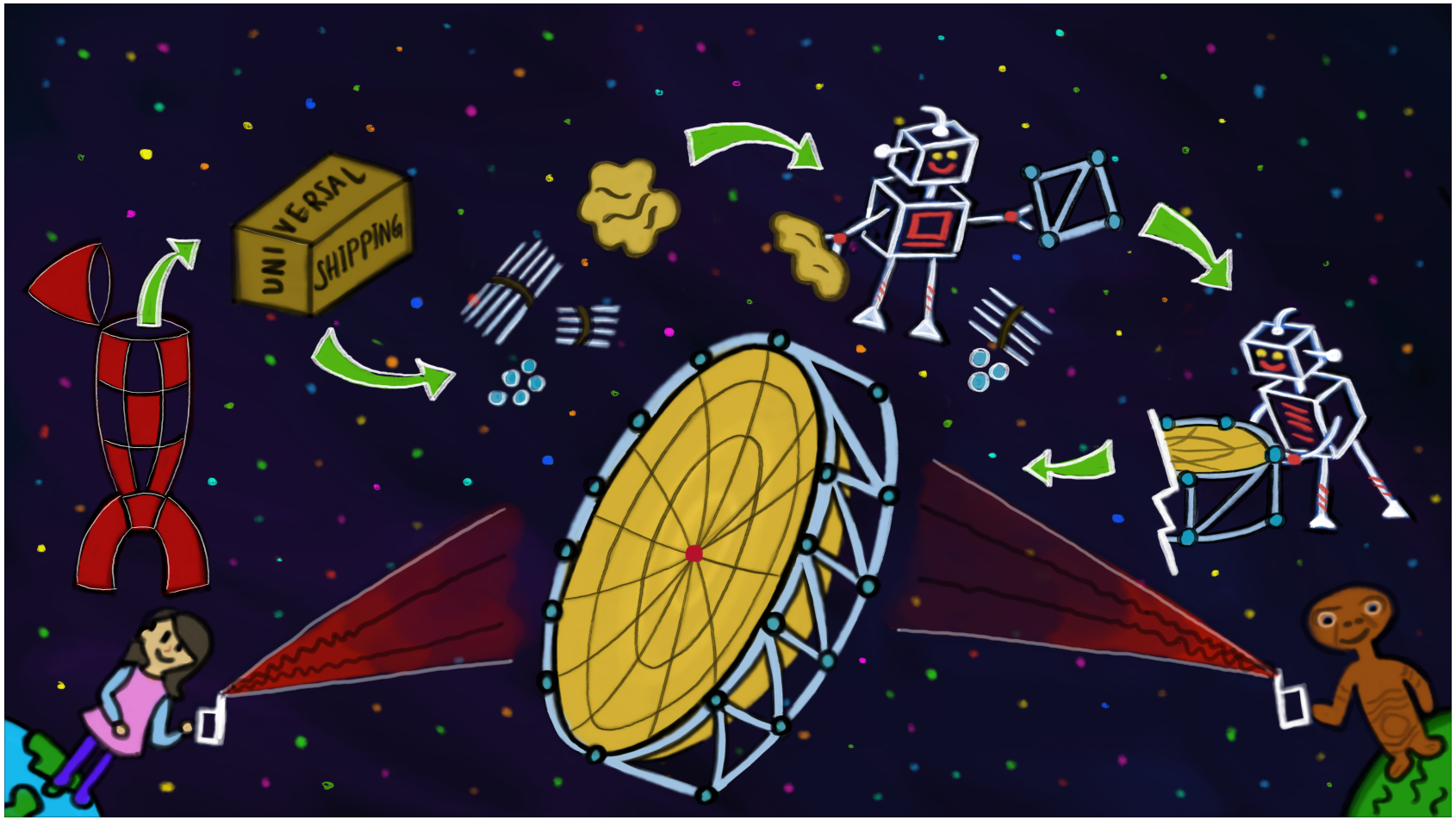

BIBLIOGRAPHY

[1] L. Puig, A. Barton, and N. Rando, "A Review on Large Deployable Structures for Astrophysics Missions," *Acta Astronautica"*, vol. 67, no. 1-2, pp. 12–26, 2010. DOI: 10.1016/j.actaastro.2010.02.021.

[2] G. Agnes, "Precision Deployable Structures Technology for NASA Large Aperture Missions," in *Space 2004 Conference and Exhibit*, 2004, p. 5899. DOI: 10.2514/6.2004-5899.

[3] E. Gdoutos, C. F. Sommer, A. Truong, *et al.*, "Development of the Deployable on-Orbit ultraLight Composite Experiment (DOLCE) for the Space Solar Power Project Demonstration Mission," in *AIAA SCITECH 2022 Forum*, 2022, p. 1266. DOI: 10.2514/6.2022-1266.

[4] K. Miura and S. Pellegrino, *Forms and Concepts for Lightweight Structures*. Cambridge University Press, 2020, ISBN: 9781139048569. DOI: 10.1017/9781139048569.

[5] M. R. Johnson, "The Galileo High Gain Antenna Deployment Anomaly," May 1994, pp. 359–377. [Online]. Available: https://ntrs.nasa.gov/api/citations/19940028813/downloads/19940028813.pdf.

[6] A. Rivera and A. Stewart, "Study of Spacecraft Deployables Failures," Aug. 2021. [Online]. Available: https://ntrs.nasa.gov/api/citations/20210020397/downloads/Alphonzo%20Stewart-%20Final%20Paper.pdf.

[7] P. A. Sabelhaus and J. E. Decker, "An Overview of the James Webb Space Telescope (JWST) Project," *Proc. SPIE 5487, Optical, Infrared, and Millimeter Space Telescopes*, vol. 5487, pp. 550–563, 2004. DOI: 10.1117/12.549895.

[8] "FAQ for Scientists Webb Telescope/NASA." (2024), [Online]. Available: https://webb.nasa.gov/content/forScientists/faqScientists.html#astronauts (visited on 07/2024).

[9] R. P. Hoyt, "SpiderFab: An Architecture for Self-Fabricating Space Systems," in *AIAA SPACE 2013 Conference and Exposition*, 2013. DOI: 10.2514/6.2013-5509.

[10] "DARPA Kicks Off Program to Explore Space-Based Manufacturing." (2022), [Online]. Available: https://www.darpa.mil/news-events/2022-03-23 (visited on 07/2022).

[11] W. R. Oegerle, L. R. Purves, J. G. Budinoff, *et al.*, "Concept for a Large Scalable Space Telescope: In-Space Assembly," in *Proc. SPIE 6265, Space Telescopes and Instrumentation I: Optical, Infrared, and Millimeter*, vol. 6265, 2006, p. 62652C. DOI: 10.1117/12.672244.

[12] D. Ebbets, J. DeCino, and J. Green, "Architecture Concept for a 10 m UV-Optical Space Telescope," in *Proc. SPIE 6265,Space Telescopes and Instrumentation I: Optical, Infrared, and Millimeter*, vol. 6265, 2006, 62651S. DOI: 10.1117/12.670466.

[13] M. Lake, "Launching a 25-meter Space Telescope. Are Astronauts a Key to the Next Technically Logical Step after NGST?" In *2001 IEEE Aerospace Conference Proceedings (Cat. No.01TH8542)*, vol. 7, 2001, pp. 7–3611. DOI: 10.1109/AERO.2001.931444.

[14] M. M. Mikulas Jr., H. G. Bush, and M. F. Card, "Structural Stiffness, Strength and Dynamic Characteristics of Large Tetrahedral Space Truss Structures," *NASA Technical Memorandum (TM) X-74001*, Mar. 1977. [Online]. Available: http://hdl.handle.net/2060/19770012543.

[15] M. M. Mikulas Jr. and J. T. Dorsey, "An Integrated In-Space Construction Facility for the 21st Century," *NASA Technical Memorandum (TM) 101515*, Nov. 1988. [Online]. Available: https://ntrs.nasa.gov/api/citations/19890004115/downloads/19890004115.pdf.

[16] M. M. Mikulas Jr., T. J. Collins, and J. M. Hedgepeth, "Preliminary Design Approach for Large High Precision Segmented Reflectors," *NASA Technical Memorandum (TM) 102605*, Feb. 1990. [Online]. Available: https://ntrs.nasa.gov/api/citations/19900011780/downloads/19900011780.pdf.

[17] H. Bush, C. Herstrom, W. Heard Jr, T. Collins, and W. Fichter, "Design and Fabrication of an Erectable Truss for Precision Segmented Reflector Application," *31st Structures, Structural Dynamics and Materials Conference*, Apr. 1990. DOI: 10.2514/6.1990-999.

[18] Z. Xue, J. Liu, C. Wu, and Y. Tong, "Review of in-space assembly technologies," *Chinese Journal of Aeronautics*, vol. 34, no. 11, pp. 21–47, 2021. DOI: 10.1016/j.cja.2020.09.043.

[19] W. Whittaker, C. Urmson, P. Staritz, B. Kennedy, and R. Ambrose, "Robotics for Assembly, Inspection, and Maintenance of Space Macrofacilities," in *Proceedings of AIAA Space Conference and Exposition*, AIAA, Sep. 2000, pp. 1–6.

[20] S.-I. Nishida and T. Yoshikawa, "A new end-effector for on-orbit assembly of a large reflector," in *2006 9th International Conference on Control, Automation, Robotics and Vision*, IEEE, 2006, pp. 1–6. DOI: 10.1109/ICARCV.2006.345414.

[21] W. L. Heard Jr., J. Watson, J. Ross, S. Spring, and M. Cleave, "Results of the ACCESS Space Construction Shuttle Flight Experiment," in *Proceedings of the 2nd Aerospace Maintenance Conference, AIAA*, American Institute of Aeronautics and Astronautics, vol. 1186, 1986. DOI: 10.2514/6.1986-1186.

[22] W. L. Heard Jr. and M. S. Lake, "Neutral buoyancy evaluation of extravehicular activity assembly of a large precision reflector," *Journal of Spacecraft and Rockets*, vol. 31, no. 4, pp. 569–577, 1994. DOI: 10.2514/3.26480.

[23] J. Watson, T. Collins, and H. Bush, "A History of Astronaut Construction of Large Space Structures at NASA Langley Research Center," in *Proceedings, IEEE Aerospace Conference*, vol. 7, 2002, pp. 7–7. DOI: 10.1109/AERO.2002.1035334.

[24] J. P. Trevelyan, S.-C. Kang, and W. R. Hamel, "Robotics in Hazardous Applications," in *Springer Handbook of Robotics*. Springer Berlin Heidelberg, 2008, pp. 1101–1126, ISBN: 978-3-540-30301-5. DOI: 10.1007/978-3-540-30301-5_49.

[25] J. M. Davila Delgado, L. Oyedele, A. Ajayi, *et al.*, "Robotics and Automated Systems in Construction: Understanding Industry-Specific Challenges for Adoption," *Journal of Building Engineering*, vol. 26, p. 100 868, 2019, ISSN: 2352-7102. DOI: 10.1016/j.jobe.2019.100868.

[26] R. Smith, E. Cucco, and C. Fairbairn, "Robotic Development for the Nuclear Environment: Challenges and Strategy," *Robotics*, vol. 9, no. 4, 2020, ISSN: 2218-6581. DOI: 10.3390/robotics9040094.

[27] B. Xiao, C. Chen, and X. Yin, "Recent Advancements of Robotics in Construction," *Automation in Construction*, vol. 144, p. 104 591, 2022, ISSN: 0926-5805. DOI: 10.1016/j.autcon.2022.104591.

[28] D. W. Miller, S. Mohan, and J. Budinoff, "Assembly of a Large Modular Optical Telescope (ALMOST)," in *Space Telescopes and Instrumentation 2008: Optical, Infrared, and Millimeter*, SPIE, vol. 7010, 2008, pp. 717–727. DOI: 10.1117/12.788566.

[29] N. Lee, P. Backes, J. Burdick, *et al.*, "Architecture for In-Space Robotic Assembly of a Modular Space Telescope," *Journal of Astronomical Telescopes, Instruments, and Systems*, vol. 2, no. 4, pp. 041 207–041 207, 2016. DOI: 10.1117/1.JATIS.2.4.041207.

[30] O. Formoso, C. Gregg, G. Trinh, A. Rogg, and K. Cheung, "Androgynous Fasteners for Robotic Structural Assembly," in *2020 IEEE Aerospace Conference*, 2020, pp. 1–8. DOI: 10.1109/AERO47225.2020.9172583.

[31] Q. Lindsey and V. Kumar, "Distributed Construction of Truss Structures," in *Algorithmic Foundations of Robotics X*, Springer Berlin Heidelberg, 2013, pp. 209–225, ISBN: 978-3-642-36279-8. DOI: 10.1007/978-3-642-36279-8_13.

[32] R. A. Knepper, T. Layton, J. Romanishin, and D. Rus, "IkeaBot: An Autonomous Multi-Robot Coordinated Furniture Assembly System," in *2013 IEEE International Conference on Robotics and Automation*, 2013, pp. 855–862. DOI: 10.1109/ICRA.2013.6630673.

[33] J. Werfel, K. Petersen, and R. Nagpal, "Designing Collective Behavior in a Termite-Inspired Robot Construction Team," *Science*, vol. 343, no. 6172, pp. 754–758, 2014. DOI: 10.1126/science.1245842.

[34] B. Jenett and K. Cheung, "BILL-E: Robotic platform for Locomotion and Manipulation of Lightweight Space Structures," in *25th AIAA/AHS Adaptive Structures Conference*, 2017. DOI: 10.2514/6.2017-1876.

[35] A. G. Roederer and Y. Rahmat-Samii, "Unfurlable Satellite Antennas: A Review," in *Annales Des Télécommunications*, vol. 44, 1989. DOI: 10.1007/BF02995012.

[36] R. Russell, T. Campbell, and R. Freeland, "A Technology Development Program for Large Space Antennas," Tech. Rep., 1980.

[37] K. Miura *et al.*, "Research and Development of the Tension Truss Antenna," IAF-87-317, Tech. Rep., 1987.

[38] K. Miura and Y. Miyazaki, "Concept of the Tension Truss Antenna," *AIAA Journal*, vol. 28, no. 6, pp. 1098–1104, 1990. DOI: 10.2514/3.25172.

[39] J. M. Hedgepeth, "Influence of Fabrication Tolerances on the Surface Accuracy of Large Antenna Structures," *AIAA Journal*, vol. 20, no. 5, pp. 680–686, 1982. DOI: 10.2514/3.7936.

[40] M. W. Thomson, "The Astromesh Deployable Reflector," in *IEEE Antennas and Propagation Society International Symposium. 1999 Digest. Held in conjunction with: USNC/URSI National Radio Science Meeting (Cat. No. 99CH37010)*, IEEE, vol. 3, 1999, pp. 1516–1519. DOI: 10.1109/APS.1999.838231.

[41] M. Thomson, "AstroMesh Deployable Reflectors for Ku and Ka Band Commercial Satellites," in *20th AIAA International Communication Satellite Systems Conference and Exhibit*, 2002, p. 2032. DOI: 10.2514/6.2002-2032.

[42] T. Smith, B. Lee, D. Semler, and D. Chae, "A Large S-Band Antenna for a Mobile Satellite," in *Space 2004 Conference and Exhibit*, 2004, p. 6120. DOI: 10.2514/6.2004-6120.

[43] D. Entekhabi, E. G. Njoku, P. E. O'Neill, *et al.*, "The Soil Moisture Active Passive (SMAP) Mission," *Proceedings of the IEEE*, vol. 98, no. 5, pp. 704–716, 2010. DOI: 10.1109/JPROC.2010.2043918.

[44] L. Scialino, A. Ihle, M. Migliorelli, *et al.*, "Large Deployable Reflectors for Telecom and Earth Observation Applications," *CEAS Space Journal*, vol. 5, no. 3-4, pp. 125–146, 2013. DOI: 10.1007/s12567-013-0044-7.

[45] L. Datashvili, S. Endler, B. Wei, *et al.*, "Study of Mechanical Architectures of Large Deployable Space Antenna Apertures: from Design to Tests," *CEAS Space Journal*, vol. 5, no. 3-4, pp. 169–184, 2013. DOI: 10.1007/s12567-013-0050-9.

[46] T. Li, J. Jiang, H. Deng, Z. Lin, and Z. Wang, "Form-Finding Methods for Deployable Mesh Reflector Antennas," *Chinese Journal of Aeronautics*, vol. 26, no. 5, pp. 1276–1282, 2013. DOI: 10.1016/j.cja.2013.04.062.

[47] D. Yang, Y. Zhang, G. Yang, and J. Du, "Least-Squares Minimization of Boundary Cable Tension Ratios for Mesh Reflectors," *AIAA Journal*, vol. 56, no. 2, pp. 883–888, 2018. DOI: 10.2514/1.J056222.

[48] D. Yang, Y. Zhang, P. Li, and J. Du, "Numerical Form-Finding Method for Large Mesh Reflectors with Elastic Rim Trusses," *Acta Astronautica*, vol. 147, pp. 241–250, 2018. DOI: 10.1016/j.actaastro.2018.04.007.

[49] S. Zhang, S. Zhang, Y. Zhang, and J. Ye, "Force Density Sensitivity Form-Finding Design Method for Cable-Mesh Reflector Antennas considering Interactive Effects between Cable Network and Supporting Truss," *Engineering Structures*, vol. 244, p. 112 722, 2021. DOI: 10.1016/j.engstruct.2021.112722.

[50] S. Morterolle, B. Maurin, J.-F. Dube, J. Averseng, and J. Quirant, "Modal Behavior of a New Large Reflector Conceptual Design," *Aerospace Science and Technology*, vol. 42, pp. 74–79, 2015. DOI: 10.1016/j.ast.2015.01.002.

[51] P. Li, C. Liu, Q. Tian, H. Hu, and Y. Song, "Dynamics of a Deployable Mesh Reflector of Satellite Antenna: Form-Finding and Modal Analysis," *Journal of Computational and Nonlinear Dynamics*, vol. 11, no. 4, 2016. DOI: 10.1115/1.4033440.

[52] P. Li, C. Liu, Q. Tian, H. Hu, and Y. Song, "Dynamics of a Deployable Mesh Reflector of Satellite Antenna: Parallel Computation and Deployment Simulation," *Journal of Computational and Nonlinear Dynamics*, vol. 11, no. 6, 2016. DOI: 10.1115/1.4033657.

[53] B. Siriguleng, W. Zhang, T. Liu, and Y. Liu, "Vibration Modal Experiments and Modal Interactions of a Large Space Deployable Antenna with Carbon Fiber Material and Ring-Truss Structure," *Engineering Structures*, vol. 207, p. 109 932, 2020. DOI: 10.1016/j.engstruct.2019.109932.

[54] S. W. Smith, C. S. Pack, and T. J. Bartkowicz, "Understanding Dynamic Challenges of In-Space Modular Assembly and Reconfiguration of Flexible Structures from Early Efforts," in *AIAA SCITECH 2022 Forum*, 2022. DOI: 10.2514/6.2022-2374.

[55] *Abaqus/CAE*, Dassault Systemes Simulia Corp., 2020.

[56] J. D. Kraus and R. Marhefka, *Antennas for All Applications*. McGraw-Hill, New York, 2002.

[57] L. T. Tan and S. Pellegrino, "Thin-Shell Deployable Reflectors with Collapsible Stiffeners Part 1: Approach," *AIAA Journal*, vol. 44, no. 11, pp. 2515–2523, 2006. DOI: 10.2514/1.16320.

[58] P. Agrawal, M. Anderson, and M. Card, "Preliminary Design of Large Reflectors with Flat Facets," *IEEE Transactions on Antennas and Propagation*, vol. 29, no. 4, pp. 688–694, 1981. DOI: 10.1109/TAP.1981.1142631.

[59] H. Shi, S. Yuan, and B. Yang, "New Methodology of Surface Mesh Geometry Design for Deployable Mesh Reflectors," *Journal of Spacecraft and Rockets*, vol. 55, no. 2, pp. 266–281, 2018. DOI: 10.2514/1.A33867.

[60] C. R. Calladine, "Buckminster Fuller's "Tensegrity" Structures and Clerk Maxwell's Rules for the Construction of Stiff Frames," *International Journal of Solids and Structures*, vol. 14, no. 2, pp. 161–172, 1978. DOI: 10.1016/0020-7683(78)90052-5.

[61] S. Pellegrino, "Structural Computations with the Singular Value Decomposition of the Equilibrium Matrix," *International Journal of Solids and Structures*, vol. 30, no. 21, pp. 3025–3035, 1993. DOI: 10.1016/0020-7683(93)90210-X.

[62] A. Tibert and S. Pellegrino, "Deployable Tensegrity Reflectors for Small Satellites," *Journal of Spacecraft and Rockets*, vol. 39, no. 5, pp. 701–709, 2002. DOI: 10.2514/2.3867.

[63] H. Deng, T. Li, and Z. Wang, "Design of Geodesic Cable Net for Space Deployable Mesh Reflectors," *Acta Astronautica*, vol. 119, pp. 13–21, 2016, ISSN: 0094-5765. DOI: 10.1016/j.actaastro.2015.10.024.

[64] *M55J High Modulus Carbon Fiber*, Rev. 2.0, Toray Composite Materials America, Inc., Jan. 2020.

[65] M. Kheradiya, "Effects of Edge Distance, Hole Size Ratio and Hole Spacing on Peak Stresses of Composite Laminate with Multiple Holes," M.S. thesis, Faculty of the Graduate School of The University of Texas at Arlington, 2008.

[66] *Falcon user's guide*, SpaceX, Sep. 2021.

[67] *Starship user's guide*, SpaceX, Mar. 2020.

[68] C. Chen, J. Talnagi, J. Liu, *et al.*, "The Effect of Neutron Irradiation on Sm2Co17-Based High Temperature Magnets and Nd-Fe-B Magnets," vol. 41, May 2005, pp. 1967–1968. DOI: 10.1109/INTMAG.2005.1464420.

[69] A. J. Samin Jr., "An Analysis of Neutron Radiation Effects on NdFeB Permanent Magnets," Ph.D. dissertation, Ohio State University, 2014.

[70] H. C. Hua, G. Y. Wang, Q. Z. Xu, H. J. Jin, and G. Q. Xu, "Study of Oxidation of NdFeB Permanent Magnets," *Physica Status Solidi (a)*, vol. 125, no. 2, pp. 615–624, 1991. DOI: 10.1002/pssa.2211250223.

[71] W. Li, A. Li, and H. Wang, "Anisotropic Fracture Behavior of Sintered Rare-Earth Permanent Magnets," *IEEE Transactions on Magnetics*, vol. 41, no. 8, pp. 2339–2342, 2005. DOI: 10.1109/TMAG.2005.852948.

[72] M. Hoffmann and A. Elwany, "In-Space Additive Manufacturing: A Review," *Journal of Manufacturing Science and Engineering*, vol. 145, no. 2, p. 020 801, 2022. DOI: 10.1115/1.4055603.

[73] J. Block, M. Straubel, and M. Wiedemann, "Ultralight Deployable Booms for Solar Sails and Other Large Gossamer Structures in Space," *Acta Astronautica*, vol. 68, no. 7-8, pp. 984–992, 2011. DOI: 10.1016/j.actaastro.2010.09.005.

[74] "Additive Manufacturing Facility: 3D Printing The Future in Space." (2019), [Online]. Available: https://redwirespace.com/newsroom/2019-3-28-additive-manufacturing-facility-3d-printing-the-future-in-space/ (visited on 07/2024).

Appendix A

HOMOGENIZED STIFFNESS MATRIX OF PARALLEL TESSELLATION

The equivalent in-plane stiffness matrix for equally spaced parallel truss elements oriented at an angle α to the x-axis is given by the expression [4]:

$$\begin{bmatrix} N_x \\ N_y \\ N_{xy} \end{bmatrix} = \frac{EA}{l} \begin{bmatrix} \cos^4\alpha & \sin^2\alpha\cos^2\alpha & \sin\alpha\cos^3\alpha \\ \sin^2\alpha\cos^2\alpha & \sin^4\alpha & \sin^3\alpha\cos\alpha \\ \sin\alpha\cos^3\alpha & \sin^3\alpha\cos\alpha & \sin^2\alpha\cos^2\alpha \end{bmatrix} \begin{bmatrix} \varepsilon_x \\ \varepsilon_y \\ \gamma_{xy} \end{bmatrix} \tag{A.1}$$

where E, A, and l represent the Young's modulus, cross-sectional area, and spacing between the elements, respectively. The terms N_x, N_y, and N_{xy} denote the force per unit width stress resultants, while ϵ_x, ϵ_y, and γ_{xy} are the corresponding in-plane strain components.

The homogenized in-plane stiffness matrix for the complete truss tessellation is obtained by summing the stiffness matrices for each set of parallel trusses.

For instance, the truss tessellation composed of equilateral triangles, as shown in Fig. 2.19(b), is divided into three sets of parallel trusses with inclination angles of $\alpha = 0°$, $60°$, and $120°$. The spacing between two adjacent parallel trusses is $\sqrt{3}L/2$, while the Young's modulus and cross-sectional area of the trusses are denoted as E_n and A_n, respectively. Applying Eq. (A.1), the constitutive equation for the truss tessellation is expressed as:

$$\begin{bmatrix} N_x \\ N_y \\ N_{xy} \end{bmatrix} = \frac{3\sqrt{3}E_nA_n}{4L} \begin{bmatrix} 1 & 1/3 & 0 \\ 1/3 & 1 & 0 \\ 0 & 0 & 1/3 \end{bmatrix} \begin{bmatrix} \varepsilon_x \\ \varepsilon_y \\ \gamma_{xy} \end{bmatrix}. \tag{A.2}$$

Appendix B

MODIFICATION OF CABLE STIFFNESS IN ABAQUS/CAE

This method allows for independent control over the constitutive behavior of multiple cables in the system, with each cable following its unique trajectory of material transition.

Consider a system with a single cable and two different constitutive behaviors, CB_1 and CB_2. The transition is governed by field variables (FV), where the cable is assigned its own FV to control the behavior shift. The cable material properties will change smoothly between CB_1 to CB_2 as the FV is ramped between the corresponding values across all nodes, as shown in Table B.1.

Table B.1: Material definition for a single cable

Constitutive Behavior	Field Variable Value
CB_1	Value 1
CB_2	Value 2

In this study, when the FV value of a cable with a specific extension is shifted from 0 to 1, the cable force transitions from that corresponding to zero stiffness behavior to non-zero stiffness behavior, described in Section 4.2.2 and depicted in Fig. 4.4. This change reflects the *activation* of the cable, enabling it to contribute to the structure's overall stiffness.

As the number of cables increases, so do the dependencies on the FV, making the system more complex and requiring precise control over the transitions between constitutive behaviors. Table B.2 presents the material definition for cable i in a system containing n cables, each exhibiting two distinct constitutive behaviors.

Table B.2: Material definition for cable i in a multi-cable system

Constitutive Behavior	FV1	FV2	.....	FVi
CB_1	0	0	0	0
CB_2	1	1	1	1

In this system, the dependencies on FV1 increase with the addition of each cable, from cable 2 to cable *n*. Hence, each cable is assigned a unique FV (e.g., FVi for cable *i*), enabling independent control over the transition of each cable between the two behaviors.

A PREDEFINED FIELD is established for each cable at the initial simulation step, where the FV number is assigned, and the magnitude is set to the value corresponding to the desired behavior at the start of the simulation. The magnitude of the FV defined in this manner can be modified to facilitate the transition between behaviors at later specific simulation steps.